

## ABSTRACT

TURGMAN COHEN, SALOMON. Controlling Surface Properties of Materials by Small Molecule and Polymer Grafts. (Under the direction of Jan Genzer and Peter K. Kilpatrick.)

Two topics related to chemical modification of material surfaces are investigated. First, we apply the “grafting to” approach to construct binary self-assembled monolayers (SAMs) used to control the adsorption of colloidal aggregates onto solid substrates. Second, we investigate the chemical modification of surfaces by employing Monte Carlo computer simulations to investigate the kinetics of surface-initiated controlled radical polymerization (CRP) for the synthesis of grafted polymer films (“grafting from” approach).

SAMs constitute layers of small molecules that assemble spontaneously at an interface. SAMs of mixed aromatic and aliphatic trichlorosilanes with varying thickness, aromaticity, and chemical composition were constructed by simultaneous codeposition of the molecules from solution (“grafting to”). We characterize these layers by measuring their wettability (using contact angle goniometry, CA), thickness (using variable angle spectroscopic ellipsometry, VASE), and chemical composition (using near-edge x-ray absorption fine structure spectroscopy, NEXAFS). Variations in the ratio of aromatic to aliphatic

molecules in the deposition solution resulted in SAMs with fine-tuned compositions and thicknesses.

We used mixed SAMs to control the adsorption of asphaltenes onto silicon substrates. Asphaltenes, a petroleum-derived class of molecules that tend to aggregate in solution, are highly polar, aromatic, and surface active. The thickness and chemical composition of the asphaltene treated SAMs were characterized by VASE and NEXAFS, respectively. We find that SAMs that expose the underlying polar silica substrate promote the adsorption of asphaltenes, while SAMs that shield the polar silica layer largely prevent the adsorption.

In the second part of this dissertation, we investigate surface-initiated CRP by Monte Carlo computer simulation. In surface-initiated CRP, polymerization starts directly from a SAM of initiating molecules on a surface. A computer model of the surface-initiated CRP reaction is developed and a stochastic algorithm based on the bond-fluctuation model is implemented. We explore the effect of the grafting density of initiators and the solvent quality on polymer properties such as the average molecular weight, root-mean squared radius of gyration, and polydispersity index. We find that confining the initiators by placing them on the surface or by performing the simulation in poor solvent conditions leads to decreased polymerization rate and increased polydispersity index. Our results

suggest that the assumption that solution- and surface-initiated polymers have equivalent properties is seldom valid.

We also study the simultaneous polymerization of surface- and bulk-initiated polymers. The competition between these two polymer populations for a limited supply of free monomers affects the properties of both classes of polymers. The effect that this competition has on the polymer properties depends on the fraction of polymers on the surface, the grafting density of initiators and the initial number of free monomers. We find that increasing the number of fast-growing bulk initiators limits the growth of the slow-growing, surface-confined chains, which results in different molecular weight distributions of bulk- and surface-initiated polymers.

Controlling Surface Properties of Materials by Small Molecule and Polymer  
Grafts

by  
Salomon Turgman Cohen

A dissertation submitted to the Graduate Faculty of  
North Carolina State University  
in partial fulfillment of the  
requirements for the Degree of  
Doctor of Philosophy

Chemical Engineering

Raleigh, North Carolina

2011

APPROVED BY:

---

Jan Genzer  
Chair of Advisory Committee

---

Peter K. Kilpatrick  
Co-chair of Advisory Committee

---

Orlin D. Velev

---

Stefan Franzen

## DEDICATION

To my parents Raquel and Samuel  
your counsel, teachings, and sacrifices made this achievement possible  
*sus consejos, enseñanzas, y sacrificios hicieron esta meta posible*

My siblings Esther and Rafael  
the experiences we shared helped form my character and thoughts  
*las experiencias que compartimos ayudaron a formar mi carácter y pensamientos*

And especially to my wife Katarzyna  
my closest and strongest supporter throughout this journey

## **BIOGRAPHY**

Salomon Turgman Cohen was born to Raquel Cohen and Samuel Turgman in Maracay, Venezuela. Two years later, he moved to Panama City, Panama where he grew up. He shared the home with his dear younger siblings Esther and Rafael, who through the years were great companions and friends to Salomon. Raquel and Samuel encouraged Salomon's interest in mathematics, science, and computers from an early age. They provided him with programming courses and wonderful chemistry kits.

Salomon completed primary and secondary school at the Instituto Alberto Einstein, where he had the privilege to share 12 years in the company of forty wonderful classmates. He got to know this group of classmates as his own brothers and sisters and they had a tremendous influence on Salomon's formative years. At school, his teachers fostered Salomon's love for the fields of mathematics and science.

After completing secondary studies, Salomon enrolled in the Chemical Engineering program at Purdue University in West Lafayette, IN. Through his years as an undergraduate student, professors Igal Szleifer and James M. Caruthers introduced Salomon to the wonderful world of scientific research.

After completing his undergraduate education, Salomon decided to pursue graduate studies at North Carolina State University in Raleigh, NC. Under the mentorship of Jan Genzer and Peter K. Kilpatrick, he pursued research on surface and polymer science.

## **ACKNOWLEDGMENTS**

First, I would like to thank my mentors Prof. Jan Genzer and Prof. Peter K. Kilpatrick. You challenged me to excel, provided encouragement when times were difficult, and always gave me sound advice. I cannot dream of better advisors. Special thanks to Dr. Matthew Smith, Dr. Vincent Verruto, and Mr. Ali Evren Ozcam. You taught me much by your example. Your dedicated work ethic, ability to judge honestly your own work, and your capacity to differentiate between work time and play time are lessons that will remain with me forever. Thanks for your camaraderie and companionship during numerous meals, trips to scientific conferences and experimental facilities, and for your sound advice when times got tough. Thanks to the staff of beamline U7A at Brookhaven National Laboratories, Drs. Daniel Fischer and Cherno Jaye, for maintaining a finely tuned machine for us to break and for assisting us in our experiments no matter the time of day (or night). To the Kilpatrick and Genzer research groups, thank you for your support throughout this epic journey, I can only hope that I contributed as much to your careers as you did to mine. Thanks to the staff in the Chemical and Biomolecular Engineering Department. You helped me navigate smoothly the road through the CBE department and through NCSU.

I would like to acknowledge my parents Raquel Cohen and Samuel Turgman whose sacrifices, teachings, and counsel made this achievement possible. Sending a son to a different world, to pursue his dreams and aspirations, is an enormous sacrifice that I will never forget. Thank you for all you have done. Thanks to my siblings Esther and Rafael. Growing up with you was an amazing experience and I miss every moment we shared. Thank you for all the support and excitement you always showed for all my accomplishments. My deepest gratitude is for my wife Katarzyna. You have been there from the beginning as my closest and strongest supporter. You have been my partner throughout this journey and your company, support, and love are a big part of this achievement. I hope to deserve always your love and admiration.

## TABLE OF CONTENTS

<b>LIST OF TABLES.....</b>	<b>xii</b>
<b>LIST OF FIGURES.....</b>	<b>xiii</b>
<b>CHAPTER 1 Introduction.....</b>	<b>1</b>
1.1. Self-assembled monolayers for adsorption studies .....	1
1.2. Kinetics of “grafting from” polymer graft formation .....	4
1.3. References .....	8
<b>CHAPTER 2 Asphaltene Adsorption onto Self-Assembled Monolayers of Mixed Aromatic and Aliphatic Trichlorosilanes .....</b>	<b>10</b>
2.1. Abstract .....	10
2.2. Introduction .....	11
2.3. Materials and Methods .....	17
2.3.1. Materials.....	17
2.3.2. Sample preparation.....	18

2.3.3.	Contact angle measurements .....	20
2.3.4.	Spectroscopic ellipsometry .....	21
2.3.5.	Near-edge x-ray absorption fine structure (NEXAFS) spectroscopy .....	22
2.4.	Results and Discussion .....	25
2.5.	Conclusions .....	45
2.6.	References .....	46

**CHAPTER 3 Asphaltene Adsorption onto Self-Assembled Monolayers  
of Alkyltrichlorosilanes of Varying Chain Length.....51**

3.1.	Abstract .....	51
3.2.	Introduction .....	52
3.3.	Materials and Methods .....	59
3.3.1.	Materials.....	59
3.3.2.	Sample preparation.....	60
3.3.3.	Spectroscopic ellipsometry.....	61
3.3.4.	Contact angle measurements.....	62
3.3.5.	Near-edge x-ray absorption fine structure (NEXAFS) spectroscopy.....	63
3.4.	Results and Discussion .....	65

3.5.	Conclusions .....	85
3.6.	References .....	86
<b>CHAPTER 4</b>	<b>Computer simulation of controlled radical polymerization: Effect of chain confinement due to initiator grafting density and solvent quality in “grafting from” method .....</b>	<b>92</b>
4.1.	Abstract .....	92
4.2.	Introduction .....	93
4.3.	Simulation Model.....	100
4.4.	Results and Discussion .....	106
	4.4.1. Solvent quality .....	106
	4.4.2. Surface Density .....	110
4.5.	Conclusions .....	129
4.6.	References .....	132
<b>CHAPTER 5</b>	<b>Computer simulation of simultaneous bulk- and surface-initiated controlled radical polymerization.....</b>	<b>138</b>
5.1.	Introduction.....	138
5.2.	Simulation Model and Algorithm.....	141

5.3.	Results and Discussion .....	146
5.4.	Conclusions .....	165
5.5.	References .....	167
<b>CHAPTER 6</b>	<b>Outlook and Future Work .....</b>	<b>170</b>
6.1.	Polymerization from various geometries.....	170
6.2.	Molecular weight distribution of polymers (Schulz–Zimm).....	172
6.3.	Effects of termination and chain transfer .....	173
6.4.	Experimental studies mimicking the simulations.....	174
6.4.1.	Size exclusion chromatography with refractive index detection.....	174
6.4.2.	Size exclusion chromatography with fluorescence detection.....	177
6.5.	References .....	178
<b>APPENDICES</b>	<b>.....</b>	<b>180</b>
<b>APPENDIX A</b>	<b>NEXAFS and Ellipsometry for Spun-Coated Asphaltenes .</b>	<b>181</b>
<b>APPENDIX B</b>	<b>Determining the escape depth for PEY NEXAFS .....</b>	<b>184</b>
B.1.	References .....	188

<b>APPENDIX C</b>	<b>Mapping the coil-to-globule transition and the effects of</b>	
	<b><math>P_r</math></b> .....	<b>190</b>
C.1.	Mapping the coil-to-globule transition .....	190
C.2.	Probability of reaction versus motion .....	192
<b>APPENDIX D</b>	<b>Simulation Model</b> .....	<b>194</b>
<b>APPENDIX E</b>	<b>Finding the instantaneous shape of a polymer coil</b> .....	<b>199</b>
E.1.	References .....	201

## LIST OF TABLES

<b>Table 4.1.</b>	Lattice dimensions and the corresponding values of $\sigma$ .....	102
<b>Table 4.2.</b>	Degrees of polymerization (N) and polydispersity indices (PDI) compared to those obtained by fitting the Schulz–Zimm distribution to the simulation data at several $\sigma$ and both solvent conditions.....	128
<b>Table 5.1.</b>	Parameters adjusted in order to correctly change $M_0$ .....	143
<b>Table 5.2.</b>	Datasets truncated to avoid interaction with opposing substrate. $\text{Max}(x_m)$ denotes value of $x_m$ at which truncation occurred. Datasets not displayed were not truncated. ....	146
<b>Table 6.1.</b>	Common SEC solvents and their $dn/dc$ when paired with common polymers. Obtained from <a href="http://www.ampolymer.com">http://www.ampolymer.com</a> .....	176
<b>Table D.1.</b>	List of input parameters needed for the simulation algorithm and their default values.....	197

## LIST OF FIGURES

- Figure 2.1.** PEY NEXAFS spectra collected at the carbon K-edge at the “magic” angle of incidence ( $\theta = 50^\circ$ , where  $\theta$  is the angle between the sample normal and the electric vector of the x-ray beam) for the pure component trichlorosilane SAMs. The inset depicts a shift of  $\approx 0.15$  eV between the  $1s \rightarrow \pi_{C=C}^*$  peak positions in the NEXAFS spectra of the PTS and PETS SAMs. .... 24
- Figure 2.2.** NEXAFS spectra collected at the carbon K-edge for mixed SAMs (left), asphaltene-treated mixed SAMs (center), and the difference between these two spectra (right). The sample compositions (percentage PTS/percentage ODTS) in the PTS/ODTS SAM correspond (from top to bottom) to 100/0, 85/15, 15/85, 7.5/92.5, and 0/100. .... 25
- Figure 2.3.** Advancing contact angle (■, left ordinate) and contact angle hysteresis (⊞, right ordinate) as a function of aromatic fraction in deposition solution for: a) PTS:BTS, b) PETS:BTS, c) PTS:ODTS, and d) PETS:ODTS. The error bars are smaller than the sizes of the symbols. The lines are meant to guide the eye. .... 26

- Figure 2.4.** SAM thickness as a function of aromatic mole fraction in the deposition solution for a) PTS:BTS, b) PETS:BTS, c) PTS:ODTS, and d) PETS:ODTS (d). The lines are meant to guide the eye..... 28
- Figure 2.5.** Normalized  $1s \rightarrow \pi_{C=C}^*$  peak area in the carbon K-edge NEXAFS spectra as a function of aromatic mole fraction in the deposition solution for bare SAMs (■) and HOW asphaltene-treated SAMs (⊕) for a) PTS:BTS, b) PETS:BTS, c) PTS:ODTS, and d) PETS:ODTS. The lines are meant to guide the eye. .... 31
- Figure 2.6.** The  $1s \rightarrow \pi_{C=C}^*$  peak position in the carbon K-edge NEXAFS spectra as a function of aromatic mole fraction in the deposition solution for bare SAMs (■) and HOW asphaltene-treated SAMs (⊕) for a) PTS:BTS, b) PETS:BTS, d) PTS:ODTS, and d) PETS:ODTS. The lines are meant to guide the eye. .... 33
- Figure 2.7.** The thickness of the adsorbed asphaltene film determined by ellipsometry as a function of aromatic fraction in the deposition solution for PTS:BTS (⊕), PETS:BTS (⊞), PTS:ODTS (●) and PETS:ODTS (■) mixed SAMs. The grey symbols represent repeat experiments for PTS:ODTS (squares) and PETS:ODTS (circles). The lines are meant to guide the eye..... 42

**Figure 2.8.** The asphaltene film thickness plotted as a function of the thickness of the underlying SAM for PTS:BTS ( $\oplus$ ), PETS:BTS ( $\boxplus$ ), PTS:ODTS ( $\bullet$ ) and PETS:ODTS ( $\blacksquare$ ). The marker size represents the degree of aromaticity (increasing marker size corresponds to increasing degree of aromaticity) of a given data point. The size of each symbol increases proportionally with increasing aromaticity of the SAM solution. The grey symbols represent repeat experiments for PTS:ODTS (squares) and PETS:ODTS (circles). The line is meant to guide the eye. .... 44

**Figure 3.1.** Partial electron yield (PEY, top) and fluorescence yield (FY, bottom) NEXAFS spectra at the “magic” angle of incidence ( $\theta = 55^\circ$ , where  $\theta$  denotes the angle between the surface normal and the electric vector of the x-ray beam) for alkyltrichlorosilanes of varying chain length: n-butyltrichlorosilane ( $\text{—}$ ), n-octyltrichlorosilane ( $\text{--}$ ), n-decyltrichlorosilane ( $\text{----}$ ), n-dodecyltrichlorosilane ( $\text{---}$ ), n-hexadecyltrichlorosilane ( $\text{- - -}$ ), n-octadecyltrichlorosilane ( $\text{- - - -}$ ). The pre-edge region of all the PEY spectra (around 280 eV) has been shifted up by 0.1 a.u. vertically for clarity. .... 64

- Figure 3.2.** The thicknesses of the SAM measured by ellipsometry as a function of  $N_c$  for experiments collected during different times: November 2007 ( $\square$ ), March 2008 ( $\circ$ ) and April 2008 ( $\triangle$ ). The grey bars represent the range of thicknesses reported by Wasserman et al.<sup>39</sup> The dotted line represents the best linear fit through the data. .... 67
- Figure 3.3.** The PEY (a) and FY (b) NEXAFS edge jump as a function of  $N_c$  for bare SAMs (open symbols) and asphaltene-treated SAMs (closed symbols). The data presented have been collected during various time periods: March 2007 (triangles), November 2007 (squares) and March 2008 (circles). The PEY and FY signals corresponding to bare silica treated with asphaltenes are shown for comparison (a half-filled symbol at  $N_c = 0$ ). .... 69
- Figure 3.4.** The advancing contact angle (top) and the contact angle hysteresis (bottom) as a function of  $N_c$  are shown for the March 2008 ( $\circ$ ) and April 2008 ( $\triangle$ ) experiments. The grey bars represent the range of contact angles reported by Wasserman et al.<sup>39</sup> ..... 71
- Figure 3.5.** The thickness (open symbols, left ordinate) and the FY NEXAFS edge jump of asphaltene layers (closed symbols, right ordinate)

adsorbed from toluene solutions and as a function of  $N_c$  in the underlying SAM. While the asphaltene layer thicknesses were measured directly by ellipsometry, the FY NEXAFS data were obtained by subtracting FY NEXAFS values collected from bare SAMs from those of the SAM/asphaltene specimens. The various symbols corresponds to data collected in November 2007 ( $\square$  and  $\blacksquare$ ) and April 2008 ( $\triangle$ ). ..... 78

**Figure 3.6.** Schematics of asphaltenes adsorbed on alkyltrichlorosilane modified silica substrates. a) Variations in adsorption with increased thicknesses, b) variations in thickness of adsorbed asphaltenes when decreasing solvent quality. .... 79

**Figure 3.7.** The thickness of the asphaltene adsorbed film as a function of the negative cosine of the SAM advancing DI water contact angle collected in the March 2008 ( $\bullet$ ) and April 2008 ( $\blacktriangle$ ) experiments are shown for various solvents including: (a) toluene, (b) tetralin, (c) methylnaphthalene..... 81

**Figure 3.8.** (a) Thickness of the asphaltene adsorbed film before (closed symbols) and after (open symbols) sonication in parent neat solvent and (b) the aggregate size (aggregate diameter: crossed symbols, aggregate thickness: open symbols, aggregate average

radius of gyration: closed symbols) as a function of the Hildenbrand solubility parameter of the solvent. The solvents used are heptol (cyan diamond), decalin (blue down-triangle), toluene (green up-triangle), tetralin (red circle) and 1-methylnaphthalene (black square). The composition of heptol in samples in Figure 3.8a is 20:80 (w/w), while that in samples in Figure 3.8b is 60:40 (v/v). The data in Figure 3.8b have been adopted from.<sup>22</sup>..... 83

**Figure 4.1.** a) Radius of gyration and b) polydispersity index of bulk polymers in good (blue squares,  $\epsilon = 4 \times 10^{-7} \text{ k}_B\text{T}$ ) and poor (red circles,  $\epsilon = 4 \times 10^{-1} \text{ k}_B\text{T}$ ) solvent conditions as a function of monomer conversion.....107

**Figure 4.2.** Average number of nearest neighbor sites per active end occupied by free monomers ( $\theta_m$ ), polymers ( $\theta_p$ ), polymers belonging to a different chain ( $\theta_{p,o}$ ), polymer belonging to the observed chain ( $\theta_{p,s}$ ) and the remaining empty sites ( $\theta_e$ ) for bulk polymerization under good (solid,  $\epsilon = 4 \times 10^{-7} \text{ k}_B\text{T}$ ) and poor (dashed,  $\epsilon = 4 \times 10^{-1} \text{ k}_B\text{T}$ ) solvent conditions.....109

**Figure 4.3.** Parallel ( $R_{g,\parallel}$ , closed symbols) and perpendicular ( $R_{g,\perp}$ , open symbols) components of the average radius of gyration of

grafted chains as a function of monomer conversion for good (left column,  $\epsilon = 4 \times 10^{-7} k_B T$ ) and poor (right column,  $\epsilon = 4 \times 10^{-1} k_B T$ ) solvent conditions at three different grafting densities ( $\sigma$ ): 0.08 (top row, magenta), 0.16 (middle row, green) and 0.44 (bottom row, black). The dashed lines represent corresponding data for chains polymerized in bulk. ....112

**Figure 4.4.** Initiator efficiency as a function of monomer conversion for a) good ( $\epsilon = 4 \times 10^{-7} k_B T$ ) and b) poor ( $\epsilon = 4 \times 10^{-1} k_B T$ ) solvent conditions at various grafting densities ( $\sigma$ ): 0.06 ( $\blacktriangleleft$ ), 0.08 ( $\blacklozenge$ ), 0.11 ( $\blacktriangledown$ ), 0.16 ( $\blacktriangle$ ), 0.25 ( $\bullet$ ), and 0.44 ( $\blacksquare$ ). ....115

**Figure 4.5.** Chain length distributions for surface initiated polymerizations as a function of monomer conversion ( $x_m$ , ordinate) for good (left column,  $\epsilon = 4 \times 10^{-7} k_B T$ ) and poor (right column,  $\epsilon = 4 \times 10^{-1} k_B T$ ) solvent conditions at three grafting densities ( $\sigma$ ): 0.08 (top, magenta), 0.16 (middle, green) and 0.44 (bottom, black). The dark areas represent high frequency of a specific chain length and light colors low frequency. The lines represent slices of these distributions and their ordinate value represent the frequency at a given chain length. ....117

**Figure 4.6.** Polydispersity index (PDI) of grafted chains as a function of monomer conversion for good (a,  $\epsilon = 4 \times 10^{-7} \text{ k}_B\text{T}$ ) and poor (b,  $\epsilon = 4 \times 10^{-1} \text{ k}_B\text{T}$ ) solvent conditions at various grafting densities ( $\sigma$ ): 0.06 ( $\blacktriangleleft$ ), 0.08 ( $\blacklozenge$ ), 0.11 ( $\blacktriangledown$ ), 0.16 ( $\blacktriangle$ ), 0.25 ( $\bullet$ ), and 0.44 ( $\blacksquare$ ). The dotted black lines represent the PDI values for chains polymerized in bulk. ....118

**Figure 4.7.** Average number of nearest neighbor sites per active end occupied by monomers ( $\theta_m$ , top row), polymers ( $\theta_p$ , middle row), wall ( $\theta_w$ , bottom row) as a function of monomer conversion for good (left column,  $\epsilon = 4 \times 10^{-7} \text{ k}_B\text{T}$ ) and poor (right column,  $\epsilon = 4 \times 10^{-1} \text{ k}_B\text{T}$ ) solvent conditions. The solid lines represent values corresponding to various grafting densities: 0.08 (magenta), 0.16 (green), and 0.44 (black). The dark grey dashed lines represent the corresponding values for chains polymerized in bulk. ....121

**Figure 4.8.** Volume fraction of grafted chains (left column, black), monomers (middle column, red), and chain-ends (right column, green) expressed as a function of the distance from the wall (abscissa,  $z$ ) vs. monomer conversion (ordinate,  $x_m$ ) under good ( $\epsilon = 4 \times 10^{-7} \text{ k}_B\text{T}$ ) solvent conditions at three grafting densities: 0.08 (top row), 0.16 (middle row), and 0.44 (bottom row). ....123

- Figure 4.9.** Volume fraction of grafted chains (left column, black), monomers (middle column, red), and chain-ends (right column, green) expressed as a function of the monomer conversion ( $x_m$ ) vs. the distance from the wall ( $z$ ) under poor ( $\varepsilon = 4 \times 10^{-1} k_B T$ ) solvent conditions at three grafting densities: 0.08 (top row), 0.16 (middle row), and 0.44 (bottom row). ..... 124
- Figure 4.10.** Volume fraction profiles of grafted chains (■), monomers (●), and chain-ends (▲) for good (left column,  $\varepsilon = 4 \times 10^{-7} k_B T$ ) and poor (right column,  $\varepsilon = 4 \times 10^{-1} k_B T$ ) solvent conditions at three grafting densities: 0.08 (top row), 0.16 (middle row), and 0.44 (bottom row). ..... 125
- Figure 4.11.** Volume fraction profiles for monodisperse (squares) and polydisperse (triangles, PDI listed in the legend) for good (left column,  $\varepsilon = 4 \times 10^{-7} k_B T$ ) and poor (right column,  $\varepsilon = 4 \times 10^{-1} k_B T$ ) solvents at three grafting densities: 0.11 (top row), 0.16 (middle row) and 0.25 (bottom row). Profiles were obtained at  $x_m$  values of 0.26 and 0.58 for  $N$  equal to 10.1 and 20.1 respectively. .... 126

- Figure 5.1.** Top view of the lattices used in this study for various  $\sigma$  and  $\eta$ . The dots indicate the positions of the grafting points on the surface. ....142
- Figure 5.2.** Average molecular weight for bulk (top row) and surface (bottom row) polymers as a function of monomer conversion with initial number of monomers ( $M_o$ ) of 25000; percentages of surface polymers ( $\eta$ ): 6% (left column), 49% (middle column) and 90% (right column); grafting densities of initiators ( $\sigma$ ) : 0.08 (red), 0.16 (green) and 0.25 (blue). The black dashed lines represent the  $\eta = 100\%$  and  $M_o = 25000$  conditions. The  $\eta = 90\%$  data is truncated because the brush starts interacting with the opposite impenetrable surface. ....147
- Figure 5.3.** Number average molecular weight (top row) and the same quantity scaled (bottom row) for bulk (left column, red,  $\eta = 0\%$ ) and surface (right column, blue,  $\eta = 100\%$ ) polymers as a function of Monte Carlo steps per bead for initial number of monomers ( $M_o$ ): 6250 (squares), 12500 (circles), and 25000 (triangles); grafting density of initiators ( $\sigma$ ): 0.08 (hollow), 0.16 (cross), and 0.25 (ex). The purple and dark blue lines are guides to the eye for the bulk- and surface-initiated data, respectively. 149

**Figure 5.4.** Scaled number average molecular weight as a function of Monte Carlo step per bead for bulk (red) and surface (blue) polymers with fraction of surface polymers ( $\eta$ , left to right columns): 6%, 49%, and 90%; initiator grafting densities ( $\sigma$ , top to bottom rows): 0.08, 0.16, and 0.25; initial number of monomers ( $M_o$ ): 6250 (squares), 12500 (circles), and 25000 (triangles). The solid lines correspond to  $\eta = 0\%$  (purple) and  $\eta = 100\%$  (dark blue). 151

**Figure 5.5.** Initial polymerization rate as a function of  $\sigma$  for bulk (open symbols, top row) and surface (close symbols, bottom row) for  $\eta$  equal to 6% (left column), 49% (middle column), and 90% (right column) and  $M_o$  equal to 6250 (red down triangle), 12500 (blue diamond), and 25000 (green left triangle). For clarity, the data for  $M_o=6250$  and  $M_o=25000$  have been shifted horizontally by a small arbitrary increment to the left and right, respectively. The dotted lines in the top and bottom rows represent  $\eta = 0\%$  (bulk-only polymerization and 100% (surface-only polymerization) , respectively. The solid vertical lines in the top row at  $\sigma = 0$  denote the range of the  $\eta = 0\%$  data..... 153

**Figure 5.6.** Number average molecular weight of surface polymers as a function of number average molecular weight of bulk polymers

for the three values of  $M_o$  (top row) and for  $M_o = 6250$  (bottom row). Percentage of surface polymers ( $\eta$ ): 6% (left column), 49% (middle column), and 90% (right column); initial number of free monomers ( $M_o$ ): 6250 (squares), 12500 (circles), and 25000 (triangles); grafting density of initiators ( $\sigma$ ): 0.08 (red), 0.16 (green), and 0.25 (blue). The dashed line represents  $\langle N \rangle_s = \langle N \rangle_b$ .....155

**Figure 5.7.** Polydispersity index for bulk (top row) and surface (bottom row) polymers as a function of monomer conversion with initial number of monomers ( $M_o$ ) of 25000; percentages of surface polymers ( $\eta$ ): 6% (left column), 49% (middle column) and 90% (right column); grafting densities of initiators ( $\sigma$ ) : 0.08 (red), 0.16 (green) and 0.25 (blue). The black dashed lines represent the  $\eta = 0\%$  (top row) and  $\eta = 100\%$  (bottom row),  $M_o = 25000$  and  $\sigma = 0.08, 0.16$  and  $0.25$  conditions.....158

**Figure 5.8.** The PDIs of bulk (top) and surface (bottom) polymers as a function of the monomer conversion for  $\eta = 49\%$ . Initiator grafting densities ( $\sigma$ ): 0.08 (red), 0.16 (green) and 0.25 (blue); initial number of free monomers ( $M_o$ ): 6250 (squares), 12500 (circles) and 25000 (triangles).....160

- Figure 5.9.** The PDIs of bulk (top) and surface (bottom) polymers as a function of the average molar mass of bulk and surface polymers, respectively, for  $\eta = 49\%$ . Initiator grafting densities ( $\sigma$ ): 0.08 (red), 0.16 (green) and 0.25 (blue); initial number of free monomers ( $M_0$ ): 6250 (squares), 12500 (circles) and 25000 (triangles). The black dashed lines represent the  $\eta = 0\%$  (top) and  $\eta = 100\%$  (bottom),  $M_0 = 25000$  and  $\sigma = 0.08, 0.16$  and  $0.25$  conditions.....162
- Figure 6.1.** Schematic of polymers grafted to surfaces of various geometries. The squares represent the difference in shapes of equivalent chains with different orientation. This difference in the dimensions of the chains leads to issues in characterizing these chains solely by measuring the radius of gyration.....171
- Figure A.1.** Ellipsometry data for spun-coated asphaltenes. See text for details.....182
- Figure A.2.** PEY NEXAFS spectra collected from Hondo asphaltenes spin-coated onto a silicon wafer.....183
- Figure B.1.** The edge jump of the trichlorosilane SAMs as a function of the adjusted SAM thickness for (a) PEY NEXAFS and (b) FY NEXAFS.

	The solid line in Figure A.1a represents a best fit to equation A.1, the solid line in Figure A.1b is meant to guide the eye.....	185
<b>Figure B.2.</b>	Schematic showing a simple model, from which equation B.1 can be derived.....	186
<b>Figure C.1.</b>	Radius of gyration of a single coil in the bulk (a) and grafted to the surface (b) with degree of polymerization: 10 (■), 20 (●), 30 (▲), 40 (▼), and 50 (◆) as a function of polymer solubility expressed in terms of the reduced inverse temperature. ....	191
<b>Figure C.2.</b>	Average number of sites nearest neighbors to the chain-ends occupied by monomer as a function of monomer conversion for bulk-initiated systems in good solvent consisting of $I_0 = 100$ and $M_0 = 3125$ at various values of $P_r$ .....	192
<b>Figure C.3.</b>	Polydispersity index as a function of monomer conversion for bulk-initiated systems in good solvents consisting of $I_0 = 100$ and $M_0 = 3125$ at various values of $P_r$ .....	193
<b>Figure D.1.</b>	Flow chart of the simulation algorithm.....	195

## **CHAPTER 1**

### **INTRODUCTION**

The modification of surface properties of materials is an important technological step in many modern applications. Relevant characteristics of surfaces include chemical composition, roughness, surface modulus, surface charge, mobility of surface groups and many other attributes. These properties affect the performance of materials (and their surfaces) in applications such as colloidal stabilization, adhesion, lubrication, bio-sensing, and anti-fouling. One type of modification involves the physical or chemical attachment of molecules to the surface in order to achieve certain functionality or property enhancement. This chemical modification can impart changes in the wettability and lubricity of the surface, and, among other properties, they can also affect the adsorption of molecules onto the surface and induce changes on these adsorbed layers.

#### **1.1. Self-assembled monolayers for adsorption studies**

Deposition of self-assembled monolayers<sup>1-8</sup> (SAMs) on surfaces represents one type of chemical surface modification method. In this technique, a thin layer

of small molecules assembles spontaneously at an interface given the right balance of intermolecular, adsorbate/substrate and adsorbate/solvent interactions and typically reacts chemically with the underlying substrate. Two types of chemistries widely used for the synthesis of SAMs are organosulfur molecules on gold or other noble metal substrates and alkyl silanes on hydroxylated surfaces. Sulfur-based SAMs (i.e., thiolates, disulfides) are easy to fabricate in a well-defined manner. Because of this, the kinetics of formation and the structure of alkanethiol-based SAMs have been investigated extensively. Despite their ease of formation, these structures are unstable for example to exposure to UV light and in exchange reactions with other sulfur containing molecules. Organosilane chemistries on silica are also widely used in the literature, primarily due to their high structural stability. These SAMs are relatively stable to changes in temperature, solvents, exposure to acidic or basic conditions, and physical treatments (i.e. sonication). Their disadvantage is that the deposition conditions (i.e., solvent type or temperature) at which these SAMs are formed need to be controlled carefully. Silane based SAMs form by condensation with surface-bound hydroxyls and, in cases of di- or tri-functional molecules, through in-plane Si-O-Si - linkages; the latter further stabilize the SAM structure on the substrate. In the presence of excess moisture in the solution (i.e. toluene saturated with water), the formation of trichlorosilane

aggregates in solution leads to multilayer formation on the surface. In the absence of enough moisture, however, the hydration reaction of the silane moieties does not take place and the result is a partially covered, low quality monolayer.

The aim of **Chapter 2** and **3** of this dissertation is to explore the applicability of organosilane SAMs to tune the adsorption properties of complex asphaltene molecules on solid substrates. Specifically, we employ SAMs of trichlorosilanes on silicon substrates due the aforementioned stability improvements over their alkanethiol counterparts. This will ensure that under the conditions of the adsorption experiments, the SAMs will not change their structure and composition. To gain additional control of the surface properties, we will form binary SAMs consisting of molecules with different chemical end-groups. In this manner, we can tune the chemical composition of the surface coating and its affinity to the adsorbate molecules. We will show that it is possible to control the chemical composition and the thickness of the SAMs by varying the chemical composition of the co-adsorbing trichlorosilane molecules in the solution. We also describe the dependence of the adsorption process of asphaltenes on the composition and thickness of the SAM layer. In this manner, we identify the characteristics of the SAM that promote or prevent molecular adsorption depending on the application of interest.

## 1.2. Kinetics of “grafting from” polymer graft formation

A second type of chemical modification involves the grafted polymer layer. These structures are similar to a SAM in that they involve chemical attachment of molecules onto the surface. Here, however, the molecules involved are very large (and in many cases linear) chains comprising many monomers linked covalently. Grafted polymers provide additional parameters to tune the surface properties such as the molecular weight (and hence the length) of the grafts and convenient means of varying the composition by incorporating more than a single monomer into the macromolecular graft. The rich phase behavior of polymers can provide means to produce surfaces responsive to a variety of stimuli such as solvent, pH and temperature changes. Compared to SAMs, grafted polymer layers are often thicker and more mobile, but their number density of molecules per unit area on the surface is lower.

The typical procedure for the formation of SAMs involves exposing a well-cleaned gold or hydroxylated surface to a solution with a low concentration ( $\mu\text{M}$ ) of the adsorbing molecules. We call this the “grafting onto” approach. In the case of alkanethiols on gold, there is an initial fast stage of adsorption where the interaction between the sulfur head-group and the underlying substrate drives the adsorption process. The second stage of SAM formation involves the rearrangement of the alkyl chains within the monolayer to form a well-packed

structure. This second stage is slower and is driven by the competition between chain-chain interaction (typically van der Waals interactions for alkanes or molecules without a significant contribution of special interactions, i.e., charged, hydrogen bonding,  $\pi$ - $\pi$ , etc) and the conformational entropy of the SAM forming molecules (gauche defects or all-trans configuration). As the size of the SAM forming molecules increases (or in case they are bulky), these two adsorption stages become coupled and the chain conformations of the already adsorbed molecules start affecting the accessibility of additional reactive groups to the surface. An analogous “grafting onto” method can be used in the synthesis of grafted polymer layers. In this case, the polymers synthesized in solution are modified to include end-groups that can interact (chemically or physically) with the solid substrate. Opposed to the small molecule case, long polymer chains adsorbing on the surface will sterically prevent each other from adsorbing and forming a densely packed polymer layer. Furthermore, obtaining all-trans configurations of long polymer chains involves an immense entropic penalty (unless they tend to crystallize). The energetic terms that govern the adsorption process in the adsorption of macromolecules are then the strength of the end-group/substrate interaction, the entropic penalty of stretching the chain, and the solvent quality during the deposition solvent. Due to steric limitations, the

“grafting onto” approach can only achieve limited grafting densities in the synthesis of grafted polymers.

The “grafting from”<sup>9-20</sup> method circumvents this grafting density limitation. The “grafting from” technique involves the deposition of small-molecule polymerization initiators on the surface and the polymerization of long macromolecules directly from the substrate-bound initiator sites. Ideally, all the chains grow simultaneously, thus forming a dense assembly of highly stretched polymers and preventing the steric limitations of the “grafting onto” approach. Although, in principle, this method is capable of producing grafted polymer layers with surface densities larger than with the “grafting onto” technique, it also has the disadvantage that the properties of the grafted chains (i.e. the molecular weight distribution) are difficult to characterize in-situ with the currently available experimental techniques. A typical approach is then to assume that the properties of the grafted chains are similar to the properties of polymers grown with identical methods in bulk solutions.

Our aim in **Chapters 4** and **5** is to use computer simulations to study the “grafting from” method for the synthesis of tethered polymer layers. We do this by modeling the controlled radical polymerization process, a scheme often used to synthesize these grafted layers. This type of polymerization allows for relatively precise control of the average molecular weight (or alternatively layer

thickness in the case of the surface-bound polymers) and the polydispersity of the length of growing chains. Although these types of reactions have been studied widely in bulk solutions, technical challenges have prevented the full characterization of their kinetics when the initiators are confined to a flat surface. The computer simulations herein presented reveal information about the rates of polymerization, average molecular weights, polydispersity index, and the various factors that affect these properties in surface-initiated polymerizations. In **Chapter 4**, we compare the characteristics of bulk- and surface-initiated polymerizations and their dependence on parameters such as the density of grafted chains and the polymer solvent quality. In **Chapter 5**, we study the simultaneous polymerization of bulk- and surface-initiated polymers and discuss how the competition between these two classes of chains can alter their molecular weight distribution during the polymerization. The information thus obtained serves several purposes. First, it highlights the need to develop analytical techniques capable of in-depth characterization of the grafted polymer layers and the direct measurement of their properties. One such method to characterize experimentally the grafted polymers will be described in **Chapter 6.4** (future work and outlook). Second, it probes the validity of the assumption that the bulk- and surface- initiated polymers have similar properties, and that the characteristics of bulk polymers offer good estimates to those of the surface.

Finally, the trends observed for the molecular weight distribution as a function of the various parameters tested provide a guide for the experimental design of dense polymer graft with controlled molecular weight distributions and polydispersity index.

### 1.3. References

1. Ulman, A. In *An introduction to ultrathin organic films : from Langmuir-Blodgett to self-assembly*; Academic Press: Boston, 1991; pp 442.
2. Dubois, L. H.; Nuzzo, R. G. Synthesis, Structure, and Properties of Model Organic Surfaces. *Annu. Rev. Phys. Chem.* **1992**, *43*, 437-463.
3. Mrksich, M.; Whitesides, G. M. Using Self-Assembled Monolayers to Understand the Interactions of Man-made Surfaces with Proteins and Cells. *Annu. Rev. Biophys. Biomol. Struct.* **1996**, *25*, 55-78.
4. Ulman, A. Formation and Structure of Self-Assembled Monolayers. *Chem. Rev.* **1996**, *96*, 1533-1554.
5. Poirier, G. E. Characterization of Organosulfur Molecular Monolayers on Au(111) using Scanning Tunneling Microscopy. *Chem. Rev.* **1997**, *97*, 1117-1128.
6. Xia, Y. N.; Whitesides, G. M. Soft Lithography. *Annu. Rev. Mat. Sci.* **1998**, *28*, 153-184.
7. Schreiber, F. Structure and Growth of Self-Assembling Monolayers. *Prog. Surf. Sci.* **2000**, *65*.
8. Krämer, S.; Fuierer, R. R.; Gorman, C. B. Scanning Probe Lithography using Self-Assembled Monolayers. *Chem. Rev.* **2003**, *103*, 4367-4418.
9. Milner, S. T. Polymer Brushes. *Science (New York, N.Y.)* **1991**, *251*, 905-914.

10. Halperin, A.; Tirrell, M.; Lodge, T. P. Tethered Chains in Polymer Microstructures. *Adv. Polym. Sci.* **1992**, *100*, 31-71.
11. Szleifer, I.; Carignano, M. A. Tethered Polymer Layers. *Adv. Chem. Phys.* **1996**, *94*, 165-260.
12. Uyama, Y.; Kato, K.; Ikada, Y. Surface Modification of Polymers by Grafting. *J. Polym. Sci., Part A: Polym. Chem.* **1998**, *137*, 1-39.
13. Léger, L.; Raphaël, E.; Hervet, H. Surface-Anchored Polymer Chains : Their Role in Adhesion and Friction. *Polymer* **1999**, *138*, 185-225.
14. Zhao, B.; Brittain, W. J. Synthesis, Characterization, and Properties of Tethered Polystyrene-*b*-Polyacrylate Brushes on Flat Silicate Substrate. *Macromolecules* **2000**, *33*, 8813-8820.
15. Currie, E. P. K.; Norde, W.; Cohen Stuart, M. A. Tethered Polymer Chains: Surface Chemistry and their Impact on Colloidal and Surface Properties. *Adv. Colloid Interface Sci.* **2003**, *100-102*, 205-265.
16. Rühle, J.; Ballauff, M.; Biesalski, M.; Dziezok P.; Gröhn, F.; Johannsmann, D.; Houbenov, N.; Hugenberg, N.; Konradi, R.; Minko, S.; Motornov, M.; Netz, R. R.; Schmidt, M.; Seidel, C.; Stamm, M.; Stephan, T.; Usov, D.; Zhang, H. Polyelectrolyte Brushes. *Advanced Computer Simulation Approaches For Soft Matter Sciences I* **2004**, *165*, 79-150.
17. Edmondson, S.; Osborne, V. L.; Huck, W. T. S. Polymer Brushes Via Surface-Initiated Polymerizations. *Chem. Soc. Rev.* **2004**, *33*, 14-22.
18. Tsujii, Y.; Ohno, K.; Yamamoto, S.; Goto, A. Structure and Properties of High-Density Polymer Brushes Prepared by Surface-Initiated Living Radical Polymerization. *Adv. Polym. Sci.* **2006**, *197*, 1-45.
19. Minko, S. Responsive Polymer Brushes. *Polym. Rev.* **2006**, *46*, 397-420.
20. Barbéy, R.; Lavanant, L.; Paripovic, D.; Schüwer, N.; Sugnaux, C.; Tugulu, S.; Klok, H. Polymer Brushes Via Surface-Initiated Controlled Radical Polymerization: Synthesis, Characterization, Properties, and Applications. *Chem. Rev.* **2009**, *109*, 5437-5527.

## **CHAPTER 2**

### **ASPHALTENE ADSORPTION ONTO SELF-ASSEMBLED MONOLAYERS OF MIXED AROMATIC AND ALIPHATIC TRICHLOROSILANES**

#### **2.1. Abstract**

The adsorption of asphaltenes onto flat solid surfaces modified with mixed self-assembled monolayers (SAMs) of aliphatic and aromatic trichlorosilanes with varying wettabilities, aromaticities, and thicknesses is tested. The mixed SAMs are characterized by means of contact angle to assess hydrophobicity and molecular and chemical uniformity, spectroscopic ellipsometry to measure the thickness of the films, and near edge x-ray absorption fine structure (NEXAFS) spectroscopy to assess chemical and molecular composition. The molecular characteristics of the adsorbed asphaltene layer and the extent of asphaltene adsorption are determined using NEXAFS and spectroscopic ellipsometry, respectively. The SAMs are formed by depositing phenyl-, phenethyl-, butyl- and octadecyl- trichlorosilanes from toluene solutions onto silica-coated substrates; the chemical composition and the wettability of the SAM surface is tuned

systematically by varying the trichlorosilane composition in the deposition solutions. The adsorption of asphaltenes on the substrates does not correlate strongly with the SAM chemical composition. Instead, the extent of asphaltene adsorption decreases with increasing SAM thickness. This observation suggests that the leading interaction governing the adsorption of asphaltenes is their interaction with the polar silica substrate and that the chemical composition of the SAM is of secondary importance.

## **2.2. Introduction**

The fouling of pipes and other solid substrates due to the deposition of insoluble organic compounds from petroleum represents a costly problem facing today's oil industry.<sup>1,2</sup> Among these low solubility organics, asphaltenes are known to play a key role in fouling due to their high affinity to various metal and oxide surfaces.<sup>3-9</sup> Asphaltenes constitute chemically- and structurally-heterogeneous organic molecules that possess high degrees of aromaticity and polarity, relatively high molecular weights (ca. 400-2,000 Da), and have a tendency to form supramolecular aggregates in solution. Asphaltenes are a solubility class of molecules defined as the crude oil fraction insoluble in a low boiling paraffinic solvent (n-pentane or n-heptane) but soluble in aromatic solvents, such as toluene or benzene.<sup>10</sup>

The adsorption of asphaltenes onto solid surfaces has been studied using a variety of experimental methods, including, contact angle measurements,<sup>11,12</sup> atomic force microscopy (AFM),<sup>12-14</sup> photothermal surface deformation (PSD),<sup>8,15,16</sup> Fourier transform infrared spectroscopy (FTIR),<sup>14</sup> quartz crystal microbalance gravimetry (QCM),<sup>6,9,17</sup> x-ray photoelectron spectroscopy (XPS),<sup>7</sup> and ellipsometry.<sup>18</sup> To that end, Acevedo et al.<sup>8,15,16</sup> reported on the kinetics of asphaltene adsorption by measuring the optical absorption of dilute asphaltene solutions in contact with silica plates. The authors also used PSD to establish adsorption isotherms on silica plates after 18, 48, and 96 hours of asphaltene adsorption. The authors reported that even at high dilutions asphaltenes adsorbed to silica plates as multilayered deposits. Acevedo and coworkers attributed this multilayered adsorption of asphaltenes to strong asphaltene-asphaltene interactions in solution that resulted in the formation of supramolecular aggregates, which adsorbed onto surfaces. Asphaltenes possess high refractive indices and thus produce opaque solutions even at low concentrations; optical absorption experiments therefore require accurate dilution procedures in order to monitor the adsorption of asphaltenes. In this respect, QCM studies carried out by several groups<sup>6,9,17</sup> are of high importance because QCM, not being affected by the solution transparency, allows for direct adsorption measurement in a wide range of asphaltene solution concentrations.

By utilizing QCM, Ekholm et al.<sup>17</sup> and Dudášová et al.<sup>6</sup> monitored asphaltene adsorption onto a variety of hydrophilic surfaces. Their results revealed that asphaltene adsorption from toluene solution onto hydrophilic surfaces resulted in the adsorption of asphaltene aggregates and the formation of multilayers. The researchers noted that the extent of asphaltene adsorption was governed by the solvent quality, the concentration of asphaltenes in solution, and the chemistry of the asphaltenes, while the exact nature of the hydrophilic surface onto which the asphaltenes are adsorbed played only a minor role. Xie and Karan<sup>9</sup> utilized QCM to monitor the kinetics of asphaltene adsorption onto gold-coated QCM crystals. The authors argued that asphaltenes adsorbed very fast initially, after which they continued adsorbing at a slower rate with no upper limit within the timeframe of the experiments. Labrador et al.<sup>18</sup> employed null ellipsometry to monitor the adsorption of asphaltenes onto glass surfaces after 24 and 48 hours of asphaltene adsorption. The results of Labrador and coworkers supported earlier experimental evidence indicating that strong asphaltene-asphaltene interactions contributed to the formation of thick multilayers on substrates.

While most of the research pertaining to asphaltene adsorption onto solid surfaces has been carried out on hydrophilic metal oxide, metallic, or glass substrates, very little work has been done on chemically modified substrates. Hannisdal et al.<sup>19</sup> studied the stabilizing power of silica particles on water in oil

and oil in water emulsions. While the focus of their study centered on the stability of asphaltenic emulsions, Hannisdal and coworkers provided insight into the adsorption of asphaltenes onto silica particles of varying wettabilities. In their work, commercially available neat silica particles and particles modified with 2-methacryl oxypropyl trimethoxysilane, polydimethyl siloxane, and dimethyl dichlorosilane were exposed to asphaltene solutions. The authors determined visually that hydrophilic particles appeared darker than hydrophobic ones, indicating that they adsorbed a higher amount of asphaltenes. This observation was further verified with near-infrared spectroscopy by monitoring the intensity of the stretching vibration of methylene groups ( $2924\text{ cm}^{-1}$ ), which provides a relative measure of the hydrocarbon content present on the silica surface. These results confirmed that the amount of asphaltenes adsorbed decreased with increasing hydrophobicity of the particles. In spite of offering important insight into the effect of the hydrophobicity of the substrate on asphaltene adsorption, Hannisdal *et al.*'s studies were limited to only a few discrete surfaces. In order to establish the role of hydrophobicity on asphaltene adsorption, one needs to vary methodically the surface energy of the substrate. In this work, we alter systematically the surface energy of the substrate by depositing self-assembled monolayers (SAMs) with gradually varying chemical

composition and study the effect of the substrate surface energy on asphaltene adsorption.

SAMs represent an important tool for engineering surfaces through the modification of their physico-chemical properties.<sup>20</sup> Since their introduction in the 1980's by Sagiv and co-workers,<sup>21-24</sup> organosilanes on silica have been among the most widely used methods for production of well-organized SAMs. Trichlorosilane-based SAMs exhibit great chemical and physical stability due to the reaction of the silane head-group with the silica substrate and subsequent cross-linking among the SAM-forming molecules, leading to the formation of a covalently bound polysiloxane network.<sup>21,25,26</sup> This network endows organosilane-based SAMs with much higher stability relative to other SAMs, *e.g.*, those formed by assembling thiol-based moieties on noble metal surfaces. Smith et al. studied the formation of SAMs by competitive adsorption of aromatic and aliphatic trichlorosilanes from the liquid phase.<sup>27</sup> Using near-edge x-ray absorption fine structure (NEXAFS) spectroscopy and contact angle measurements, Smith and coworkers demonstrated that mixed SAMs with tuned composition can be reproducibly formed by such a deposition method. By varying the ratio of the aromatic to the aliphatic components in the deposition organosilane solutions, the authors engineered SAMs with fine-tuned wettabilities and aromaticities.

In this work, we report on asphaltene adsorption on mixed SAMs. By tailoring the degree of aromaticity and wettability of the SAMs, we hoped to investigate systematically the substrate propensity towards the adsorption of asphaltenes, which are known to contain aromatic cores and aliphatic chains. Specifically, by varying the content of the phenyl- or alkyl- based organosilanes and their packing densities in the SAMs we intended to tune systematically the affinity of the asphaltene molecules to the solid substrate. The structural and physical properties of the SAMs will be characterized with contact angle, spectroscopic ellipsometry, and NEXAFS measurements. The properties of the adsorbed asphaltenes and the extent of adsorption will be characterized with NEXAFS spectroscopy and spectroscopic ellipsometry, respectively. As will be documented later in this paper, the wettability of the substrate does not seem to be the primary factor governing the adsorption of asphaltenes to such mixed SAMs. Instead, we will demonstrate that the thickness of the SAM coating appears to be the leading parameter that regulates the amount of asphaltene adsorption. This leads to the conclusion that the SAM coating acts primarily as a buffer layer regulating the strength of the interaction between asphaltene molecules and the underlying polar silica substrate.

## 2.3. Materials and Methods

### 2.3.1. Materials

n-butyltrichlorosilane (BTS), n-octadecyltrichlorosilane (ODTS), n-phenyltrichlorosilane (PTS) and n-phenethyltrichlorosilane (PETS) were purchased from Gelest, Inc. (Morrisville, PA). HPLC-grade n-heptane and toluene were purchased from Fisher Scientific (Pittsburgh, PA). Absolute ethanol was purchased from Acros Organics (Belgium). All chemicals were used as received. Silicon wafers with [100] orientation were acquired from Silicon Valley Microelectronics (Santa Clara, CA).

Hondo (HOW) crude oil for isolating asphaltenes was obtained from ExxonMobil Upstream Research Company. The lot of Hondo crude used in this study had 14.8% (w/w) asphaltene; the hydrogen to carbon ratio was 1.29. The asphaltene precipitation was described elsewhere.<sup>28</sup> In brief, asphaltenes were obtained by mixing n-heptane and crude oil in a 40:1 volume ratio followed by stirring for 24 hours. The precipitated asphaltenes were removed by vacuum filtration through a 15 cm-diameter Whatman 934-AH glass microfiber filter paper and were sequentially Soxhlet-extracted for 24 hours with n-heptane, to remove residual resins and maltenes, and toluene to re-dissolve the asphaltenes and separate them from carbenes, carboids, and inorganic materials. Toluene

was evaporated and the asphaltenes re-dissolved in methylene chloride for transferring. The asphaltenes were finally dried under reduced pressure resulting in a shiny, dark solid.

### *2.3.2. Sample preparation*

Silicon wafers were cut into 1 x 1 cm<sup>2</sup> pieces, cleaned by rinsing with absolute ethanol and exposed to an ultraviolet/ozone (UVO) treatment for 15 minutes. The latter process generates a high density of surface-bound -OH groups needed for attachment of organosilane SAMs. The cleaned substrates were immediately transferred to a nitrogen-purged glove bag for submersing in deposition solutions.

Stock solutions (2% w/w) of organosilanes were prepared by dissolving the respective trichlorosilanes into HPLC-grade toluene in a nitrogen purged glove bag. These stock solutions were diluted to a final concentration of 2 mmol trichlorosilane per kilogram of solution. Mixed silane solutions were prepared by combining the pure component deposition solutions on a mass basis, for a final trichlorosilane concentration of 2 mmol/kg. The deposition solutions prepared in this manner were used within a day of the time of preparation and only exposed to the atmosphere for the removal of the silicon substrate after deposition. In preliminary experiments, we established that asphaltene

adsorption varied monotonically with varying the fraction of the aromatic component in the SAM for all combinations of the SAM-forming moieties. In the present work we thus concentrate only on exploring systematically the low ( $< 0.2$ ) and high ( $> 0.8$ ) aromatic fraction regimes. Mixed SAMs were formed for mixtures of PTS/BTS, PTS/ODTS, PETS/BTS, and PETS/ODTS. Organosilane SAMs were prepared by submersing UVO-treated silicon substrates into deposition solutions of trichlorosilanes in tightly-sealed containers for approximately 16 hours. After SAM formation, the substrates were removed from the deposition solutions and quickly rinsed with toluene and absolute ethanol, followed by drying with nitrogen gas. Replicates of each sample were made in order to 1) establish the properties of the pre- and post- asphaltene treated SAMs, and 2) ensure the reproducibility of the adsorption experiments.

Asphaltene solutions (0.5% w/w) were prepared by dissolving the precipitated, dry asphaltenes in HPLC grade toluene followed by overnight shaking. Asphaltene adsorption was accomplished by exposing the SAM-covered substrates to these solutions for approximately 12 hours. The samples were then rinsed and sonicated in pure toluene for 5 minutes in order to remove any weakly-adsorbed asphaltenic aggregates or precipitated particles. This step was necessary because the substrate surfaces emerged from the toluene solutions with visible particles and stains. This observation is consistent with the

aforementioned studies that showed that asphaltenes can adsorb indefinitely to a solid surface in the form of multilayers. Because of the sonication, the asphaltene layers studied here are relatively thin and involve only irreversibly adsorbed asphaltenic moieties. After sonication, the samples were thoroughly rinsed with toluene and dried with nitrogen gas.

### 2.3.3. *Contact angle measurements*

Contact angles ( $\theta$ ) with deionized (DI) water as the probing liquid were measured with a Ramé-Hart contact angle goniometer (model 100-00). Static contact angles were determined after releasing an 8  $\mu$ L droplet of deionized water on the surface. To measure the advancing and receding contact angles (A-CA and R-CA, respectively), we captured the probing droplet and added (advancing) or removed (receding) 4  $\mu$ L of DI water. This procedure was repeated for two different spots on each sample and the results were averaged. In our analysis, we assumed that A-CAs provide an estimate of the wettability (*i.e.*, surface energy) of the SAMs. A densely-packed SAM of aliphatic chains should form very hydrophobic surfaces, which exhibit high DI water CAs ( $\theta \approx 110^\circ$ ). In addition, the contact angle hysteresis (CAH), defined here as the difference between A-CA and R-CA, provides information about the chemical and

structural heterogeneities of the SAM. CAH of  $\leq 10^\circ$  is generally considered a signature of a molecularly-uniform surface.<sup>20</sup>

#### 2.3.4. *Spectroscopic ellipsometry*

Film thickness was determined with a variable angle spectroscopic ellipsometer (VASE) (J.A. Woollam Co.). Ellipsometry measures the difference in the polarization state between the light beams incident and reflected from the surface; it provides information about the thickness and dielectric properties of the film. Unless otherwise specified, ellipsometric data were collected at an incidence angle of  $75^\circ$  and at wavelengths ranging from 400 to 1100 nm in 10 nm increments.

The ellipsometric angles  $\Psi$  and  $\Delta$  depend on the thickness and dielectric constant of the probed film. While in most cases one can determine the optical constants and thickness from the ellipsometric data, for very thin films, these parameters are highly correlated and cannot be determined simultaneously.<sup>29,30</sup> In order to estimate the thickness of the SAMs, we assumed the value of the index of refraction ( $n=1.47$ ) and kept it constant through the fitting procedure.<sup>20,31</sup> We note that varying the refractive index of the film by  $\pm 0.05$  results in an uncertainty of approximately  $\pm 1 \text{ \AA}$ .<sup>32</sup> Even though we cannot determine with complete certainty the exact thickness of the film, the estimated

thickness is important for comparison between samples and previously published results.

### *2.3.5. Near-edge x-ray absorption fine structure (NEXAFS) spectroscopy*

NEXAFS data were collected at the NIST/Dow Materials Characterization Facility (beamline U7A) of the National Synchrotron Light Source at Brookhaven National Laboratory (Upton, NY). NEXAFS involves the excitation of core shell electrons by a monochromatic beam of soft x-rays and their subsequent relaxation involving the emission of Auger electrons and fluorescence radiation. The x-ray absorption of thin organic films is preferentially monitored with a partial electron yield (PEY) detector because Auger electron emission represents the dominant relaxation mode for low atomic number atoms, such as carbon.<sup>33</sup> The PEY detector operates at a bias of -150 V in order to detect only electrons that have suffered negligible energy losses, thus enhancing the surface sensitivity of NEXAFS to the uppermost 1-2 nm of the sample.<sup>33,34</sup> NEXAFS derives its elemental specificity from the ability to tune the energy of the incoming synchrotron x-ray beam to match the excitation energy of the core shell electrons of the element of interest ( $\approx 285$  eV for carbon,  $\approx 400$  eV for nitrogen,  $\approx 535$  eV for oxygen). NEXAFS is also sensitive to the chemical environment of the molecules due to the resonance of specific electronic

transitions from the core shell levels to unoccupied anti-bonding orbitals. All experiments were conducted at the so-called “magic angle”, *i.e.*, angle between the sample normal and the electric vector of the x-ray beam equal to 50 degrees, where the PEY intensities are independent of the molecular orientation.<sup>33</sup> **Figure 2.1** shows typical carbon K-edge NEXAFS spectra for the pure component SAMs. By monitoring the relative intensity of the peaks present in the NEXAFS spectrum one can estimate the population of individual bonds in the SAM. In this work we use the area and position of the peak that corresponds to the  $1s \rightarrow \pi_{C=C}^*$  transition ( $\approx 285.1$  eV) of the NEXAFS spectrum to monitor the aromatic fraction in the films. The edge jump of the NEXAFS spectra is defined as the NEXAFS intensity at the post-edge region (arbitrarily chosen at 320 eV) relative to the intensity at the pre-edge region (arbitrarily chosen at 280 eV). The edge jump provides a relative measure of the total amount of carbon present in the specimen. The carbon K-edge spectra are normalized by shifting the pre-edge intensity value to zero and scaling the edge-jump to unity. To obtain the  $1s \rightarrow \pi_{C=C}^*$  peak areas and the peak position we fit the peak of the normalized spectra with a Gaussian lineshape.<sup>33</sup> The area of the  $1s \rightarrow \pi_{C=C}^*$  normalized peak is taken to be a measure of the amount of aromatic material relative to the total carbon content of the film. The apparent position of the  $1s \rightarrow \pi_{C=C}^*$  peak varies depending on the aromatic molecule being probed (**Figure 2.1** inset). Possible

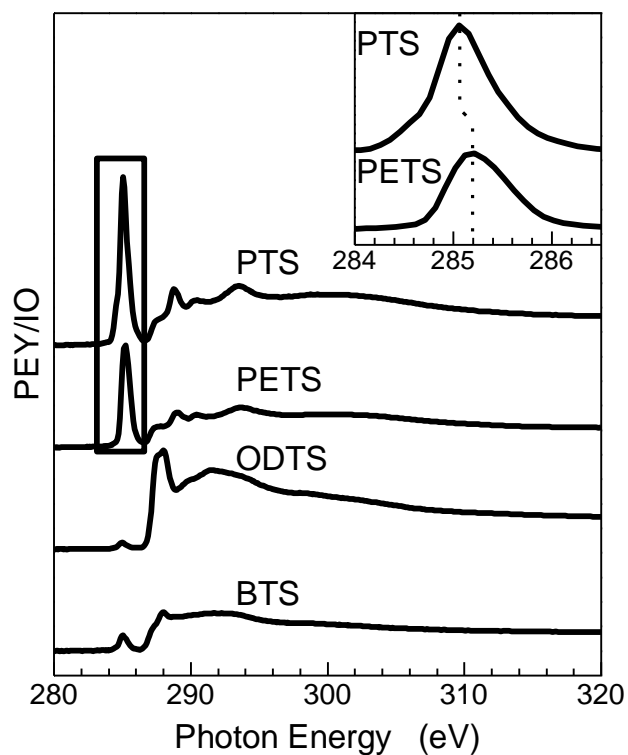


**Figure 2.1.** PEY NEXAFS spectra collected at the carbon K-edge at the “magic” angle of incidence ( $\theta = 50^\circ$ , where  $\theta$  is the angle between the sample normal and the electric vector of the x-ray beam) for the pure component trichlorosilane SAMs. The inset depicts a shift of  $\approx 0.15$  eV between the  $1s \rightarrow \pi_{C=C}^*$  peak positions in the NEXAFS spectra of the PTS and PETS SAMs.

origins of these peak shifts are discussed later in the text. **Figure 2.2** shows spectra for mixed SAMs (left), asphaltene-treated mixed SAMs (middle), and the difference between these two spectra (right). As will be discussed later in the paper, the changes in the spectral features between these data can be attributed to the variation in the chemical composition of the deposited film, its carbon density, and the total amount of carbon being probed.

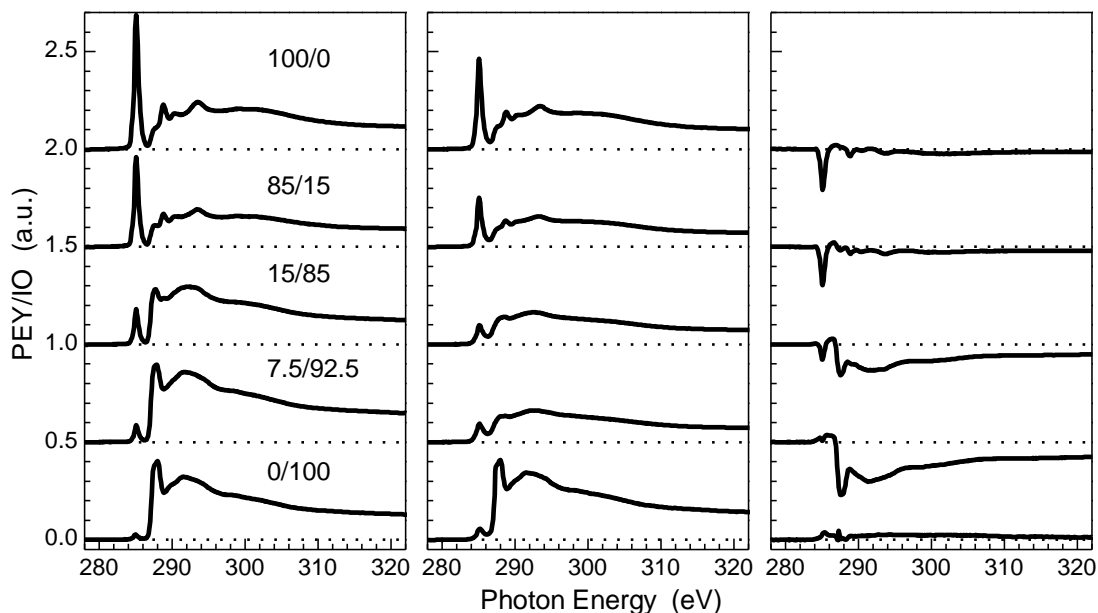


**Figure 2.2.** NEXAFS spectra collected at the carbon K-edge for mixed SAMs (left), asphaltene-treated mixed SAMs (center), and the difference between these two spectra (right). The sample compositions (percentage PTS/percentage ODTS) in the PTS/ODTS SAM correspond (from top to bottom) to 100/0, 85/15, 15/85, 7.5/92.5, and 0/100.

## 2.4. Results and Discussion

The advancing contact angles and contact angle hysteresis for the four mixed aromatic/aliphatic SAMs are presented in **Figure 2.3**. The mixed SAMs exhibit a gradual decrease in the advancing contact angles with increasing aromatic fraction in the deposition SAM solution, indicating that solutions of mixed trichlorosilanes form intermixed SAMs as previously described.<sup>27</sup> ODTS-rich SAMs exhibit the largest A-CA ( $\approx 110^\circ$ ), revealing that these SAMs are densely packed and expose a close-packed array of methyl terminal groups to

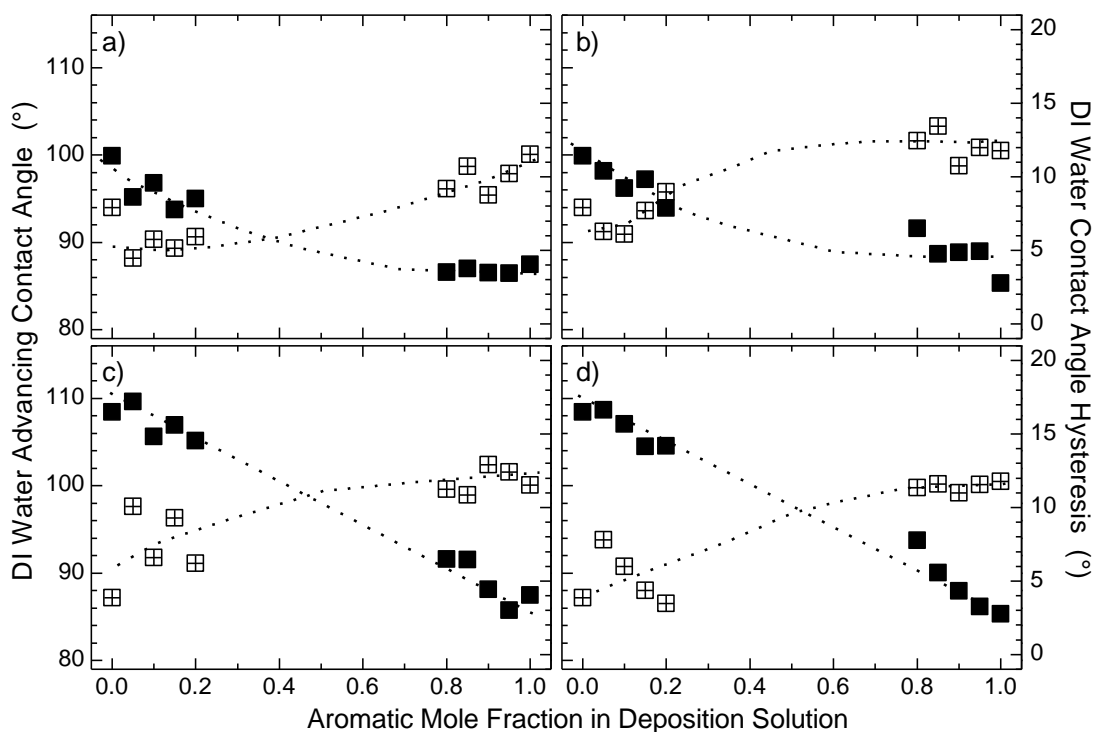


**Figure 2.3.** Advancing contact angle (■, left ordinate) and contact angle hysteresis (⊠, right ordinate) as a function of aromatic fraction in deposition solution for: a) PTS:BTS, b) PETS:BTS, c) PTS:ODTS, and d) PETS:ODTS. The error bars are smaller than the sizes of the symbols. The lines are meant to guide the eye.

the water droplet. The BTS-rich films exhibit a lower A-CA compared to ODTS-rich SAMs. This observation, consistent with previous results,<sup>31</sup> indicates that these films are less densely packed exposing a substantial fraction of methylene groups to the probing water droplet. Additionally, BTS-rich SAMs exhibit a number of structural defects, which might expose the underlying silica substrate to the probing water droplet, effectively decreasing the A-CA. The SAMs rich in either of the two aromatic molecules (PTS and PETS) exhibit lower A-CA than

the aliphatic-rich SAM. The decrease in CA is a consequence of the SAM exposing phenyl rings, which are more polar than the methyl end-groups, to the DI water droplet. The phenyl moieties also pack less densely than ODTS chains, exposing the underlying substrate to the probing liquid and increasing the number of defects in the SAM.

The CAH data plotted in **Figure 2.3** (open symbols) can be divided in two groups, depending on the aromaticity of the probed film. SAMs rich in the aliphatic component exhibit a lower CAH than SAMs rich in the aromatic component, revealing that the aromatic SAMs possess a lower packing density and a higher number of defects relative to their aliphatic counterparts. The CAH is indicative of either the chemical or structural heterogeneity of the SAMs. It is thus noteworthy that the CAH does not change markedly (within error) when probing a mixed SAM instead of a pure SAM, suggesting that pure and mixed SAMs exhibit comparable density of chemical and structural heterogeneities.

The ellipsometric thickness of the mixed SAMs as a function of the aromatic fraction in the deposition solution for the four mixed SAM systems under investigation is plotted in **Figure 2.4**. The thickness of the BTS-based SAMs increases and that of the ODTS-based SAMs decreases with increasing of the aromatic fraction in the deposition solution. This observation provides additional evidence that the composition of the SAMs is comparable to that in

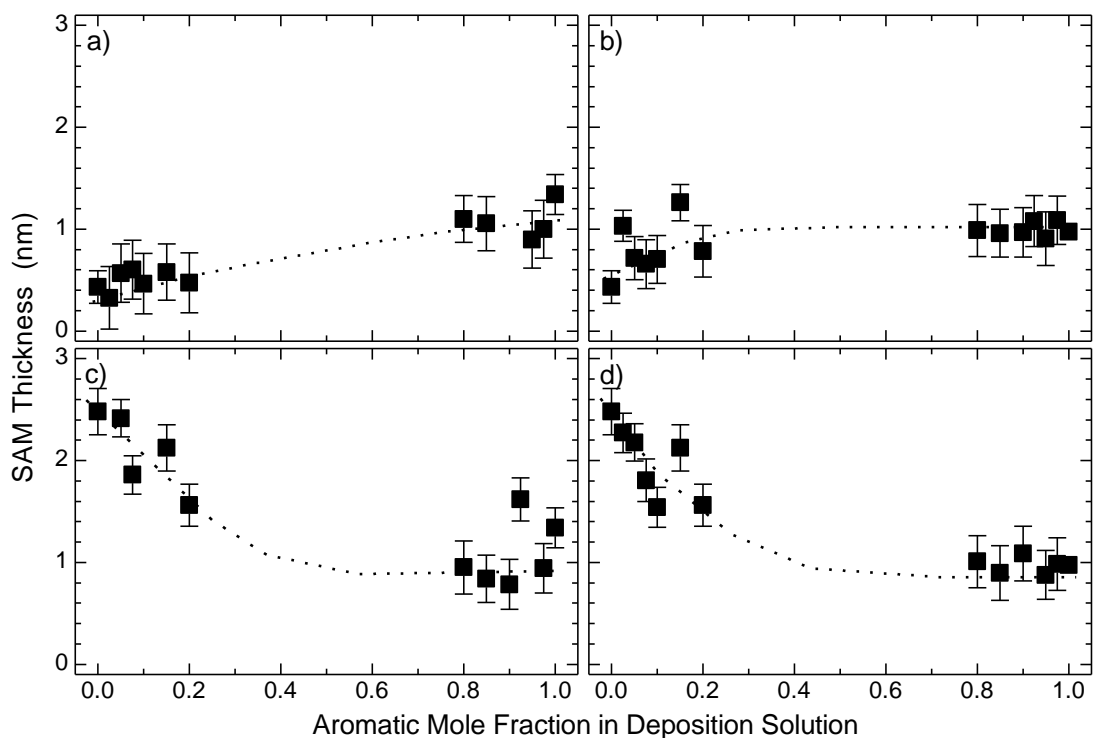


**Figure 2.4.** SAM thickness as a function of aromatic mole fraction in the deposition solution for a) PTS:BTS, b) PETS:BTS, c) PTS:ODTS, and d) PETS:ODTS (d). The lines are meant to guide the eye.

the deposition solution. BTS SAMs are the shortest molecules used; they do not form densely-packed SAMs, as suggested by the contact angle data. The PTS-rich and PETS-rich SAMs exhibit comparable thicknesses even though the PETS has two additional methylene spacers between the phenyl group and the silicon atom. This observation is consistent with previous results, which revealed that PTS SAMs form dense films with the phenyl ring oriented perpendicular to the surface while PETS SAMs exist as lower density films with a slightly higher tilt relative to the surface normal.<sup>27</sup> ODTS-rich SAMs exhibit ellipsometric

thicknesses consistent with those reported in the literature, indicating that the ODTS chains are in an all-trans configuration and aligned nearly parallel to the surface normal, as confirmed with NEXAFS measurements (not shown here).

The chemical composition and carbon density of the SAMs were characterized using NEXAFS. The relative aromatic carbon content in the SAMs can be established by monitoring the area under the  $1s \rightarrow \pi_{C=C}^*$  peak in the NEXAFS spectra. In **Figure 2.1**, we plot the NEXAFS spectra for the four types of pure component SAMs. The PTS and PETS spectra feature a pronounced  $1s \rightarrow \pi_{C=C}^*$  peak, which represents a surface with high aromatic content. BTS and ODTS SAMs differ in that they exhibit very small, albeit still present,  $1s \rightarrow \pi_{C=C}^*$  peaks. Possible sources for the appearance of these peaks in the BTS and ODTS SAM NEXAFS spectra may include the presence of adventitious carbon, beam damage on the sample, and impurities present in the chemicals used for SAM syntheses. **Figure 2.2** shows NEXAFS spectra for mixed SAMs formed from deposition solutions of varying aromatic content (left). The area of the  $1s \rightarrow \pi_{C=C}^*$  peak increases with increasing the content of the aromatic component in the deposition solution, indicating that the composition of the SAM mimics very closely that of the deposition solution. The NEXAFS spectra can be utilized to determine the aromatic content of the SAMs relative to the total amount of carbon in the film. This can be assessed quantitatively by plotting the normalized

$1s \rightarrow \pi_{C=C}^*$  peak area versus the aromatic fraction in deposition solution for all mixed SAMs systems tested (*cf.* **Figure 2.5**, closed symbols). SAMs made from deposition solution containing no aromatic trichlorosilanes exhibit a small, but non-zero,  $1s \rightarrow \pi_{C=C}^*$  normalized peak area. We attribute this spectral feature to the presence of adventitious carbon on the surface. Even though the SAMs are made immediately prior to each experiment, the specimens are taken from the deposition solution, dried, and exposed to the atmosphere before measurement in the synchrotron. Adventitious carbon can therefore adsorb on the surface of the samples explaining the small  $1s \rightarrow \pi_{C=C}^*$  signal in purely aliphatic SAMs. Much care has been taken in this study to minimize the adsorption of atmospheric carbon impurities prior to the NEXAFS experiments.

The compositions of aliphatic-rich SAMs are very sensitive to changes in the aromatic fraction of the deposition solution, with increases as small as 2.5% yielding detectable increases in the  $1s \rightarrow \pi_{C=C}^*$  peak area. For aliphatic SAMs, the variations in the peak area are linear with respect to the composition in SAM solution indicating that the aliphatic and aromatic molecules adsorb competitively on the surface. Additionally, the aliphatic BTS-rich SAMs exhibit in general a higher normalized  $1s \rightarrow \pi_{C=C}^*$  peak area than the corresponding ODTS-rich SAMs, due to several likely reasons. First, BTS molecules have a lower packing density than ODTS, which leads to a decrease in the number of aliphatic

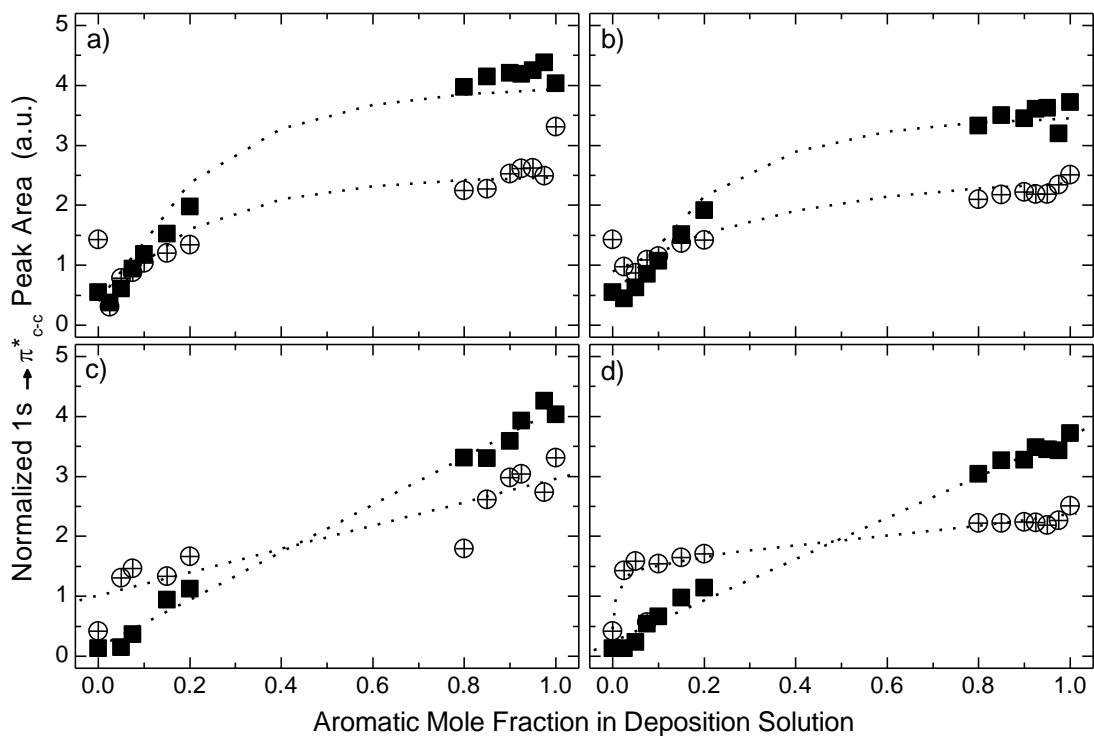


**Figure 2.5.** Normalized  $1s \rightarrow \pi_{C=C}^*$  peak area in the carbon K-edge NEXAFS spectra as a function of aromatic mole fraction in the deposition solution for bare SAMs (■) and HOW asphaltene-treated SAMs (⊕) for a) PTS:BTS, b) PETS:BTS, c) PTS:ODTS, and d) PETS:ODTS. The lines are meant to guide the eye.

molecules per unit area and therefore to a higher amount of aromatic content on the surface. Second, BTS molecules have less carbon atoms per molecule, which results in further increases in the aromatic fraction of the surface. Finally, BTS SAMs are more likely to be contaminated by adventitious carbon because they have a higher surface energy as shown by the contact angle measurements (*cf.* **Figure 2.3**).

The surfaces rich in the aromatic component and BTS are not as sensitive as their aliphatic counterparts are to changes in the composition of the deposition solution. For SAMs in which BTS is the minority component, the  $1s \rightarrow \pi_{C=C}^*$  peak area exhibits little variation with respect to the composition of the deposition solution. This observation implies that for solutions rich in the aromatic component, the aromatic component is faster to populate the surface and that the aromatic content of the SAM is higher than that of the deposition solution. Alternatively, when ODTS is used as the minority component, the compositions of the SAMs retain their sensitivity to changes in the aromatic composition of the deposition solutions, indicating that ODTS SAMs adsorb competitively with the aromatic components and that the composition of the surface resembles closely the composition of the solution. Finally, we note that PTS-based SAMs exhibit, in general, higher  $1s \rightarrow \pi_{C=C}^*$  peak areas when compared to the corresponding PETS based SAMs. This supports previous results indicating that PTS forms denser SAMs than PETS.<sup>27</sup>

Subtle changes in the position of any peak in the NEXAFS spectrum relative to the ionization potential (IP) have been associated with the chemical identity of the bonds involved in the NEXAFS resonance and with variations in the bond length.<sup>33,35,36</sup> The aromatic molecules under investigation here exhibit strong  $1s \rightarrow \pi_{C=C}^*$  resonances present at photon energies lower than the IP threshold;

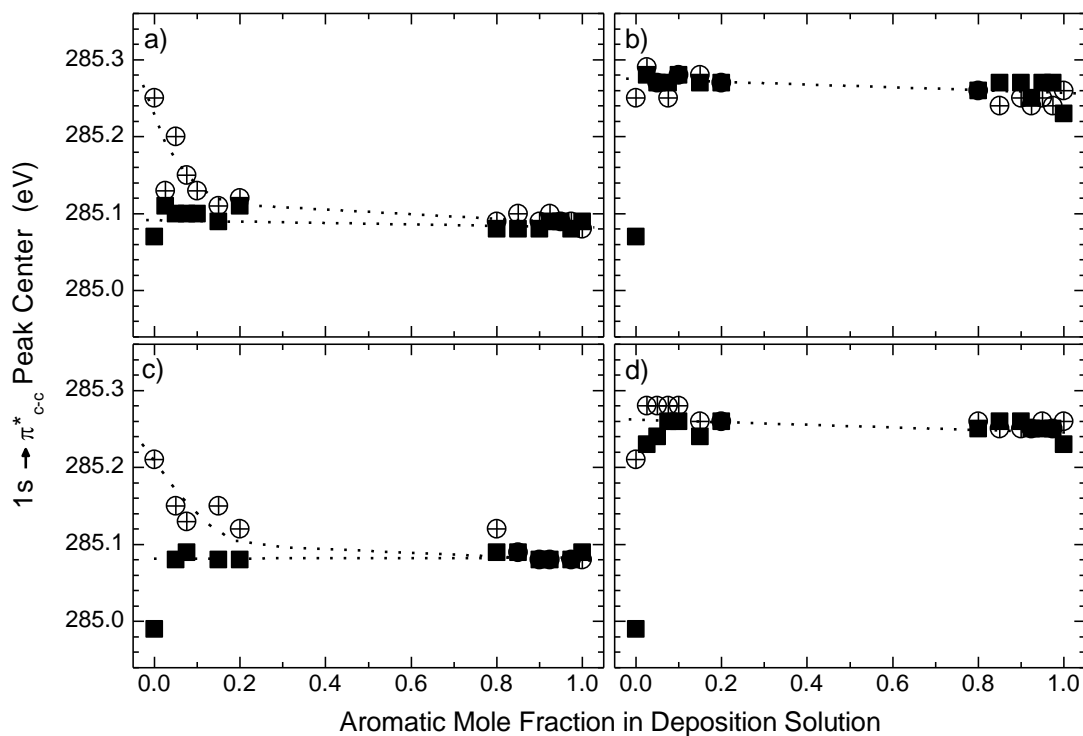


**Figure 2.6.** The  $1s \rightarrow \pi_{C=C}^*$  peak position in the carbon K-edge NEXAFS spectra as a function of aromatic mole fraction in the deposition solution for bare SAMs (■) and HOW asphaltene-treated SAMs (⊕) for a) PTS:BTS, b) PETS:BTS, c) PTS:ODTS, and d) PETS:ODTS. The lines are meant to guide the eye.

this facilitates the precise determination of the peak position. **Figure 2.6** depicts the  $1s \rightarrow \pi_{C=C}^*$  peak position as a function of the aromatic fraction of the mixed SAM. We detect a consistent shift in the  $1s \rightarrow \pi_{C=C}^*$  peak position that depends sensitively on the aromatic molecule incorporated in the film. For PTS-based mixed SAMs an average of  $(285.09 \pm 0.01)$  eV is calculated for the center of the  $1s \rightarrow \pi_{C=C}^*$  peak resonance whereas for PETS SAMs the value is  $(285.26 \pm 0.01)$  eV

(*cf.* the inset in **Figure 2.1**). Furthermore, the  $1s \rightarrow \pi_{C=C}^*$  peak center does not vary as a function of aromatic fraction, with the exception of the purely aliphatic samples, suggesting that the  $1s \rightarrow \pi_{C=C}^*$  peak position is independent of the concentration of the aromatic moiety on the surface. In the case of a purely-aliphatic SAM, the  $1s \rightarrow \pi_{C=C}^*$  resonance peak can be attributed to impurities, adventitious carbon in the film or material produced by beam damage to the sample, and not to an aromatic moiety purposely included in the system. The shift in energy for the aromatic molecules suggests that there is a difference in electronic structure between their carbon-carbon bonds. This may be due to the methylene groups that separate the phenyl ring from the silicon atom in PETS and the differences in the electronic structures of carbon and silicon atoms. Work is currently underway that aims at understanding the nature of the shifts in the  $1s \rightarrow \pi_{C=C}^*$  resonance; details will be provided in our future publication.<sup>37</sup>

The adsorption of asphaltenes on the mixed SAMs is reflected by changes in the positions and intensities of the various NEXAFS peaks and the magnitude of the edge-jump in the NEXAFS spectra. For example, provided that the thickness of the probed film does not surpass the probing depth of PEY NEXAFS (1-2 nm), the adsorption of aromatic material on top of the SAMs should be reflected as an increase in the area of the  $1s \rightarrow \pi_{C=C}^*$  peak and an increase in the edge-jump signal. **Figure 2.2** depicts the spectra for mixed SAMs before (left) and after

(center) treating with asphaltene solutions and their difference (right). The ODTs spectrum in **Figure 2.2** exhibits very little variation upon asphaltene adsorption as reflected by the negligible signal seen in the difference spectra, suggesting that very little adsorption of asphaltenes occurred onto the ODTs SAMs. For the more aromatic SAMs (PTS concentration > 15%) the  $1s \rightarrow \pi_{C=C}^*$  peak area decreases as a result of the asphaltene adsorption, as evidenced by the presence of pronounced negative peaks in the difference spectra. This indicates that a lower amount of aromatic material is probed after the adsorption of asphaltenes. In addition to changes in peak intensities, the data in **Figure 2.2** reveal that the spectral edge-jump decreases upon asphaltene adsorption, suggesting a decrease in the amount of carbon probed. This can be explained by 1) considering that asphaltenes possess lower atomic density than the SAMs and 2) the inability of PEY NEXAFS to probe the entire SAM/asphaltene film. The claim that asphaltenes have a lower atomic density relative to a well-packed SAM is supported by neutron scattering data, which reveal that asphaltenic aggregates can incorporate a significant amount of entrained solvent (30-50% v/v).<sup>38,39</sup> When they are adsorbed to SAMs from solution, dried under nitrogen and subsequently exposed to the ultrahigh vacuum of the NEXAFS experiment, the asphaltenic aggregates likely lose a considerable amount of solvent. Because of the presence of rigid fused aromatic ring complexes, the asphaltenes do not

likely collapse upon solvent removal. Instead, they retain a substantial amount of voids, which leads to reducing their atomic density per unit volume. Thus if only the topmost 1-2 nm of the film are probed by PEY NEXAFS and the asphaltene layer has lower atomic density than the SAM, the edge-jump of the NEXAFS spectra would decrease despite the net increase of carbonaceous material on the surface.

In order to understand the effect of the aromaticity of the SAM on asphaltene adsorption, in **Figure 2.5** we plot the normalized  $1s \rightarrow \pi_{C=C}^*$  peak area before and after asphaltene adsorption as a function of aromatic fraction in the SAM. For highly aromatic mixed SAMs, the amount of aromatic carbon relative to the total carbon probed decreases. In order to interpret correctly this observation one needs to consider the probing depth of the PEY NEXAFS technique, the aromaticity of the adsorbed asphaltene layer, and the total thickness of the combined SAM/asphaltene film. As mentioned previously, the Auger electrons possess a very small mean-free path ( $<1-2$  nm)<sup>34,40</sup> making PEY NEXAFS a very surface-sensitive technique. Although this is beneficial when studying very thin small molecule layers (up to 1 monolayer), it can give rise to difficulties when interpreting PEY NEXAFS data for thicker films. The asphaltene-treated SAMs are likely to be thicker than the probing depth of PEY NEXAFS making it a difficult to measure the extent of asphaltene adsorption.

Despite these limitations, one can still draw useful insights from the PEY NEXAFS data. The  $1s \rightarrow \pi_{C-C}^*$  signal of predominantly-aromatic SAMs is always attenuated upon asphaltene adsorption. An argument similar to that of the attenuated edge jump can explain this observation, namely, given that asphaltenes typically contain 60% of aromatic components and that PEY NEXAFS cannot probe the entire film, the net result of the asphaltene adsorption is a reduction of the probed aromatic carbon. Additionally, the ratio of the attenuated PEY NEXAFS signal to the original SAM signal for aromatic-rich SAMs is fairly constant (with the exception of the PTS:ODTS system) suggesting that the amount of asphaltenes adsorbed for these films should be similar. This observation is consistent with results obtained from ellipsometric measurements, as discussed below.

To better understand the nature of NEXAFS signals from pure asphaltenes, we spun coated 0.5% (w/w) asphaltene in toluene solutions onto cleaned silicon substrates (c.f. **Appendix A**). Spun-coated asphaltenes on silica show a normalized peak area for the  $1s \rightarrow \pi_{C-C}^*$  signal of  $\approx 2$  on the arbitrary unit scale and a peak center of 285.39 eV. This value for the peak area is slightly lower than the signals found for asphaltene-treated aromatic SAMs in **Figure 2.5**. Assuming that spun-coated asphaltenes have an aromatic content that is similar to that present in asphaltenes passively-adsorbed from solutions, this observation

suggests that the carbon in the SAM buried beneath the adsorbed asphaltenes contributes to the overall NEXAFS signal, although its contribution is highly attenuated. Alternatively, asphaltenes of slightly higher aromaticity may be selectively adsorbing to the aromatic-rich SAMs.

Despite the aforementioned limitations of PEY NEXAFS for the study of thick (> 1 nm) films, one can extract important information from the data. It is prudent to mention that a possible method to overcome these limitations is the use of NEXAFS with fluorescence yield (FY) detection whose probing depth is on the order of hundreds of nanometers. While FY NEXAFS appears to be better suited for studying the structure of films thicker than  $\approx 1$  nm, the FY of low atomic number atoms is significantly lower than the Auger yield.<sup>33</sup> For this reason, FY NEXAFS has lower signal-to-noise ratios when compared to the PEY, and consequently requires longer collection times in order to obtain NEXAFS spectra with good statistics. While we do not employ FY NEXAFS in this study, we utilize it in subsequent work and compare the FY and PEY NEXAFS intensity signal in order to gain more information about the sensitivities of the two detection methods.<sup>37</sup>

The data in **Figure 2.6** reveal the effect of asphaltene treatment on the position of the  $1s \rightarrow \pi_{C=C}^*$  resonance peak (crossed symbols). While the PTS-based SAMs exhibit an increase in the peak position upon asphaltene adsorption

at low aromatic fractions, the PETS-based SAMs maintain a constant peak center as a function of the aromatic fraction in the SAM. The shift in the peak position for PTS-based SAMs is attributed to aromatic chemical bonds found in asphaltenic aggregates that have different chemical environments than the trichlorosilane molecules in the SAMs. For primarily aliphatic SAM, the leading contribution to the aromatic PEY signal is due to the aromatic cores in the asphaltenes and not due to the underlying aliphatic SAM. In the case of a primarily aromatic SAM, the predominant aromatic contribution is due to the richly aromatic SAM and not due to the asphaltene signal, resulting in a decrease in the  $1s \rightarrow \pi_{C=C}^*$  resonance peak center to the bare monolayer value. While the same effect should be present in the PETS-based SAMs, it cannot be discriminated in the NEXAFS spectra because the bare PETS SAMs have a  $1s \rightarrow \pi_{C=C}^*$  peak center similar to those for the adsorbed asphaltenes. Nevertheless, the NEXAFS spectra shown in **Figure 2.6** demonstrate clearly the power of NEXAFS spectroscopy to discriminate among various chemical functionalities in a thin organic coating.

It is interesting to compare the  $1s \rightarrow \pi_{C=C}^*$  peak positions for the asphaltene-treated SAMs to the peak center for the spun-coated asphaltenes. The  $1s \rightarrow \pi_{C=C}^*$  peak center in the spun-coated asphaltenes is positioned at 285.39 eV, a value that is higher than those observed for the asphaltenes that were passively

adsorbed onto the monolayers. The processes by which the asphaltenes are adsorbed in both cases are dissimilar; it is possible that different groups of asphaltenes adsorb on the surface for the two adsorption procedures given the rather chemical heterogeneous nature of asphaltene molecules. The value of 285.39 eV provides a possible explanation for the upturn in peak centers for the aliphatic, asphaltene-treated SAMs.

The ellipsometric data of the asphaltene-treated samples were collected using the same parameters as those described for the bare SAMs. We employ a two-layer model in order to estimate the increase in film thickness due to asphaltene adsorption. The first and second layers resting above the silicon substrate represent the native silica layer and the SAM, respectively. The SAM layer is modeled as described before; its thickness is fixed to the values reported in **Figure 2.4**. The second layer, comprising adsorbed asphaltenes, is modeled by assuming an index of refraction of 1.8, a number obtained from measuring the refractive index of spun-coated asphaltene on silicon substrates. Determining the refractive index of spun-coated asphaltenes from ellipsometry is possible because the thickness of these films is high enough so that the thickness and refractive index of the film are no longer correlated. The value of 1.8 determined with this method is higher than refractive index values estimated routinely for asphaltenes in solution.<sup>41</sup> The difference might be attributed to the difference in

structure of the asphaltenic molecules in the adsorbed layer (relative to solution state) and possible chemical fractionation of the asphaltenes upon adsorption. Experimental studies reported that molecules with fused polyaromatic rings might reach refractive indexes  $\approx 2.2$ .<sup>42</sup> Assuming that typical aliphatic hydrocarbons have refractive indices around 1.43, taking the value of the refractive index for aromatic fused rings to be  $\approx 2.2$ , and considering that the aromatic and aliphatic fractions of asphaltenes are 0.6 and 0.4 respectively; one can estimate the effective refractive index of an asphaltene layer to be  $n_{\text{theo}} > 1.9$ . This value is higher than the value of 1.8 measured experimentally in this work. A possible explanation for  $n_{\text{exp}} (=1.8) < n_{\text{theo}}$  is that the adsorbed asphaltene layer contains voids, which would cause the observed decrease in the refractive index of asphaltene relative to densely packed fused polyaromatic rings. This explanation is consistent with the NEXAFS experiments discussed earlier, and while it still needs to be validated by additional experiments, this approach provides a convenient means of approximating relative changes in the asphaltene thickness from sample to sample.

The thickness of the asphaltene layer as a function of the aromatic mole fraction in deposition solution is plotted in **Figure 2.7** for two separate sets of experiments. The comparison of the two data sets provides insight into the reproducibility of our experiments. Although the trend in the adsorption of

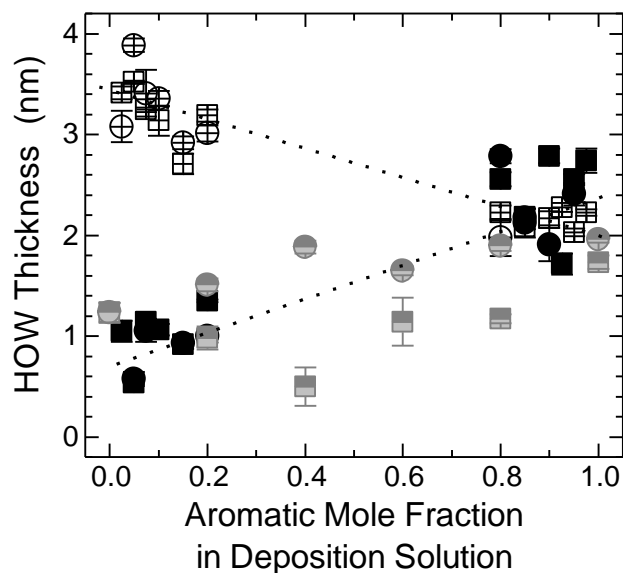


**Figure 2.7.** The thickness of the adsorbed asphaltene film determined by ellipsometry as a function of aromatic fraction in the deposition solution for PTS:BTS ( $\oplus$ ), PTS:BTS ( $\boxplus$ ), PTS:ODTS ( $\bullet$ ) and PTS:ODTS ( $\blacksquare$ ) mixed SAMs. The grey symbols represent repeat experiments for PTS:ODTS (squares) and PTS:ODTS (circles). The lines are meant to guide the eye.

asphaltenes is consistent between the two sets, the absolute values of the adsorbed thickness differ slightly. Among the factors contributing to this lack of absolute reproducibility are: 1) the chemical amphiphilicity and structural heterogeneity of asphaltenes, 2) the overall properties of the SAMs, 3) the sonication procedure, 4) and traces of water that may be present both in the solvent and during the SAM deposition. The SAM quality has a pronounced effect on both the trends and the absolute extent of asphaltene adsorption. In a separate set of experiments (unpublished data), we observed that adsorption of asphaltenes on the SAM monolayer, in cases in which the SAM had lower hydrophobicity, resulted in irreproducible adsorption data. Another factor

possibly contributing to the data scatter is those different sonicating baths were used for the different experimental sets. This lead to different amounts of asphaltenes being removed from the surface depending on the sonication power of the specific instrument.<sup>2</sup> For this reason, data comparisons should be made among data points collected in the same experiment.

The data in **Figure 2.7** reveal two distinct trends between the aromaticity of the SAM and the thickness of the adsorbed asphaltenes. For ODTS-based SAMs, the asphaltene layer thickness increases with increasing aromatic character of the SAM. In contrast, for BTS-based SAMs the thickness decreases with increasing aromatic fraction. Given that ODTS-rich SAMs are thicker than BTS based SAMs, these observations suggest that the extent of asphaltene adsorption depends strongly on the thickness of the SAM as opposed to the aromaticity of the SAM. In **Figure 2.8** we plot the thickness of the asphaltene layer as a function of the SAM thickness. Based on the data in **Figure 2.8** one can conclude that the thickness of the asphaltene layer decreases with increasing SAM thickness. It is possible to divide the data into three distinct groups depending on the majority component of the SAM. BTS-rich SAMs represent the thinnest SAMs; they exhibit the largest amounts of asphaltene adsorption. The BTS-rich SAMs are closely followed by the aromatic-rich SAMs. PTS and PETS SAMs have equivalent thicknesses (*cf.* **Figure 2.4**) resulting in little difference in the extent of

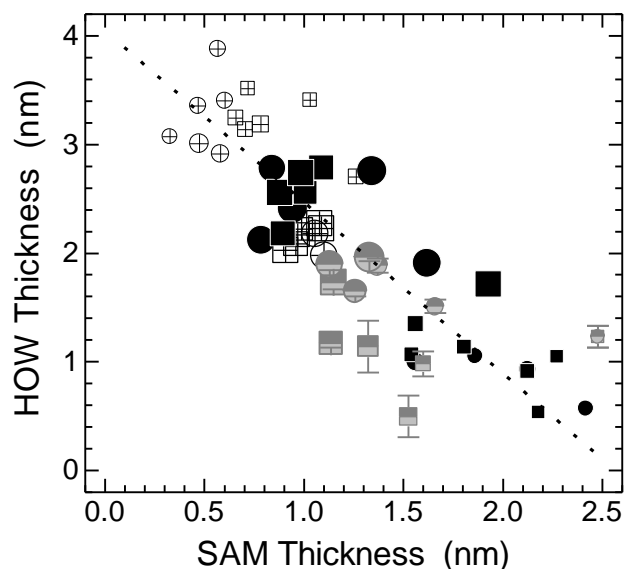


**Figure 2.8.** The asphaltene film thickness plotted as a function of the thickness of the underlying SAM for PTS:BTS ( $\oplus$ ), PETS:BTS ( $\boxplus$ ), PTS:ODTS ( $\bullet$ ) and PETS:ODTS ( $\blacksquare$ ). The marker size represents the degree of aromaticity (increasing marker size corresponds to increasing degree of aromaticity) of a given data point. The size of each symbol increases proportionally with increasing aromaticity of the SAM solution. The grey symbols represent repeat experiments for PTS:ODTS (squares) and PETS:ODTS (circles). The line is meant to guide the eye.

asphaltene adsorption between these films. This observation is consistent with the similar attenuations of the normalized  $1s \rightarrow \pi_{C=C}^*$  peak areas for SAMs rich in the aromatic component after asphaltene deposition (*cf.* **Figure 2.5**). The lowest asphaltene adsorption is detected on ODTS-rich SAMs; the thickest, densest, and most hydrophobic SAMs studied. The fact that the asphaltene thickness depends on the thickness of the SAMs suggests that the leading interaction affecting asphaltene adsorption onto SAMs is the interaction with the underlying  $\text{SiO}_x$  substrate rather than the interaction between asphaltenes and the tail group in the SAM. Even though our original hypothesis was that the asphaltenes would

interact strongly with an aromatic surface, it is not surprising that the strongest interaction is with the high energy silica substrate. Asphaltenes constitute some of the most polar components in crude oil and they therefore can interact strongly with the underlying polar  $\text{SiO}_x$  substrate through the polar moieties present in asphaltenes, viz. pyridinic and pyrrolic nitrogen, phenolic hydroxyl, carboxylic groups, and quinonic oxygen. The aromaticity of the SAMs seems to play a minor role in the adsorption process.

## **2.5. Conclusions**

We have studied the adsorption of asphaltenic aggregates on SAMs of fine-tuned aromatic/aliphatic composition. Our results reveal that good control of the SAM composition can be achieved by carefully varying the ratio of the aromatic to aliphatic organosilanes in the deposition solution. The asphaltene adsorption experiments show that the aromaticity of the SAM is not the leading factor in determining adsorption of asphaltenes. Instead, we observed that the ability of the SAM to shield the polar  $\text{SiO}_x$  substrate is the most significant factor in determining the extent of asphaltene adsorption. We used PEY NEXAFS as a tool to study the adsorption of asphaltenes. We note that PEY has some limitations when dealing with adsorption studies that involve films that are thicker than the inelastic mean free path of Auger electrons. A way to overcome

these limitations is to use fluorescence yield NEXAFS for absolute characterization of the adsorption events and comparison to the ellipsometry data. Experiments employing both PEY and FY NEXAFS signals will be reported in a subsequent publication.<sup>37</sup>

## 2.6. References

1. Leontaritis, K. J.; Ali Mansoori, G. Asphaltene Deposition: A Survey of Field Experiences and Research Approaches. *J. Pet. Sci. Eng.* **1988**, *1*, 229-239.
2. Sheu, E. Y.; Mullins, O. C., Eds.; In *Asphaltenes : fundamentals and applications*; Plenum Press: New York, 1995; , pp 245.
3. Thawer, R.; Nicoll, D. C. A.; Dick, G. Asphaltene Deposition in Production Facilities. *SPE Prod. Eng.* **1990**, *5*, 475-480.
4. Misra, S.; Baruah, S.; Singh, K. Paraffin Problems in Crude-Oil Production and Transportation - a Review. *SPE Prod. Facil* **1995**, *10*, 50-54.
5. Mansoori, G. A. In *In Deposition and Fouling of Heavy Organic Oils and Other Compounds*; Proceedings of the 9th International Conference on Properties and Phase Equilibria for Product and Process Design; 2001; .
6. Dudášová, D.; Silset, A.; Sjöblom, J. Quartz Crystal Microbalance Monitoring of Asphaltene Adsorption/Deposition. *J. Dispersion Sci. Technol.* **2008**, *29*, 139-146.
7. Abdallah, W. A.; Taylor, S. D. Surface Characterization of Adsorbed Asphaltene on a Stainless Steel Surface. *Nucl. Instrum. Methods Phys. Res. , Sect. B* **2007**, *258*, 213-217.
8. Acevedo, S.; Ranaudo, M. A.; Garcia, C.; Castillo, J.; Fernandez, A. Adsorption of Asphaltenes at the Toluene-Silica Interface: A Kinetic Study. *Energy Fuels* **2003**, *17*, 257-261.

9. Xie, K.; Karan, K. Kinetics and Thermodynamics of Asphaltene Adsorption on Metal Surfaces: A Preliminary Study. *Energy Fuels* **2005**, *19*, 1252-1260.
10. Speight, J. G. In *The Chemistry and Technology of Petroleum*; Chemical Industries; Marcel Dekker, Inc.: New York, 1999; Vol. 76, pp 918.
11. Drummond, C.; Israelachvili, J. Fundamental Studies of Crude Oil-Surface Water Interactions and its Relationship to Reservoir Wettability. *J. Pet. Sci. Eng.* **2004**, *45*, 61-81.
12. Toulhoat, H.; Prayer, C.; Rouquet, G. Characterization by Atomic-Force Microscopy of Adsorbed Asphaltenes. *Colloids Surf., A* **1994**, *91*, 267-283.
13. Batina, N.; Manzano-Martinez, J. C.; Andersen, S. I.; Lira-Galeana, C. AFM Characterization of Organic Deposits on Metal Substrates from Mexican Crude Oils. *Energy Fuels* **2003**, *17*, 532-542.
14. Batina, N.; Reyna-Cordova, A.; Trinidad-Reyes, Y.; Quintana-Garcia, M.; Buenrostro-Gonzalez, E.; Lira-Galeana, C.; Andersen, S. I. Qualitative Analysis of Thin Films of Crude Oil Deposits on the Metallic Substrate by Fourier Transform Infrared (FTIR) Microscopy. *Energy Fuels* **2005**, *19*, 2001-2005.
15. Acevedo, S.; Castillo, J.; Fernandez, A.; Goncalves, S.; Ranaudo, M. A. A Study of Multilayer Adsorption of Asphaltenes on Glass Surfaces by Photothermal Surface Deformation. Relation of this Adsorption to Aggregate Formation in Solution. *Energy Fuels* **1998**, *12*, 386-390.
16. Acevedo, S.; Ranaudo, M. A.; Garcia, C.; Castillo, J.; Fernandez, A.; Caetano, M.; Goncalves, S. Importance of Asphaltene Aggregation in Solution in Determining the Adsorption of this Sample on Mineral Surfaces. *Colloids Surf., A* **2000**, *166*, 145-152.
17. Ekholm, P.; Blomberg, E.; Claesson, P.; Auflem, I. H.; Sjöblom, J.; Kornfeldt, A. A Quartz Crystal Microbalance Study of the Adsorption of Asphaltenes and Resins Onto a Hydrophilic Surface. *J. Colloid Interface Sci.* **2002**, *247*, 342-350.
18. Labrador, H.; Fernandez, Y.; Tovar, J.; Munoz, R.; Pereira, J. C. Ellipsometry Study of the Adsorption of Asphaltene Films on a Glass Surface. *Energy Fuels* **2007**, *21*, 1226-1230.

19. Hannisdal, A.; Ese, M.; Hemmingsen, P. V.; Sjöblom, J. Particle-Stabilized Emulsions: Effect of Heavy Crude Oil Components Pre-Adsorbed Onto Stabilizing Solids. *Colloids Surf., A* **2006**, *276*, 45-58.
20. Ulman, A. In *An introduction to ultrathin organic films : from Langmuir-Blodgett to self-assembly*; Academic Press: Boston, 1991; , pp 442.
21. Sagiv, J. Organized Monolayers by Adsorption. 1. Formation and Structure of Oleophobic Mixed Monolayers on Solid-Surfaces. *J. Am. Chem. Soc.* **1980**, *102*, 92-98.
22. Netzer, L.; Sagiv, J. A New Approach to Construction of Artificial Monolayer Assemblies. *J. Am. Chem. Soc.* **1983**, *105*, 674-676.
23. Netzer, L.; Iscovici, R.; Sagiv, J. Adsorbed Monolayers Versus Langmuir-Blodgett Monolayers—Why and how? II: Characterization of Built-Up Films Constructed by Stepwise Adsorption of Individual Monolayers. *Thin Solid Films* **1983**, *100*, 67-76.
24. Maoz, R.; Sagiv, J. On the Formation and Structure of Self-Assembling Monolayers. I. A Comparative ATR-Wettability Study of Langmuir-Blodgett and Adsorbed Films on Flat Substrates and Glass Microbeads. *J. Colloid Interface Sci.* **1984**, *100*, 465-496.
25. Finklea, H. O.; Robinson, L. R.; Blackburn, A.; Richter, B.; Allara, D.; Bright, T. Formation of an Organized Monolayer by Solution Adsorption of Octadecyltrichlorosilane on Gold—Electrochemical Properties and Structural Characterization. *Langmuir* **1986**, *2*, 239-244.
26. Allara, D. L.; Parikh, A. N.; Rondelez, F. Evidence for a Unique Chain Organization in Long-Chain Silane Monolayers Deposited on 2 Widely Different Solid Substrates. *Langmuir* **1995**, *11*, 2357-2360.
27. Smith, M. B.; Efimenko, K.; Fischer, D. A.; Lappi, S. E.; Kilpatrick, P. K.; Genzer, J. Study of the Packing Density and Molecular Orientation of Bimolecular Self-Assembled Monolayers of Aromatic and Aliphatic Organosilanes on Silica. *Langmuir* **2007**, *23*, 673-683.

28. Spiecker, P. M.; Gawrys, K. L.; Kilpatrick, P. K. Aggregation and Solubility Behavior of Asphaltenes and their Subfractions. *J. Colloid Interface Sci.* **2003**, *267*, 178-193.
29. McCrackin, F. L.; Passaglia, E.; Stromberg, R. R.; Steinberg, H. L. Measurement of Thickness and Refractive Index of very Thin Films and Optical Properties of Surfaces by Ellipsometry. *J. Res. Natl. Bur. Stand. Sect. A* **1963**, *A 67*, 363-377.
30. McCrackin, F. L.; Passaglia, E.; Stromberg, R. R.; Steinberg, H. L. Measurement of the Thickness and Refractive Index of very Thin Films and the Optical Properties of Surfaces by Ellipsometry. *J. Res. Nat. Inst. Stand. Technol.* **2001**, *106*, 589-603.
31. Wasserman, S. R.; Tao, Y. T.; Whitesides, G. M. Structure and Reactivity of Alkylsiloxane Monolayers Formed by Reaction of Alkyltrichlorosilanes on Silicon Substrates. *Langmuir* **1989**, *5*, 1074-1087.
32. Tillman, N.; Ulman, A.; Schildkraut, J. S.; Penner, T. L. Incorporation of Phenoxy Groups in Self-Assembled Monolayers of Trichlorosilane Derivatives - Effects on Film Thickness, Wettability, and Molecular-Orientation. *J. Am. Chem. Soc.* **1988**, *110*, 6136-6144.
33. Stöhr, J. In *NEXAFS Spectroscopy*; Springer Series in Surface Sciences 25; Springer-Verlag: New York, 1992; , pp 403.
34. Genzer, J.; Kramer, E. J.; Fischer, D. A. Accounting for Auger Yield Energy Loss for Improved Determination of Molecular Orientation using Soft x-Ray Absorption Spectroscopy. *J. Appl. Phys.* **2002**, *92*, 7070-7079.
35. Sette, F.; Stohr, J.; Hitchcock, A. P. Correlation between Intramolecular Bond Lengths and K-Shell Sigma-Shape Resonances in Gas-Phase Molecules. *Chem. Phys. Lett.* **1984**, *110*, 517-520.
36. Sette, F.; Stohr, J.; Hitchcock, A. P. Determination of Intramolecular Bond Lengths in Gas Phase Molecules from K Shell Shape Resonances. *J. Chem. Phys.* **1984**, *81*, 4906-4914.
37. Turgman-Cohen, S.; Fischer, D. A.; Kilpatrick, P. K.; Genzer, J. Unpublished, 2008.

38. Gawrys, K. L.; Kilpatrick, P. K. Asphaltenic Aggregates are Polydisperse Oblate Cylinders. *J. Colloid Interface Sci.* **2005**, *288*, 325-334.
39. Gawrys, K. L.; Blankenship, G. A.; Kilpatrick, P. K. Solvent Entrainment in and Flocculation of Asphaltenic Aggregates Probed by Small-Angle Neutron Scattering. *Langmuir* **2006**, *22*, 4487-4497.
40. Sohn, K. E.; Dimitriou, M. D.; Genzer, J.; Fischer, D. A.; Hawker, C. J.; Kramer, E. J. Determination of the Electron Escape Depth for NEXAFS Spectroscopy. *Langmuir* **2009**, *25*, 6341--6348.
41. Buckley, J. S.; Hirasaki, G. J.; Liu, Y.; Von Drasek, S.; Wang, J. X.; Gil, B. S. Asphaltene Precipitation and Solvent Properties of Crude Oils. *Petrol. Sci. Technol.* **1998**, *16*, 251-285.
42. McCartney, J. T.; Ergun, S. Refractive Index and Thickness of Ultrathin Sections of Coals and Graphite by Interferometry. *J. Opt. Soc. Am.* **1962**, *52*, 197-200.

## CHAPTER 3

### ASPHALTENE ADSORPTION ONTO SELF-ASSEMBLED MONOLAYERS OF ALKYLTRICHLOROSILANES OF VARYING CHAIN LENGTH

#### 3.1. Abstract

The adsorption of asphaltenes onto flat silica surfaces modified with self-assembled monolayers (SAMs) of alkyltrichlorosilanes of varying thickness due to a variable number of carbon atoms ( $N_C$ ) has been studied by means of contact angle measurements, spectroscopic ellipsometry, and NEXAFS spectroscopy. The extent of asphaltene adsorption was found to depend primarily on the ability of the SAM layer to shield the underlying silicon substrate from interacting with the asphaltenes present in solution. Specifically, asphaltene adsorption decreased with increasing SAM grafting density,  $\sigma_{SAM}$ , (i.e., number of SAM molecules per unit area), or/and  $N_C$ . The effect of solvent quality on the extent of asphaltene adsorption was gauged by adsorbing asphaltenes from toluene, 1-methylnaphthalene, tetralin, decalin, and toluene/heptanes mixtures. The extent

of asphaltene adsorption was found to increase proportionally with decreasing the Hildebrand solubility parameter of the solvent.

### **3.2. Introduction**

Pipeline fouling due to deposition of heavy organics from crude oils represents a significant problem for the petroleum industry because it decreases pipeline flow rates thus seriously hindering oil refining and production.<sup>1</sup> In severe cases, fouling of pipelines requires costly cleaning procedures or even pipeline replacement, often resulting in complete plant shutdown. Asphaltenes, defined broadly as a fraction of crude oil insoluble in a low boiling paraffinic solvent (n-pentane or n-heptane) but soluble in aromatic solvents such as toluene or benzene,<sup>2</sup> are in many cases responsible for this detrimental pipeline contamination. Asphaltenes represent a chemically and structurally heterogeneous group of organic molecules present in oil; they are typically characterized as macromolecules with high aromaticity and polarity, which possess a propensity to form colloidal aggregates in solution, stabilize water in oil emulsions, and have the ability to adsorb onto solid/liquid and liquid/liquid interfaces. Devising ways in which to prevent or substantially lessen the adsorption of asphaltenes onto solid surfaces can therefore be beneficial to the petroleum industry.

Research pertaining to the adsorption of asphaltenes onto solid surfaces has recently experienced upsurge due primarily to soaring petroleum prices and the possibility that refining crudes with high asphaltenic content becomes a viable commercial venture. The adsorption of asphaltenes onto solid substrates has been characterized by means of a wide variety of experimental methods including, contact angle measurements<sup>3-5</sup>, ultraviolet-visible spectrometry (UV-Vis),<sup>6</sup> atomic force microscopy (AFM)<sup>4,7,8</sup>, photothermal surface deformation (PSD)<sup>9-12</sup>, Fourier transform infrared spectroscopy (FTIR)<sup>8</sup>, quartz crystal microbalance gravimetry (QCM)<sup>13-15</sup>, x-ray photoelectron spectroscopy (XPS)<sup>6,16</sup> and ellipsometry.<sup>17,18</sup> The adsorption of asphaltenes onto solid surfaces is governed by the characteristics of the asphaltenic solutions, including asphaltene source and concentration as well as solvent quality. Akhlaq et al.<sup>5</sup> investigated the adsorption of asphaltenes onto glass plates by monitoring the variation in the contact angle of a glycerol droplet on the asphaltene-treated surfaces. The contact angle of glycerol on the glass plates increased after asphaltene treatment suggesting that asphaltenes shielded the polar substrate from the probing liquid. Akhlaq and coworkers also monitored the increase in contact angle for depositions from solvents of varying polarity, that is toluene, tetrahydrofuran, chloroform and n-heptane/toluene (heptol) mixtures. The contact angle of the plates was reported to increase with decreasing solvent

polarity. This observation was attributed to higher amounts of asphaltenes adsorbed on the glass surface, which effectively shielded the substrate from the probing droplet. In a latter work, Alboudwarej et al.<sup>19</sup> characterized the adsorption of asphaltenes onto metals by monitoring the asphaltene concentration in solution using UV-Vis spectrometry. Adsorption experiments from very dilute solutions (<0.06% w/w) onto stainless steel, iron, and aluminum powders indicated monolayer adsorption of asphaltenes, suggesting that the adsorption was limited by the number of adsorption sites on the metallic surface. The same authors observed that the amount of asphaltenes adsorbed on the surfaces decreased in the following fashion: stainless steel > iron > aluminum. However, no plausible explanation was offered in the original publications to explain these observations. Alboudwarej and coworkers also noted that asphaltenes dissolved in heptol mixtures adsorbed to a higher extent relative to adsorption taking place from pure toluene solutions. This observation, consistent with other studies, was reconciled by considering the decrease in solubility of asphaltenes and the formation of larger supramolecular aggregates in heptol solutions relative to toluene.<sup>20-22</sup>

QCM and optical ellipsometry represent two practical tools applicable in characterizing asphaltene adsorption. QCM monitors the mass of adsorbed asphaltenes in-situ from a wide range of solution concentrations.<sup>13</sup> Unlike QCM,

which is not limited by the transparency of the deposition solution, ellipsometry does not permit in-situ measurements. However, ellipsometry can provide information about both the thickness of the adsorbed asphaltenes with sub-nanometer precision and the average optical properties of the adsorbed layer.<sup>23</sup> Ekholm et al.<sup>13</sup> studied the effects of solution concentration and solvent quality on the adsorption of asphaltenes onto a gold surface. The exposure of the QCM crystal to the asphaltene solutions results in rapid shifts in the crystal's oscillating frequency, indicating the adsorption of small supramolecular aggregates. The authors observed that the adsorption of asphaltenes from toluene solutions increased continuously as a function of increasing concentration with no plateau observed at high solute concentrations. This behavior was attributed to strong asphaltene-asphaltene interactions in toluene that resulted in the formation of multilayers on the gold substrate. The adsorption of asphaltenes from heptol mixtures with equimolar compositions was also characterized and a larger extent of asphaltene adsorption was detected relative to equivalent concentrations of asphaltenes in toluene, emphasizing the effect of the solvent quality on the extent of asphaltene adsorption. Labrador et al.<sup>17</sup> employed null ellipsometry to monitor the adsorption of asphaltenes onto glass surfaces after 24 or 48 hours of asphaltene adsorption. Their results supported earlier evidence indicating that strong

asphaltene-asphaltene interactions contributed to the formation of thick multilayers.

While most of the research on asphaltene adsorption onto solid surfaces has been carried out on hydrophilic metallic or glass substrates, the effect of modifying these substrates chemically has not been explored systematically. Hannisdal et al.<sup>24</sup> studied the stabilizing power of silica particles on water in oil and oil in water emulsions. Although the focus of their study pertained to the stability of emulsions as the wettability of the particles varied, the authors provided insights into the adsorption of asphaltenes onto chemically modified silica particles. In their work, commercially available neat silica particles and particles modified with 2-methacryl oxypropyl trimethoxysilane, polydimethyl siloxane, and dimethyl dichlorosilane were treated with asphaltene solutions. The authors established visually that hydrophilic particles appeared darker than hydrophobic ones after treatment, indicating that hydrophilic particles adsorbed a higher amount of asphaltenes. This observation was verified with experiments using near-infrared spectroscopy that monitored the intensity of the stretching vibration of methylene groups ( $2924\text{ cm}^{-1}$ ), which represented a convenient measure of the hydrocarbon content present on the silica surface. These results confirmed that the amount of asphaltenes adsorbed increased with increasing hydrophilicity of the particle surfaces. In a subsequent study, Dudášová and

coworkers used UV-Vis spectrometry to monitor the adsorption of asphaltenes on a variety of inorganic particles, including hydrophilic and hydrophobic SiO<sub>2</sub>.<sup>6</sup> The asphaltene adsorption increased for the hydrophilic SiO<sub>2</sub> particles relative to the hydrophobic ones.

In spite of offering important insight into the effect of the amphiphilicity of the substrate on asphaltene adsorption, these studies were limited to only a few discrete surface types. In order to ascertain firmly the role of hydrophobicity on asphaltene adsorption, one needs to vary the surface energy of the substrate methodically. In previous work,<sup>18</sup> we altered systematically the surface energy of the substrate by depositing self-assembled monolayers (SAMs) with smoothly varying chemical composition,<sup>25</sup> and studied the effect of the substrate wettability, aromaticity, and organic layer thickness on asphaltene adsorption. We concluded that, although the chemistry of the substrates was carefully controlled, wettability of the substrate was not the leading factor controlling the extent of asphaltene adsorption. Instead, we found that the extent of adsorption was controlled by the thickness of the underlying SAM, suggesting that the interaction between asphaltenes and the underlying polar silicon substrate was the most important factor governing the asphaltene adsorption process. In this paper we build upon our previous findings and study asphaltene adsorption on aliphatic SAM surfaces with systematically increasing length of the aliphatic

spacer (or equivalently the number of carbon atoms,  $N_C$ , in the hydrocarbon mesogen). A clear picture of the physical and chemical property changes induced by chemical modification and asphaltene adsorption onto these substrates can potentially aid in the design of robust, asphaltene-repellent coatings for the inner walls of oil pipelines.

The wettability, thickness, and carbon density of the hydrophobic SAMs are characterized by means of contact angle (CA) measurements, variable angle spectroscopic ellipsometry (VASE), and near edge x-ray absorption fine structure (NEXAFS) spectroscopy. The extent of asphaltene adsorption on these SAM surfaces is assessed using NEXAFS and VASE. Our primary aim is to verify that increasing the length of the SAM molecules and keeping the chemical nature of the SAM surfaces unchanged results in a decreased amount of adsorbed asphaltenes on such SAM surfaces. Additionally, we will report on the effect of solvent quality on the thickness of the adsorbed asphaltene layer. We will provide evidence that the extent of asphaltene adsorption increases with decreasing the solubility of the asphaltenes in the solvent. Finally, we will reveal the importance of a thorough, multi-faceted approach to characterizing the SAMs prior to their use in adsorption experiments, as evidenced by the effect of varying SAM properties on the extent of adsorption of asphaltenes on the surface.

### 3.3. Materials and Methods

#### 3.3.1. Materials

n-butyl- (BTS), n-hexyl- (HTS), n-octyl- (OTS), n-decyl- (DTS), n-dodecyl- (DDTS), n-hexadecyl- (HDTS), and n-octadecyl- (ODTS) trichlorosilanes were purchased from Gelest, Inc. (Morrisville, PA) and used as received. HPLC-grade n-heptane and toluene were received from Fisher Scientific, 1,2,3,4 - tetrahydronaphthalene (tetralin) and 1-methylnaphthalene (MN) were obtained from Sigma-Aldrich, absolute ethanol was supplied by Acros Organics. All solvents were used as received. Silicon wafers (orientation [100]) were supplied by Silicon Valley Microelectronics. Hondo (HOW) crude oil for asphaltene precipitation was donated by ExxonMobil Upstream Research Company. Hondo crudes had 14.8% (w/w) asphaltene content with hydrogen to carbon ration of 1.29. The asphaltene precipitation was described elsewhere.<sup>26</sup> Briefly, asphaltenes were obtained by mixing n-heptane and crude oil in a 40:1 weight ratio followed by stirring for 24 hours. The mixture was subsequently filtered and the asphaltenes were sequentially Soxhlet-extracted with n-heptane and toluene for 24 hours each. The toluene was evaporated and the asphaltenes re-dissolved in methylene chloride for transferring. The asphaltenes were finally dried under reduced pressure resulting in a shiny, dark solid.

### 3.3.2. *Sample preparation*

Silicon wafers were cut into small (1 x 2 cm<sup>2</sup>) pieces and cleaned by rinsing with absolute ethanol and exposing to an ultraviolet/ozone (UVO) treatment for 15 minutes. The latter process generated a high density of surface-bound -OH groups needed for SAM attachment. Deposition solutions of organosilanes were prepared inside a glove bag purged with nitrogen. A known amount of alkyltrichlorosilane was dissolved into HPLC-grade toluene to make stock solutions of high concentration ( $\approx 1\%$  trichlorosilane by weight). These stock solutions were diluted to a final concentration of 2 mmol of trichlorosilane per kilogram of solution. Trichlorosilane SAMs were deposited by submerging UVO-treated silicon substrates into deposition solutions in tightly-sealed containers for  $\approx 16$  hours. After SAM formation, the substrates were removed from the deposition solutions, quickly rinsed with toluene, and blow-dried with nitrogen gas. Several replicas of each sample were made in order to establish the properties of the pre- and post- asphaltene treated SAMs, and generate sufficient level of confidence in our adsorption experiments.

Asphaltene solutions (0.5% w/w) were prepared by dissolving the precipitated, dry asphaltenes in the respective solvent, followed by overnight shaking. Prior to use, the solutions were filtered in order to remove any undissolved solids. The asphaltene treatment was accomplished by exposing the

SAM-covered substrates to these solutions for  $\approx 12$  hours. The samples were subsequently rinsed and sonicated in a respective pure solvent for 5 minutes in order to remove any weakly adsorbed asphaltenes or remaining precipitated particles. After sonication, the samples were rinsed with toluene and blow-dried with nitrogen gas.

### 3.3.3. *Spectroscopic ellipsometry*

The thicknesses of bare SAMs and SAM/asphaltene layers were determined with a variable angle spectroscopic ellipsometer (VASE) (J.A. Woollam Co.). Ellipsometry measures the difference in the polarization state between the light beams incident and reflected from the surface; it provides information about the thickness and dielectric properties of the film. Unless otherwise specified, ellipsometric data were collected at an incidence angle of  $75^\circ$  and at wavelengths ranging from 400 to 1100 nm in 20 nm increments. The ellipsometric angles  $\Psi$  and  $\Delta$  depend on the thickness and dielectric constant of the probed film. While in most cases one can determine the optical constants and thickness from the ellipsometric data, for very thin films these parameters are highly correlated and cannot be decoupled readily.<sup>27,28</sup> In order to estimate the thickness of the SAMs, we assumed the value of the index of refraction ( $n = 1.50$ )<sup>29</sup> and kept it constant through the fitting procedure. We note that

varying the refractive index of the film by  $\pm 0.05$  results in an uncertainty of approximately  $\pm 1 \text{ \AA}$ .<sup>30</sup> Even though we cannot determine the exact thickness of the film with complete certainty, the estimated thickness is important for comparison between different samples and previously published results.

#### 3.3.4. *Contact angle measurements*

Contact angles ( $\theta$ ) with deionized (DI) water as the probing liquid were measured with a Ramé-Hart contact angle goniometer (model 100-00). Static contact angles were determined after releasing an 8  $\mu\text{L}$  droplet of deionized water on the surface. To measure the advancing and receding contact angles (A-CA and R-CA, respectively), we captured the droplet with the syringe and added (advancing) or removed (receding) DI water from the droplet until the three phase contact line was displaced. This procedure was repeated for three different spots on each sample and the results were averaged. In our analysis, we assumed that A-CAs provide an estimate of the wettability of the SAMs. A densely-packed SAM of aliphatic chains should form a very hydrophobic surface, which exhibits a high water contact angle ( $\theta \approx 110^\circ$ ). In addition, the contact angle hysteresis (CAH), defined here as the difference between A-CA and R-CA, provides information about the chemical and structural heterogeneities of the

SAM. CAH of  $<10^\circ$  is generally considered a signature of a largely uniform surface.<sup>23</sup>

### 3.3.5. *Near-edge x-ray absorption fine structure (NEXAFS) spectroscopy*

NEXAFS data were collected at the NIST/Dow Materials Characterization Facility (beamline U7A) of the National Synchrotron Light Source at Brookhaven National Laboratory (Upton, NY). NEXAFS involves the excitation of core shell electrons by a monochromatic beam of soft x-rays and subsequent relaxation process involving the emission of Auger electrons and fluorescence radiation. NEXAFS can discriminate between different chemical elements by tuning the energy of the incoming synchrotron x-ray beam to match the energy of the elemental core shell electrons. Furthermore, resonances of specific electronic transitions from the core shell to unoccupied anti-bonding orbitals endow NEXAFS with sensitivity to the chemical environment of the film. The angle between the electric field vector of the x-ray beam and the sample normal was set to  $55^\circ$ ; in this geometry, the NEXAFS signal is approximately independent of the average molecular orientation in the film.<sup>31</sup> The x-ray absorption events were monitored with partial electron yield (PEY) and fluorescence yield (FY) detectors. The PEY detector was operated at a -150 V bias in order to detect only those electrons that originated from the topmost  $\approx 2$  nm of the sample.<sup>32</sup> The FY

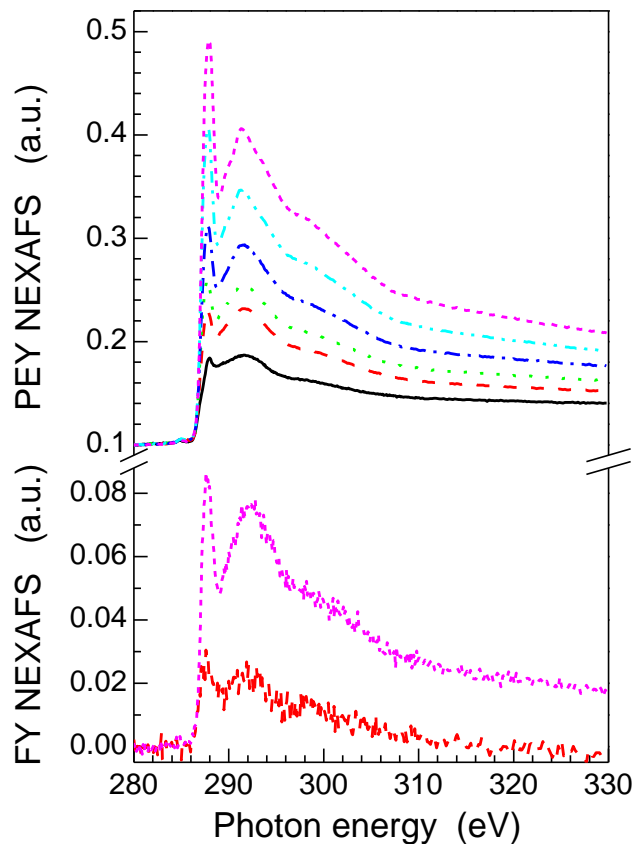


**Figure 3.1.** Partial electron yield (PEY, top) and fluorescence yield (FY, bottom) NEXAFS spectra at the “magic” angle of incidence ( $\theta = 55^\circ$ , where  $\theta$  denotes the angle between the surface normal and the electric vector of the x-ray beam) for alkyltrichlorosilanes of varying chain length: n-butyltrichlorosilane (—), n-octyltrichlorosilane (---), n-decyltrichlorosilane (·····), n-dodecyltrichlorosilane (---), n-hexadecyltrichlorosilane (---), n-octadecyltrichlorosilane (---). The pre-edge region of all the PEY spectra (around 280 eV) has been shifted up by 0.1 a.u. vertically for clarity.

detection mode is complementary to PEY in that it increases the probing depth of NEXAFS to hundreds of nanometers.<sup>31</sup> Monitoring both the PEY and FY provides information about the surface and bulk composition, respectively, of the films. One has to bear in mind that the signal-to-noise ratio depends crucially on the thickness of the probed film. In **Figure 3.1**, we plot PEY (top) and FY

(bottom) NEXAFS spectra for SAMs of trichlorosilanes of varying chain length. Although the FY signal allows for characterizing “bulk-like” structure of the films the signal-to-noise ratio is substantially decreased compared to PEY. Longer counting times are needed (5-10 times relative to PEY) in order to collect statistically meaningful spectra. The NEXAFS edge jump is defined as the difference between the post-edge region (arbitrarily chosen at  $\approx 320$  eV) and the pre-edge region (arbitrarily chosen at  $\approx 280$  eV) of the spectrum. Depending on the detection method and the thickness of the probed film, the edge jump offers a convenient measure of the total amount of carbon probed in the film. In our experiments, the NEXAFS edge jump was monitored for at least three independent spots on each sample in order to assure the reproducibility of the data reported.

### **3.4. Results and Discussion**

SAMs represent an important tool for engineering surfaces through the modification of their physico-chemical properties.<sup>23</sup> Since their introduction in the 1980s by Sagiv and co-workers<sup>33-36</sup>, organosilanes on silica have been one of the most widely used methods for production of well-organized SAMs because of their thermal and chemical stability. The stability of organosilane SAMs results from covalent bonding of organosilanes to the substrate as well as an in-plane

polysiloxane network formed among neighboring molecules proximal to the substrate.<sup>33,37,38</sup> This network endows organosilane-based SAMs with much higher stability relative to other SAMs, for example, those formed by assembling thiol-based moieties on noble metal surfaces. Wasserman et al.<sup>39</sup> employed ellipsometry, contact angle, XPS, and x-ray reflectivity to characterize the structure, stability, and reactivity of SAMs of n-alkyltrichlorosilanes of varying chain lengths. The authors reported that the SAMs formed possessed very high packing density for chain lengths larger than 4 carbon atoms; their data support a model of chains with an all-trans configuration oriented nearly parallel to the surface normal.

We prepared SAMs made of BTS, HTS, OTS, DTS, DDTs, HDTS, and ODTS using the protocols outlined in the Materials and Methods section. The bare SAMs were characterized thoroughly prior to the deposition of asphaltenes to investigate the effects of the thickness, wettability, and carbon content of the films on the extent of asphaltene adsorption. The ellipsometric thickness of the SAMs as a function of the number of carbon atoms in the alkyl mesogen of the organosilane chain ( $N_C$ ) is plotted in **Figure 3.2**. The different symbols in **Figure 3.2** denote samples prepared and characterized at different times. The thicknesses of the SAMs are reproducible from experiment to experiment and are consistent with results reported previously in the literature. The gray bars

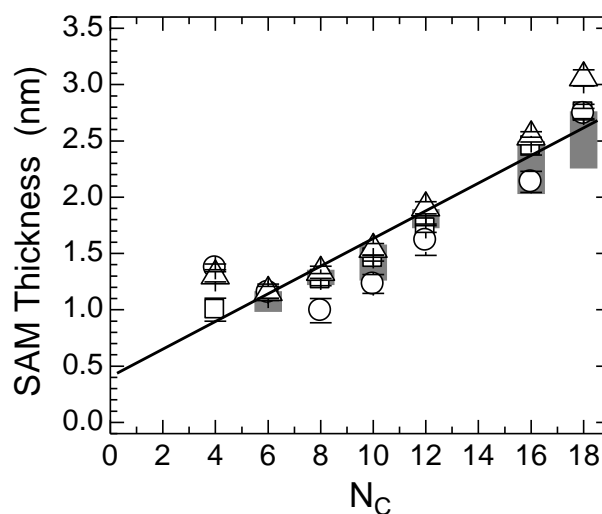


**Figure 3.2.** The thicknesses of the SAM measured by ellipsometry as a function of  $N_c$  for experiments collected during different times: November 2007 (□), March 2008 (○) and April 2008 (△). The grey bars represent the range of thicknesses reported by Wasserman et al.<sup>39</sup> The dotted line represents the best linear fit through the data.

behind the data in **Figure 3.2** represent the range of SAM thicknesses reported by Wasserman et al.<sup>39</sup> The close agreement between our data and the results reported by Wasserman et al. is remarkable given that organosilane SAMs are well known for their lack of reproducibility between different laboratory facilities and preparation protocols. We should mention that the thicknesses reported by Wasserman were obtained by assuming that the refractive index of the film is 1.45, which is different than the one assumed here. As mentioned earlier, this assumption introduces thickness uncertainties in the sub-Angström regime; these results are thus consistent despite the difference in the refractive index. The ellipsometric results support a model of alkyl chains in an all-trans

configuration and oriented parallel to the surface normal. A best linear fit of the data yields the equation:

$$t(N_c) = 1.23N_c + 4.09, \quad (1)$$

where  $t(N_c)$  is the thickness of the SAM in Angströms and  $N_c$  is the number of carbon atoms in the alkyltrichlorosilane chain. The thickness of the SAM increases by 1.23 Å per carbon atom in the organosilane molecule, a value that closely resembles that obtained by Wasserman et al. Extrapolation of the data to  $N_c = 0$  results in an intercept of  $\approx 4.09$  Å; this value is consistent with the size of the head group in the SAM forming molecules. In addition to the head-group, a small amount of adventitious impurities might also contribute to the positive value of the intercept in equation 1.

In order to determine the carbon content of the SAMs we extract the edge jump from the NEXAFS spectra and monitor its variations with chain length (*cf.* **Figure 3.3**). The proper interpretation of the edge jump requires consideration of the probing depth of the detection method (PEY vs. FY) and the thickness of the probed material. **Figure 3.3** depicts the (a) PEY and (b) FY NEXAFS edge jumps as a function of  $N_c$  for the alkyltrichlorosilane SAMs (open symbols). The PEY edge jump increases steadily with increasing  $N_c$  due to the increased amount of carbon present in the SAM. Extrapolation of the PEY edge jump data to  $N_c = 0$  yields a value of the edge jump of  $\approx 0.03$  in the arbitrary unit scale. In

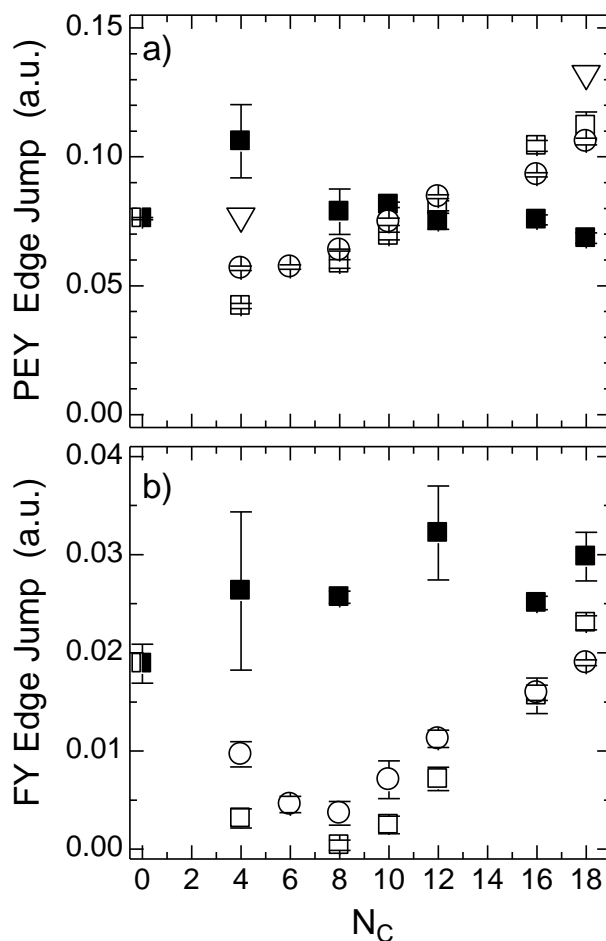


**Figure 3.3.** The PEY (a) and FY (b) NEXAFS edge jump as a function of  $N_C$  for bare SAMs (open symbols) and asphaltene-treated SAMs (closed symbols). The data presented have been collected during various time periods: March 2007 (triangles), November 2007 (squares), and March 2008 (circles). The PEY and FY signals corresponding to bare silica treated with asphaltenes are shown for comparison (a half-filled symbol at  $N_C = 0$ ).

contrast to the ellipsometry data, we cannot attribute this to the size of the head-group in the organosilane molecule because NEXAFS data collected at the carbon K-edge is only sensitive to carbon atoms at the photon energies used. Several factors may contribute to the positive value of the intercept. First, there may be

small amounts of adventitious carbon adsorbed on the surface. Second, we recall that the probing depth of the PEY NEXAFS technique is  $\approx 2$  nm<sup>32</sup> and that the thickness of SAMs with  $N_C > 12$  is higher than the probing depth. This will result in lower than expected edge jumps for the long alkyl chains. Finally, the SAMs with  $N_C < 8$  have a propensity to form multilayers, resulting in higher edge jump values. The combined effects of these three factors may explain the positive intercept of the edge jump trend. We provide a detailed account of the PEY data in relation to the SAM thickness in the **Appendix B**. Similar to the PEY, the FY data increases with increasing  $N_C$ . In the FY case, however, the extrapolated value at  $N_C = 0$  yields a negative intercept; moreover, there are strong deviations from the aforementioned trend for  $N_C < 8$ . We attribute the FY trends to the inability of the FY detector to collect sufficient signal from very short SAMs. Thus, because of technical limitations, a certain minimum amount of carbon atoms needs to be probed to detect a meaningful FY signal. It appears that for the setup used, this minimal signal threshold would correspond to  $N_C \approx 8$ . The data in **Figure 3.3** additionally include experiments performed at different dates, revealing the scatter induced by changes in the state of the detectors as well as demonstrating the high level of reproducibility of this measurement.

In **Figure 3.4**, we plot the advancing contact angles and the CAH as a function of  $N_C$ . The A-CAs exhibit two different trends for two distinct sets of

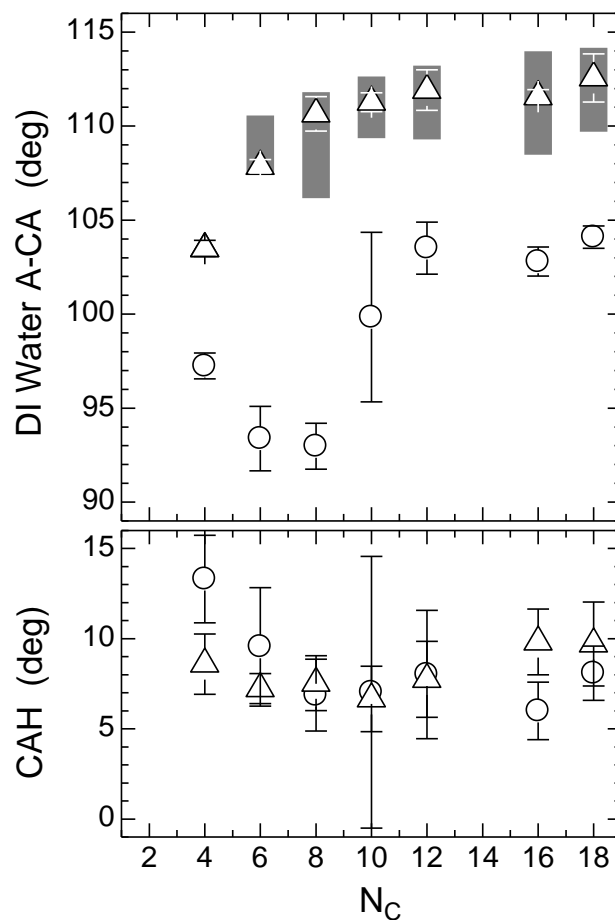


**Figure 3.4.** The advancing contact angle (top) and the contact angle hysteresis (bottom) as a function of  $N_c$  are shown for the March 2008 ( $\circ$ ) and April 2008 ( $\triangle$ ) experiments. The grey bars represent the range of contact angles reported by Wasserman et al.<sup>39</sup>

samples prepared. The samples prepared in March 2008 (open circles) exhibit increasing values of the A-CA with increasing  $N_c$ , ranging from  $\approx 93^\circ$  to a maximum of  $\approx 104^\circ$ . This set of samples also exhibits a sharp increase in the A-CA upon increasing  $N_c$  from 7 to 9. The samples prepared in April 2008 (open triangles) exhibit a constant A-CA as a function of alkyl chain length, except in

the regime of very short chains, where a decrease in the A-CA is detected. The April 2008 data are in close agreement with literature values as can be seen by the range of values extracted from Wasserman's work (grey lines in **Figure 3.4**). These two trends in the CA data suggest that the samples made in March 2008 did not pack as densely as expected. Despite the lower packing density of the March 2008 sample set, these experiments provide insight into the importance of surface wettability on asphaltene adsorption, as will be discussed below. The CAH does not exhibit a strong dependence on alkyl chain length; it also does not exhibit the anomalous behavior seen in the A-CA data. This observation suggests that although the March 2008 samples have lower packing densities, and are therefore less hydrophobic, they possess a degree of chemical and structural homogeneity similar to that of the other data sets.

While the ellipsometry and NEXAFS edge jump data suggest that all the SAMs studied here exhibit similar physical properties, the contact angle data show significant variation for one of the experimental trials. Although, the March 2008 samples exhibit consistent thicknesses and carbon content according to ellipsometry and NEXAFS, their advancing contact angles reveal clear deviations from the expected values. Proceeding with the asphaltene adsorption experiments without wettability data would have suggested that all SAMs were of equivalent quality and would have caused problems in the interpretation of

the data. Therefore, we highlight the importance of characterizing engineered SAM surfaces with a wide range of experimental techniques, as they often complement one another and no single technique can offer the full description of the system studied.

The extent of asphaltene adsorption can be studied by monitoring the variations in the edge jump before and after asphaltene treatment (*cf.* **Figure 3.3**). Because the adsorption of asphaltenes onto the SAMs results in an increase in the carbon content of the surface, it should be accompanied by an increase in the measured NEXAFS edge jump. The PEY edge jump NEXAFS data (*cf.* **Figure 3.3a**) reveal that with SAMs formed from alkyltrichlorosilanes with  $N_C \leq 12$ , the edge jump increases upon asphaltene adsorption. Conversely, SAMs with  $N_C > 12$  exhibit a *decrease* in the edge jump. This deviation from the expected trends in the PEY data can be explained by considering the total thickness of the organic films upon asphaltene adsorption, the carbon density of the SAMs relative to the carbon density of passively adsorbed asphaltene films, and the probing depth of PEY NEXAFS. As discussed above, the thickness of the short alkyl chain SAMs is below the probing depth of PEY NEXAFS, which has been estimated by Sohn et al. to be  $\approx 2$  nm.<sup>32</sup> Hence these SAMs yield a small edge jump signal. When asphaltenes are adsorbed on short-alkyl-chain SAMs, the thickness of the overall organic film increases and the total amount of carbon

probed increases, resulting in a net increase in the edge jump. However, for the long alkyl chain SAMs ( $N_C > 12$ ) there is a net decrease in the PEY edge jump upon asphaltene adsorption. This decrease, although counterintuitive, is explained by recalling that the thickness of long chain length SAMs likely exceeds the probing depth of PEY NEXAFS. Auger electrons originating from long alkyl chain SAMs lose some energy while going through the asphaltene layer, resulting in electrons that cannot reach the PEY detector and therefore the attenuation of the PEY NEXAFS signal (for detailed discussion see **Appendix B**). Additionally, if one assumes that the SAMs and the adsorbed asphaltene layer have equal carbon densities, one would expect the PEY NEXAFS edge jump signal to either remain constant or increase as the asphaltene adsorb. Instead, we detect that the PEY NEXAFS edge jump signal decreases, indicating that the carbon density of the asphaltene layer is likely to be lower than that of the densely packed SAMs. It is not surprising that the layer of passively adsorbed asphaltene has a lower carbon atomic density than the SAMs. It is well known that asphaltene self-assemble in solution to form supramolecular aggregates that subsequently adsorb to the exposed surfaces. These bulk aggregates are known to entrain as much as 50% (v/v) solvent in the case of toluene.<sup>20,40</sup> Upon exposure of the asphaltene layer to a  $N_2$  stream and to the high vacuum of the NEXAFS experiments, the solvent is removed from the asphaltene aggregates. The

presence of fused ring aromatic moieties in asphaltenic molecules, and their mutual orientation and juxtaposition in neighboring molecules, likely prevents the films from completely collapsing upon solvent removal. As a consequence, the asphaltenic molecules form a layer with significantly lower carbon atomic density relative to that of the well-packed hydrophobic aliphatic SAMs. Although this important information was obtained by means of the PEY NEXAFS measurements, the relatively shallow probing depth and difficulties associated with interpreting the amount of adsorbed asphaltenes with the PEY NEXAFS method highlight the need for complementary FY NEXAFS data to determine unambiguously the net amount of adsorbed asphaltenes.

In **Figure 3.3b** we plot the FY NEXAFS edge jump before (open symbols) and after (solid symbols) asphaltene adsorption. With FY NEXAFS detection, the adsorption of asphaltenes always results in an increase in the edge jump signal, albeit a modest one for HDTS and ODTS SAMs. This is due to the large probing depth of the FY detection mode. The data in **Figure 3.3b** demonstrate that the FY NEXAFS edge jump of the bare SAMs increases with increasing  $N_C$ . By contrast, the magnitude of the FY edge jump for asphaltene-treated SAMs remains approximately constant. These trends provide direct evidence that the amount of adsorbed asphaltenes on the SAM surfaces decreases with increasing  $N_C$  as will be discussed in detail later in this paper.

In order to further explicate the NEXAFS data, in **Figure 3.3** we plot the PEY and FY NEXAFS edge jump signals collected from a sample comprising an asphaltene layer adsorbed directly onto the silica substrate (half-filled square). The thickness of the resulting asphaltene layer is larger than the probing depth of PEY NEXAFS, as assessed by ellipsometry. The magnitude of the PEY NEXAFS edge jump collected from the asphaltene/SiO<sub>x</sub> sample is very close to the edge jumps of the asphaltene-treated SAMs but lower than the edge jumps of the thickest SAMs. This observation supports our earlier claim that the density of the asphaltene layer is lower than that of a well-organized SAM and that the decreases in the edge jump upon asphaltene adsorption are likely due to attenuation of the SAM signal. The FY NEXAFS edge jump signal from a bare asphaltene-treated silicon wafer is also close to the signal of the asphaltene-treated SAMs, albeit slightly lower. While the asphaltene film is completely probed with FY NEXAFS, there is no contribution from the absent SAM, resulting in a slightly lower edge jump.

In order to verify the extent of asphaltene adsorption, we performed ellipsometry measurements on the asphaltene-treated SAMs. A three-layer model was employed in estimating the increase in thickness due to asphaltene adsorption. The first and second layers represent the native silicon oxide and the SAM, respectively. The SAM layer is modeled as described before; its thickness is

fixed to that for the bare SAMs shown in **Figure 3.2**. The third layer represents the asphaltene layer; this layer is modeled by a uniform slab of constant index of refraction,  $n_{\text{asph}}$ , set to 1.8, a value obtained from ellipsometry measurements of spun-coated asphaltene from toluene solutions on clean silicon substrates.<sup>18</sup> Due to the large thickness of the spun-coated asphaltene layer, the optical constants and thickness can be determined simultaneously and independently from the ellipsometry measurements. We note that  $n_{\text{asph}} = 1.8$  is larger than the value normally estimated for asphaltenes in solution. Given that fused polyaromatic moieties can have refractive indices as high as  $\approx 2.2$ <sup>41</sup> and that asphaltenes comprise approximately 60% aromatic hydrocarbons,<sup>21</sup> one can estimate using an effective medium approximation<sup>42</sup> that the refractive index of asphaltenes should be  $\approx 1.9$ . Although this estimated value is higher than the one measured by ellipsometry in this work, the apparent discrepancy can be explained by the inclusion of free volume in the asphaltenic aggregates, which are generated upon evaporation of entrained solvent as explained above. We note that  $n_{\text{asph}}$  measured in an asphaltene spun-coated onto silica may differ slightly from that present in SAM-based layers because the packing density and chemical fractionation in these two sets of samples may not necessarily be equivalent. Nevertheless, given this approximation, assuming that  $n_{\text{asph}} = 1.8$  provides a

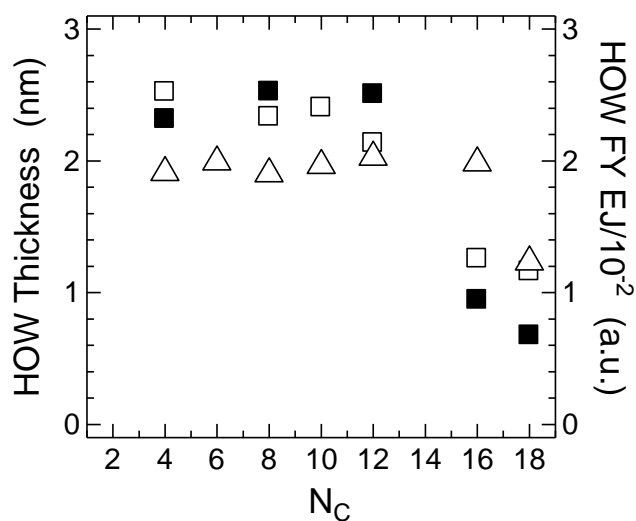


**Figure 3.5.** The thickness (open symbols, left ordinate) and the FY NEXAFS edge jump of asphaltene layers (closed symbols, right ordinate) adsorbed from toluene solutions and as a function of  $N_C$  in the underlying SAM. While the asphaltene layer thicknesses were measured directly by ellipsometry, the FY NEXAFS data were obtained by subtracting FY NEXAFS values collected from bare SAMs from those of the SAM/asphaltene specimens. The various symbols corresponds to data collected in November 2007 (□ and ■) and April 2008 (△).

convenient means of estimating and comparing the asphaltene layer thickness from sample to sample.

The thickness of the asphaltene layer adsorbed from toluene solutions as a function of  $N_C$  is shown for two independent sets of experiments in **Figure 3.5** (open symbols). The extent of asphaltene adsorption is nearly constant in the range of  $3 < N_C < 16$ . Upon increasing  $N_C$  in the SAM, the adsorbed amount of asphaltenes decreases sharply relative to the shorter SAMs. This result supports previous work on similar systems,<sup>18</sup> in which the adsorption of asphaltene was found to decrease with increasing thickness of the SAMs, an effect that was

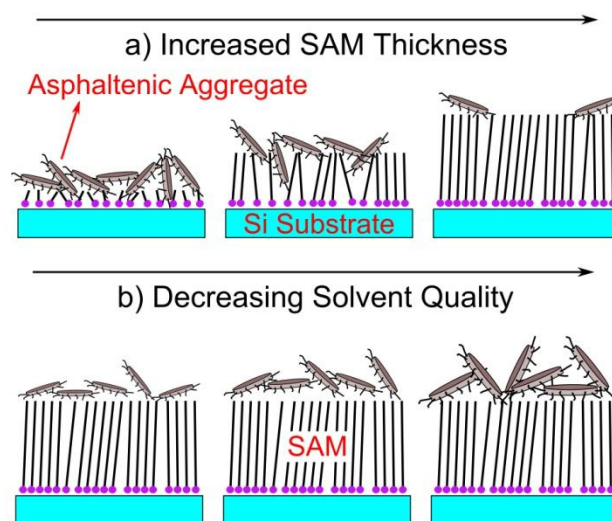


**Figure 3.6.** Schematics of asphaltenes adsorbed on alkyltrichlorosilane modified silica substrates. a) Variations in adsorption with increased thicknesses, b) variations in thickness of adsorbed asphaltenes when decreasing solvent quality.

attributed to the decrease of the interaction between asphaltenes and the underlying silica substrate, as depicted schematically in **Figure 3.6a**. The data in **Figure 3.5** also reveal the contribution of the adsorbed asphaltenes on the SAMs of varying  $N_c$  to the FY NEXAFS edge jump signal of these samples. The results are consistent with ellipsometric data on the same samples (open squares) and confirm clearly a decrease in the adsorption of asphaltenes with increasing thickness of the SAM and the ability of FY NEXAFS to probe the entire thickness of the SAM/asphaltene films.

In addition to determining the dependence of the extent of asphaltene adsorption on the  $N_c$  in the alkyltrichlorosilane SAMs, we established that the

hydrophobicity of the SAM layer is of great importance in preventing the adsorption of asphaltenes and enhancing the reproducibility of the results. In **Figure 3.4**, we showed that SAMs with similar carbon content could exhibit different A-CAs, indicating that some experiments produced SAMs of lower hydrophobicity. We attributed this behavior to lower grafting density of the SAM molecules,  $\sigma_{\text{SAM}}$ , on the substrate. In **Figure 3.7**, we plot the asphaltene thickness as determined with ellipsometry as a function of the negative cosine of the A-CA of the bare SAMs,  $-\cos(\theta_{\text{SAM}})$ .<sup>43</sup> Note that because  $\cos(\theta_{\text{SAM}})$  is proportional to the surface energy of the SAM substrate, it provides a measure of the cumulative effect of the SAM thickness (or equivalently  $N_{\text{C}}$ ) and  $\sigma_{\text{SAM}}$ . From the data in **Figure 3.7**, the extent of asphaltene adsorption tends, for the most part, to decrease with increasing A-CAs. The higher wettabilities (*i.e.*, lower A-CAs) are attributed to SAM layers that did not pack as densely as expected possibly exposing methylene groups and/or the underlying polar silica to the asphaltene solution. This leads to a less obstructed interaction between the asphaltenes and the silica substrate. We therefore conclude that it is the coverage of the substrate by the SAMs, defined as a product of  $N_{\text{C}}$  and  $\sigma_{\text{SAM}}$ , which governs the effectiveness of the alkane “buffer” layer in minimizing the number of asphaltene/silica contacts.

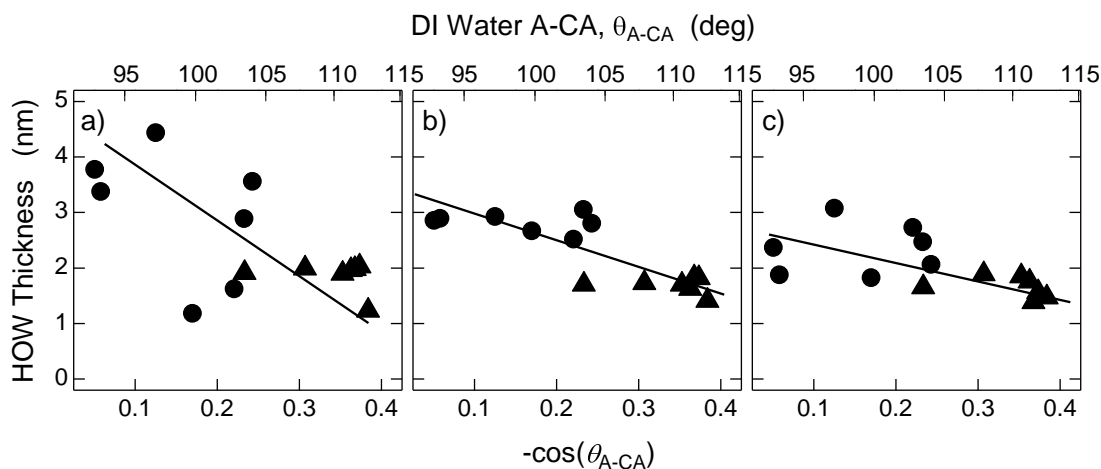


**Figure 3.7.** The thickness of the asphaltene adsorbed film as a function of the negative cosine of the SAM advancing DI water contact angle collected in the March 2008 (●) and April 2008 (▲) experiments are shown for various solvents including: (a) toluene, (b) tetralin, (c) methylnaphthalene.

Previous work established that a transition from liquid-like to semicrystalline-like structure of alkane-based SAMs occurs at  $N_c$  between 11 and 12.<sup>25,44-46</sup> While we have not measured the conformation of the organosilanes in our SAM layers in this work directly, looking back at the data shown in **Figure 3.4** it is tempting to attribute the sharp decrease in HOW at  $N_c=12$  to the formation of more-ordered semicrystalline SAMs, which would be more efficient in shielding the underlying silica substrate. Quantification of this conformational transition and its effect on adsorption will be the focus of future work.

In addition to the affinity to the  $\text{SiO}_x$  substrate, the extent of adsorption of any solute from the liquid phase depends on the substrate/solvent and

solvent/solute interactions. So far, we have discussed adsorption of asphaltenes from toluene solutions and addressed the effect of modifying the characteristics of the underlying substrate, which affected the extent of the asphaltene/substrate interactions. We note that in our analysis involving SAMs with different densities and length, we have ignored possible effects arising from various substrate/solvent effects. We now briefly address the effect of solvent quality on the extent of asphaltene adsorption on alkyl SAMs. In **Figure 3.7** we plot the HOW thickness for asphaltene adsorption from toluene (a), tetralin (b) and 1-MN (c) after sonication onto a variety of SAMs of varying  $N_c$  and carbon densities. The extent of asphaltene adsorption for 1-MN and tetralin are similar to those of toluene suggesting either that the initial adsorption from these solvents is similar, or that all these solvents are equally effective at removing asphaltenes from the surface during the sonication step. In order to discriminate between the initial adsorption of asphaltenes from different solvents and the ability of these solvents to clean the surface during the sonication step, we measured the amount of adsorbed asphaltenes on ODTs substrates of equivalent packing density before and after sonication. The data in **Figure 3.8a** depict the thickness of the adsorbed asphaltenes before (closed symbols) and after (open symbols) the sonication step as a function of the Hildebrand solubility parameter ( $\delta$ ) of the solvent.<sup>47</sup> The asphaltene adsorption increases in the following order:

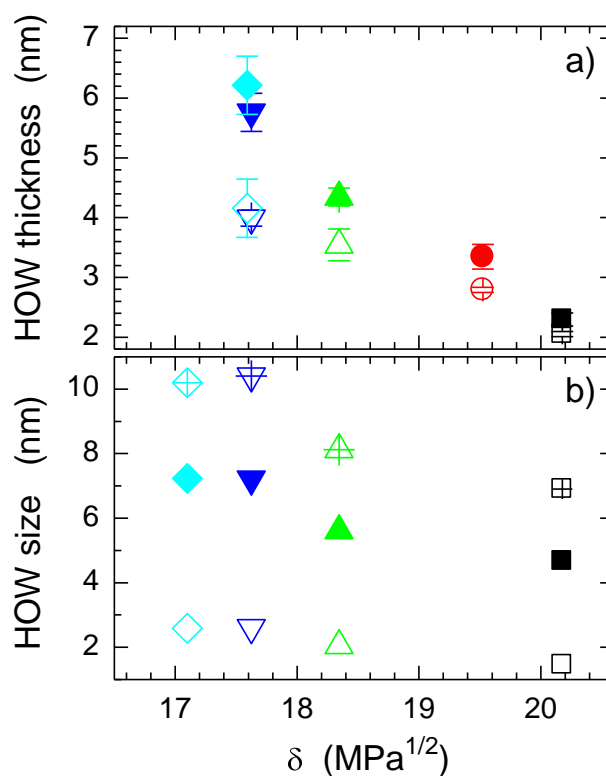


**Figure 3.8.** (a) Thickness of the asphaltene adsorbed film before (closed symbols) and after (open symbols) sonication in parent neat solvent and (b) the aggregate size (aggregate diameter: crossed symbols, aggregate thickness: open symbols, aggregate average radius of gyration: closed symbols) as a function of the Hildebrand solubility parameter of the solvent. The solvents used are heptol (cyan diamond), decalin (blue down-triangle), toluene (green up-triangle), tetralin (red circle), and 1-methylnaphthalene (black square). The composition of heptol in samples in Figure 3.8a is 20:80 (w/w), while that in samples in Figure 3.8b is 60:40 (v/v). The data in Figure 3.8b have been adopted from reference 22.

1-MN < tetralin < toluene < decalin < heptol (20:80 w/w n-heptane:toluene).

Note that the solubility parameter of the solvent increases in the same manner.

The value of  $\delta$  of asphaltenes has been estimated to range between 19.5 and 20.5

MPa<sup>1/2</sup>.<sup>48-50</sup> From the data in **Figure 3.8a** the thickness of the asphaltene layer

both before and after sonication in the neat solvent decreases systematically

with increasing  $\delta$ . This trend is identical to the variation of asphaltene aggregate size measured earlier by small-angle neutron scattering experiments<sup>22</sup> (*cf.* **Figure 3.8b**). Because asphaltenes are known to form oblate cylindrical supramolecular aggregates, it is tempting to conclude that roughly a monolayer of aggregates adsorbs on these surfaces. The mean diameter of these discoidal aggregates (crossed symbols in **Figure 3.8b**) varies from 7 nm in 1-MN to slightly more than 10 nm in decalin and mixtures of heptane and toluene. The thickness of these aggregates (open symbols in **Figure 3.8b**) is 1.5-2.6 nm, depending on solvent quality.<sup>20,22,40</sup> The adsorbed asphaltene thickness in **Figure 3.8a**, before and after sonication suggests that upon adsorption a wide distribution of orientations of these discoidal aggregates may exist on the surface, with some of the aggregates adsorbed face on and some adsorbed edge on. Sonication may remove the more weakly adsorbed aggregates. The difference between aggregate diameter and thickness is greatest for the larger aggregates, those adsorbed from heptane/toluene mixtures and decalin, and it is smallest for the best solvent 1-MN. This may explain the trend in **Figure 3.8a**, in which large amounts of asphaltenes are removed from the surface upon sonication in heptol while few asphaltenes are detached when the sonicating medium is 1-MN. These observations are schematically depicted in **Figure 3.6b** and indicate that, in addition to the physico-chemical properties of the surface,

the solution state of the asphaltenic aggregates plays an important role in the ability of the asphaltenes to be adsorbed onto and cleaned from solid surfaces.

### **3.5. Conclusions**

We have shown that chemical modification of model silicon substrates with organosilane SAMs results in coatings capable of minimizing asphaltene adsorption. Considering that organosilane coatings can generally be applied to a wide range of substrates, including oxide-coated materials used in petroleum pipelines, the findings reported here could aid in an effective design of coatings enabling protection of oil-transport pipelines against asphaltene adsorption and accumulation. Contact angle measurements, spectroscopic ellipsometry, and NEXAFS spectroscopy have been employed to determine the extent of asphaltene adsorption onto model SAMs made of trichlorosilanes with varying chain lengths. Our measurements and analysis reveal that the most important factor governing the adsorption of asphaltenes onto the substrates is the ability of the SAM layer to shield the underlying silica substrate from interacting with the polar functional groups on the asphaltenic aggregates present in solution. This conclusion was reached by noting a decrease in asphaltene adsorption with increasing thickness of the SAM layers. Additionally, experiments performed on SAMs that exhibited lower than expected A-CAs revealed increased amounts of

adsorbed asphaltenes. This observation was reconciled by considering the lower packing density of the SAM molecules likely in those surfaces with lower A-CAs, which in turn results in a higher exposure of the silicon substrate to the asphaltene solution. Adsorption experiments from different solvents revealed that asphaltene adsorption decreased with increasing the solubility parameter of the deposition solvent for all solvents studied here. In the analysis of these adsorption experiments, we explored some of the considerations necessary when performing NEXAFS spectroscopy studies of thin films. Specifically, we compared PEY and FY NEXAFS detection modes and discussed their limitations and advantages. We demonstrated that careful consideration should be given to the thickness of the probed film, its atomic density as a function of depth from the surface and the probing depth of the detection mode used in NEXAFS.

### 3.6. References

1. Leontaritis, K. J.; Ali Mansoori, G. Asphaltene Deposition: A Survey of Field Experiences and Research Approaches. *J. Pet. Sci. Eng.* **1988**, *1*, 229-239.
2. Speight, J. G. In *The Chemistry and Technology of Petroleum*; Chemical Industries; Marcel Dekker, Inc.: New York, 1999; Vol. 76, pp 918.
3. Drummond, C.; Israelachvili, J. Fundamental Studies of Crude Oil-Surface Water Interactions and its Relationship to Reservoir Wettability. *J. Pet. Sci. Eng.* **2004**, *45*, 61-81.
4. Toulhoat, H.; Prayer, C.; Rouquet, G. Characterization by Atomic-Force Microscopy of Adsorbed Asphaltenes. *Colloids Surf., A* **1994**, *91*, 267-283.

5. Akhlaq, M. S.; Götze, P.; Kessel, D.; Dornow, W. Adsorption of Crude Oil Colloids on Glass Plates: Measurements of Contact Angles and the Factors Influencing Glass Surface Properties. *Colloids Surf., A* **1997**, *126*, 25-32.
6. Dudášová, D.; Simon, S.; Hemmingsen, P. V.; Sjöblom, J. Study of Asphaltenes Adsorption Onto Different Minerals and Clays: Part 1. Experimental Adsorption with UV Depletion Detection. *Colloids Surf., A* **2008**, *317*, 1-9.
7. Batina, N.; Manzano-Martinez, J. C.; Andersen, S. I.; Lira-Galeana, C. AFM Characterization of Organic Deposits on Metal Substrates from Mexican Crude Oils. *Energy Fuels* **2003**, *17*, 532-542.
8. Batina, N.; Reyna-Cordova, A.; Trinidad-Reyes, Y.; Quintana-Garcia, M.; Buenrostro-Gonzalez, E.; Lira-Galeana, C.; Andersen, S. I. Qualitative Analysis of Thin Films of Crude Oil Deposits on the Metallic Substrate by Fourier Transform Infrared (FTIR) Microscopy. *Energy Fuels* **2005**, *19*, 2001-2005.
9. Castillo, J.; Goncalves, S.; Fernández, A.; Mujica, V. Applications of Photothermal Displacement Spectroscopy to the Study of Asphaltenes Adsorption. *Opt. Commun.* **1998**, *145*, 69-75.
10. Acevedo, S.; Castillo, J.; Fernandez, A.; Goncalves, S.; Ranaudo, M. A. A Study of Multilayer Adsorption of Asphaltenes on Glass Surfaces by Photothermal Surface Deformation. Relation of this Adsorption to Aggregate Formation in Solution. *Energy Fuels* **1998**, *12*, 386-390.
11. Acevedo, S.; Ranaudo, M. A.; Garcia, C.; Castillo, J.; Fernandez, A.; Caetano, M.; Goncalvez, S. Importance of Asphaltene Aggregation in Solution in Determining the Adsorption of this Sample on Mineral Surfaces. *Colloids Surf., A* **2000**, *166*, 145-152.
12. Acevedo, S.; Ranaudo, M. A.; Garcia, C.; Castillo, J.; Fernandez, A. Adsorption of Asphaltenes at the Toluene-Silica Interface: A Kinetic Study. *Energy Fuels* **2003**, *17*, 257-261.
13. Ekholm, P.; Blomberg, E.; Claesson, P.; Auflem, I. H.; Sjöblom, J.; Kornfeldt, A. A Quartz Crystal Microbalance Study of the Adsorption of Asphaltenes and Resins Onto a Hydrophilic Surface. *J. Colloid Interface Sci.* **2002**, *247*, 342-350.

14. Xie, K.; Karan, K. Kinetics and Thermodynamics of Asphaltene Adsorption on Metal Surfaces: A Preliminary Study. *Energy Fuels* **2005**, *19*, 1252-1260.
15. Dudášová, D.; Silset, A.; Sjöblom, J. Quartz Crystal Microbalance Monitoring of Asphaltene Adsorption/Deposition. *J. Dispersion Sci. Technol.* **2008**, *29*, 139-146.
16. Abdallah, W. A.; Taylor, S. D. Surface Characterization of Adsorbed Asphaltene on a Stainless Steel Surface. *Nucl. Instrum. Methods Phys. Res., Sect. B* **2007**, *258*, 213-217.
17. Labrador, H.; Fernandez, Y.; Tovar, J.; Munoz, R.; Pereira, J. C. Ellipsometry Study of the Adsorption of Asphaltene Films on a Glass Surface. *Energy Fuels* **2007**, *21*, 1226-1230.
18. Turgman-Cohen, S.; Smith, M. B.; Fischer, D. A.; Kilpatrick, P. K.; Genzer, J. Asphaltene Adsorption Onto Self-Assembled Monolayers of Mixed Aromatic and Aliphatic Trichlorosilanes. *Langmuir* **2009**, *25*, 6260-6269.
19. Alboudwarej, H.; Pole, D.; Svrcek, W. Y.; Yarranton, H. W. Adsorption of Asphaltenes on Metals. *Ind. Eng. Chem. Res.* **2005**, *44*, 5585-5592.
20. Gawrys, K. L.; Kilpatrick, P. K. Asphaltenic Aggregates are Polydisperse Oblate Cylinders. *J. Colloid Interface Sci.* **2005**, *288*, 325-334.
21. Gawrys, K. L.; Blankenship, G. A.; Kilpatrick, P. K. On the Distribution of Chemical Properties and Aggregation of Solubility Fractions in Asphaltenes. *Energy Fuels* **2006**, *20*, 705-714.
22. Verruto, V. J.; Kilpatrick, P. K. Preferential Solvent Partitioning within Asphaltenic Aggregates Dissolved in Binary Solvent Mixtures. *Energy Fuels* **2007**, *21*, 1217-1225.
23. Ulman, A. In *An introduction to ultrathin organic films : from Langmuir-Blodgett to self-assembly*; Academic Press: Boston, 1991; , pp 442.
24. Hannisdal, A.; Ese, M.; Hemmingsen, P. V.; Sjöblom, J. Particle-Stabilized Emulsions: Effect of Heavy Crude Oil Components Pre-Adsorbed Onto Stabilizing Solids. *Colloids Surf., A* **2006**, *276*, 45-58.

25. Smith, M. B.; Efimenko, K.; Fischer, D. A.; Lappi, S. E.; Kilpatrick, P. K.; Genzer, J. Study of the Packing Density and Molecular Orientation of Bimolecular Self-Assembled Monolayers of Aromatic and Aliphatic Organosilanes on Silica. *Langmuir* **2007**, *23*, 673-683.
26. Spiecker, P. M.; Gawrys, K. L.; Kilpatrick, P. K. Aggregation and Solubility Behavior of Asphaltenes and their Subfractions. *J. Colloid Interface Sci.* **2003**, *267*, 178-193.
27. McCrackin, F. L.; Passaglia, E.; Stromberg, R. R.; Steinberg, H. L. Measurement of Thickness and Refractive Index of very Thin Films and Optical Properties of Surfaces by Ellipsometry. *J. Res. Natl. Bur. Stand. Sect. A* **1963**, *A 67*, 363-377.
28. McCrackin, F. L.; Passaglia, E.; Stromberg, R. R.; Steinberg, H. L. Measurement of the Thickness and Refractive Index of very Thin Films and the Optical Properties of Surfaces by Ellipsometry. *J. Res. Nat. Inst. Stand. Technol.* **2001**, *106*, 589-603.
29. Wasserman, S. R.; Whitesides, G. M.; Tidswell, I. M.; Ocko, B. M.; Pershan, P. S.; Axe, J. D. The Structure of Self-Assembled Monolayers of Alkylsiloxanes on Silicon: A Comparison of Results from Ellipsometry and Low-Angle x-Ray Reflectivity. *J. Am. Chem. Soc.* **1989**, *111*, 5852-5861.
30. Tillman, N.; Ulman, A.; Schildkraut, J. S.; Penner, T. L. Incorporation of Phenoxy Groups in Self-Assembled Monolayers of Trichlorosilane Derivatives - Effects on Film Thickness, Wettability, and Molecular-Orientation. *J. Am. Chem. Soc.* **1988**, *110*, 6136-6144.
31. Stöhr, J. In *NEXAFS Spectroscopy*; Springer Series in Surface Sciences 25; Springer-Verlag: New York, 1992; , pp 403.
32. Sohn, K. E.; Dimitriou, M. D.; Genzer, J.; Fischer, D. A.; Hawker, C. J.; Kramer, E. J. Determination of the Electron Escape Depth for NEXAFS Spectroscopy. *Langmuir* **2009**, *25*, 6341--6348.
33. Sagiv, J. Organized Monolayers by Adsorption. 1. Formation and Structure of Oleophobic Mixed Monolayers on Solid-Surfaces. *J. Am. Chem. Soc.* **1980**, *102*, 92-98.

34. Netzer, L.; Sagiv, J. A New Approach to Construction of Artificial Monolayer Assemblies. *J. Am. Chem. Soc.* **1983**, *105*, 674-676.
35. Netzer, L.; Iscovici, R.; Sagiv, J. Adsorbed Monolayers Versus Langmuir-Blodgett Monolayers—Why and how? II. Characterization of Built-Up Films Constructed by Stepwise Adsorption of Individual Monolayers. *Thin Solid Films* **1983**, *100*, 67-76.
36. Maoz, R.; Sagiv, J. On the Formation and Structure of Self-Assembling Monolayers. I. A Comparative ATR-Wettability Study of Langmuir-Blodgett and Adsorbed Films on Flat Substrates and Glass Microbeads. *J. Colloid Interface Sci.* **1984**, *100*, 465-496.
37. Finklea, H. O.; Robinson, L. R.; Blackburn, A.; Richter, B.; Allara, D.; Bright, T. Formation of an Organized Monolayer by Solution Adsorption of Octadecyltrichlorosilane on Gold - Electrochemical Properties and Structural Characterization. *Langmuir* **1986**, *2*, 239-244.
38. Allara, D. L.; Parikh, A. N.; Rondelez, F. Evidence for a Unique Chain Organization in Long-Chain Silane Monolayers Deposited on 2 Widely Different Solid Substrates. *Langmuir* **1995**, *11*, 2357-2360.
39. Wasserman, S. R.; Tao, Y. T.; Whitesides, G. M. Structure and Reactivity of Alkylsiloxane Monolayers Formed by Reaction of Alkyltrichlorosilanes on Silicon Substrates. *Langmuir* **1989**, *5*, 1074-1087.
40. Gawrys, K. L.; Blankenship, G. A.; Kilpatrick, P. K. Solvent Entrainment in and Flocculation of Asphaltenic Aggregates Probed by Small-Angle Neutron Scattering. *Langmuir* **2006**, *22*, 4487-4497.
41. McCartney, J. T.; Ergun, S. Refractive Index and Thickness of Ultrathin Sections of Coals and Graphite by Interferometry. *J. Opt. Soc. Am.* **1962**, *52*, 197-200.
42. Tompkins, H. G.; McGahan, W. A. In *12.4 Effective Medium Approximations (EMAs); Spectroscopic Ellipsometry and Reflectometry*; John Wiley & Sons, Inc.: New York, 1999; pp 125-126.

43. Using  $-\cos(\theta_{\text{SAM}})$  instead of  $\theta_{\text{SAM}}$  is physically more meaningful because based on the Young's equation,  $\cos(\theta_{\text{SAM}}) = (\gamma_{\text{SAM}} - \gamma_{\text{SAM/L}}) / \gamma_{\text{L}}$ , where  $\gamma_{\text{SAM}}$  is the surface energy of the SAM layer,  $\gamma_{\text{SAM/L}}$  is the interfacial energy at the SAM/probing liquid interface, and  $\gamma_{\text{L}}$  is the surface energy of the probing liquid;  $-\cos(\theta_{\text{SAM}})$  is thus directly proportional to the physico-chemical character of the SAM substrate and follows the same trend (*i.e.*, it either increases or decreases) as  $\theta_{\text{SAM}}$ .
44. Allara, D. L.; Parikh, A. N.; Judge, E. The Existence of Structure Progressions and Wetting Transitions in Intermediately Disordered Monolayer Alkyl Chain Assemblies. *J. Chem. Phys.* **1994**, *100*, 1761-1764.
45. Chaudhury, M. K.; Owen, M. J. Correlation between Adhesion Hysteresis and Phase State of Monolayer Films. *J. Phys. Chem.* **1993**, *97*, 5722-5726.
46. Snyder, R. G.; Strauss, H. L.; Elliger, C. A. C-H Stretching Modes and the Structure of Normal-Alkyl Chains .1. Long, Disordered Chains. *J. Phys. Chem.* **1982**, *86*, 5145-5150.
47. Yaws, C. L. In *Chemical properties handbook : physical, thermodynamic, environmental, transport, safety, and health related properties for organic and inorganic chemicals*; McGraw-Hill handbooks; McGraw-Hill: New York, 1999; , pp 779.
48. Hirschberg, A.; Dejong, L. N. J.; Schipper, B. A.; Meijer, J. G. Influence of Temperature and Pressure on Asphaltene Flocculation. *Society of Petroleum Engineers Journal* **1984**, *24*, 283-293.
49. Burke, N. E.; Hobbs, R. E.; Kashou, S. F. Measurement and Modeling of Asphaltene Precipitation. *J. Pet. Technol.* **1990**, *42*, 1440-1446.
50. Mannistu, K. D.; Yarranton, H. W.; Masliyah, J. H. Solubility Modeling of Asphaltenes in Organic Solvents. *Energy Fuels* **1997**, *11*, 615-622.

## CHAPTER 4

### COMPUTER SIMULATION OF CONTROLLED RADICAL POLYMERIZATION: EFFECT OF CHAIN CONFINEMENT DUE TO INITIATOR GRAFTING DENSITY AND SOLVENT QUALITY IN “GRAFTING FROM” METHOD

#### 4.1. Abstract

We use stochastic Monte Carlo simulation following the bond fluctuation model to study the effects of grafting density of surface-anchored initiators and solvent quality on controlled radical polymerization (CRP) from flat impenetrable substrates under good and poor solvent conditions. Our CRP model includes a mechanism for activation/deactivation of the chains and neglects termination and/or chain transfer reactions. The system is thus “truly living”. We find that under these polymerization conditions, surface-initiated polymerizations at low grafting densities resemble those in the bulk. In contrast, at high initiator grafting densities these surface-initiated polymerizations result in gradients of the free monomer and chain-end concentrations, which lead to an uneven growth of the chains and ultimately yield polymers with broad molecular

weight distributions. Poor solvent conditions exacerbate this problem further by collapsing the chains and in some cases forming chain aggregates, which further restrict the access of free monomers by the active polymer chain-ends and contribute to their uneven growth and ultimately broader length distributions relative to good solvent conditions. While at low grafting densities the molecular weight distributions can be described by the conventional Schulz–Zimm distribution function, at high grafting densities this approach fails to describe accurately the dispersity in chain lengths.

## **4.2. Introduction**

During the past decade, numerous research reports have demonstrated that specialty end-tethered polymer layers on surfaces can be generated by “grafting from” polymerization using controlled radical polymerization (CRP) schemes.<sup>1-10</sup> CRPs represent radical polymerizations in which equilibrium between active polymerizing chains and inactive dormant chains leads to controlled molecular weights and molecular weight distributions (MWDs).<sup>11,12</sup> The “grafting from” scheme consists of growing polymers directly from initiator-covered surfaces. In contrast to the “grafting onto” approach, in which polymers with reactive end-groups attach to the surface, the “grafting from” strategy is believed to yield dense brushes with controlled thickness, grafting densities and relatively

narrow MWDs characterized by a small polydispersity index (PDI). Despite the common use of CRP for the synthesis of end-tethered layers, there is a dearth of research characterizing the PDI of polymers produced from initiating surfaces. The current approach for the estimation of PDI in tethered layers involves the addition of free bulk initiators to the polymerization mixture and the subsequent analysis of the solution-synthesized polymers by size-exclusion chromatography (SEC) or an equivalent technique. The major drawback of this approach is that it neglects possible effects of surface confinement and diffusion of the reactive components to and from the propagating radical ends, which, in turn, affect the ability of CRP to yield grafted polymers with low PDI.

Surface-initiated atom transfer radical polymerization (SI-ATRP), and its various derivatives (*i.e.*, ARGET ATRP) are probably the most frequently used controlled-radical polymerization schemes employed in the formation of polymeric grafts on surfaces using the “grafting from” method.<sup>13,14</sup> The popularity of these methodologies has stemmed from their robustness, insensitivity to the presence of a small amount of impurities (most notable oxygen) that tend to terminate the radical processes and their ability to create copolymers and polymers with complex topologies. In spite of sizeable amount of work on this topic, our understanding of the “grafting from” process and complete characterization of the properties of grown macromolecular grafts has

been hindered by many technical limitations. As a result, contradicting reports have not been reconciled conclusively by means of our current knowledge.<sup>15-19</sup> For example, experimental studies performed by cleaving the surface-initiated polymers<sup>15-19</sup> report both increases<sup>15,16,18</sup> and similar<sup>17</sup> PDIs of the surface-grafted polymers relative to polymers grown in the solution. In addition, while most reports noted that “grafting from” polymerization resulted in polymers whose molecular weights were lower than polymers grown under identical experimental conditions in the bulk, Koylu *et al.* reported recently on the opposite trend.<sup>18</sup> These and other findings are not easy to understand without performing a comprehensive set of additional experiments involving SEC measurements with very sensitive concentration detectors. However, even with the available SEC measurements of surface-grown polymers, more information about the structure of the grafted layer is needed in order to comprehend the effect of the various process parameters that influence the “grafting from” mechanism. In spite of a tremendous progress in various instrumentation tools, no currently available analytical technique is capable of characterizing completely the structure of the grafted layer. Computer simulations and various molecular theories may prove useful because they provide monomer-level insight into the polymerization process that may not be accessible to experiments. These approaches further offer the opportunity to vary

systematically the parameters of the polymerization system and to characterize completely the properties of the molecular grafts without the limitations involved with experiments.

The variations in PDI investigated herein are relevant given that properties such as the brush height and the polymer concentration profile vary significantly when comparing grafted polymers with equal number average molecular weights ( $\langle N \rangle$ ) but differing MWDs.<sup>20-29</sup> For instance, using numerical self-consistent mean field theory de Vos and Leermakers<sup>29</sup> demonstrated recently that broadening of MWDs leads to changes of the shapes of the brush concentration profiles from parabolic to linear to concave and to corresponding increases in the brush layer thickness under good solvent conditions. The authors also noted that, interestingly, the scaling exponents for the brush height with respect to the molecular weight and the grafting density are identical for both monodisperse and polydisperse polymers. In a later study, the authors report on the effect of PDI on the anti-fouling properties of tethered polymers, which is an important application of these layers.<sup>30</sup> In this contribution, we build upon previous reports and investigate the effect of the initiator grafting density and the solvent quality on the properties of polymers initiated from flat substrates; and how they compare to bulk initiated reactions in athermal

solvents. The results provide information about the molecular weight, PDI, and concentration profiles for grafted polymers grown by CRP reactions.

Reports simulating and modeling surface-initiated polymerization have appeared previously. Wittmer et al.<sup>31</sup> studied the diffusive growth of a polymer layer by in-situ polymerization using a mean-field treatment and scaling theories of polymers in good solvents. Computer simulations utilizing the bond-fluctuation model (BFM) were used to verify the developed theory. Wittmer and coworkers considered a system in which initiators, which could commence irreversible growth of linear unbranched chains, covered densely an impenetrable wall. The authors further assumed that the chain growth was slow and, therefore, the chains retained their local equilibrium configuration during the polymerization process. An infinitesimal flux of incoming monomers then provided the reactants from which the polymers could grow. Wittmer et al. predicted that for diffusion-limited reactive growth the formed chains would be polydisperse but nonetheless strongly stretched away from the surface.

Numerous computer simulation studies have been performed on bulk- and surface-initiated equilibrium, “living” polymerizations, in which polymerization and depolymerization reactions were accounted for and the polymers were in chemical equilibrium with a population of free monomers. Using off-lattice and BFM Monte Carlo (MC) simulations Milchev and coworkers<sup>32</sup> reported briefly on

the effect of growing polymers from low and high initiator grafting densities that resulted in differences in their MWDs. Matyjaszewski et al.<sup>13</sup> also implemented computer simulations to investigate surface-initiated polymerizations. They constructed concentration profiles and computed the MWD of the simulation-grown polymers.

Recently, Liu and coworkers<sup>33</sup> reported on the effects of the polymerization rate and the density of initiating centers on the properties of macromolecules grown by “grafting from” polymerization from flat substrates by means of coarse-grained molecular dynamics. Liu et al. modeled a “true” living/controlled polymerization process by not considering any termination (or chain transfer) in their simulations. They demonstrated that decreasing the rate of polymerization resulted in polymeric grafts with lower PDI, relative to polymerization performed at higher rates. Liu et al. also reported on the interplay between the density of the initiators on the surface, their effectiveness of initiation, and polymerization rates. Specifically, the authors pointed out that in systems with low initiator density nearly all initiators started polymerization. At slow polymerization rates, all chains propagated at approximately the same rate. In contrast, at high densities of the initiator centers, initiation efficiency decreased with increasing rate of polymerization, which, in turn, resulted in a higher fraction of inactive initiators and higher PDIs.

A few years ago, one of us developed and presented a computer simulation model of controlled radical polymerization resembling processes occurring in ATRP by employing a stochastic MC scheme.<sup>34</sup> We described how  $\langle N \rangle$  and the MWD of polymers grown in bulk and on flat impenetrable surfaces depended on a number of parameters, such as, the concentrations of different species and the simulation equivalent to kinetic rates and equilibrium constants. We demonstrated that increasing the termination probability and/or decreasing the initial probability of addition of a new monomer to a growing chain broadened the MWD. Our results also indicated that confinement of surface-initiated polymers resulted in increased numbers of early terminations, which, in turn, led to higher PDIs. Upon increasing the grafting density of the initiators on the surface, we noted further increases in the PDIs of the grafted polymers.

The current work builds upon our previous MC study<sup>34</sup> and the work of Liu and coworkers<sup>33</sup> to investigate the effect that decreasing the solvent quality and/or grafting the initiators to the surface has on the broadness of the MWDs. By turning off the termination reaction and decreasing the rate of polymerization (in contrast to our previous work), we aim to model the “true living”/controlled radical process. In contrast with previous studies, we include a mechanism for activation/deactivation of the propagating species that resembles most CRP schemes in our simulations. We will demonstrate that even

in “truly living” polymerizations, confining the growing chains (either by grafting to the surface or by collapsing the chains in poor solvents) may result in appreciable increases in the PDI of the surface-tethered polymers. We also explore the effect of confinement due to chain collapse on the MWDs. Our motivation for investigating polymerization in poor solvents comes from experimental studies in which methanol/water/monomer mixtures were used for SI-ATRP of methyl methacrylate (MMA)<sup>19,35</sup> and n-isopropylacrylamide (NIPAAm)<sup>36-40</sup> from planar substrates. If large monomer concentration gradients develop in these reactions, they can expose the grafted polymers to a water/methanol mixture, which is a poor solvent at the experimental conditions.

### **4.3. Simulation Model**

Computer simulations of CRP reactions are performed by implementing a stochastic MC algorithm<sup>34</sup> in conjunction with the BFM.<sup>41</sup> The polymers and monomers reside in a three dimensional cubic lattice in which the monomers can be bonded according to the following vector families: P(2,0,0), P(2,1,0), P(2,1,1), P(2,2,1), P(3,0,0) and P(3,1,0).<sup>42</sup> These vector sets prevent any bonds from crossing and monomers (and polymers) from overlapping as long as the only allowed moves in the simulation are nearest neighbor ones. The fluctuating character of the bond-lengths in this model allows for close approximation of

continuum behavior while at the same time preserving the advantages of lattice models such as integer arithmetic.

The BFM is, by its nature, self-avoiding and as such it describes polymer behavior under good solvent conditions. In order to simulate poor solvent conditions we have incorporated a set of inter-molecular, intra-molecular and bond-length potentials.<sup>43</sup> The first potential is of the Lennard-Jones (LJ) form and is truncated to only act between beads that find themselves within the maximum distance allowed by the above mentioned vector families (bond length =  $10^{1/2}$ ). A bond-length potential is also included in order to describe the increase in chain stiffness with decreasing temperature. In our system, the LJ and bond-length potentials only act between bonded beads in the simulation box and not between the beads representing free monomers. We neglect the polymer-monomer and monomer-monomer interactions in order to prevent aggregation of free monomers that would describe an unlikely physical condition in which the monomers are not soluble in the polymerization medium. It was demonstrated previously that increasing the interaction parameter ( $\epsilon$ ) in these potentials relative to temperature leads to collapsed chain conformations.<sup>43,44</sup> We confirm independently chain collapse in the bulk- and surface-initiated cases (c.f. **Appendix C**) and perform reactive simulations in both good ( $\epsilon = 4 \times 10^{-7} k_B T$ ) and poor ( $\epsilon = 4 \times 10^{-1} k_B T$ ) solvents.

**Table 4.1.** Lattice dimensions and the corresponding values of  $\sigma$ .

$L_x = L_y$	$L_z$	Lattice Volume	$\sigma$
160	39	998400	0.06
140	51	999600	0.08
120	69	993600	0.11
100	100	1000000	0.16
80	156	998400	0.25
60	278	1000800	0.44

The MC algorithm used to simulate the polymerization reactions has been described previously<sup>34</sup> (c.f. **Appendix D**). The total number of initiators and monomers is fixed for all simulations performed. We vary the density of initiators on the surface while maintaining nearly constant overall volume of the lattice by adjusting the dimensions of the cubic lattice ( $L_x = L_y, L_z$ ). In this manner, we can investigate the effect of the grafting density of initiators on the polymerization while keeping other relevant parameters (*i.e.*, monomer concentration) unchanged. **Table 1** shows the  $L_x = L_y$  and the  $L_z$  dimensions of the lattices used in this study and the resulting surface density of the initiators ( $\sigma$ , where  $\sigma = 1$  represents a fully covered surface in the BFM). In bulk-initiated polymerizations, we implement periodic boundary conditions in the three spatial directions. For surface-initiated polymerizations two impenetrable walls are located at  $z = 0$  and  $z = L_z$  representing the substrate and the limit of the simulation box, respectively; the periodic boundary conditions are employed only in the  $xy$  plane of the lattice.

The initial configuration for bulk-initiated polymerizations corresponds to the monomers and initiators distributed uniformly throughout the volume of the simulation box. Each initiator corresponds to two bonded polymer beads, of which one is a propagating center (i.e., chain-end). In the case of surface-initiated polymerizations the inactive bead of the initiator is located at equally spaced intervals on the substrate and at  $z = 1$  while the propagating bead is placed directly above of the anchoring bead at  $z = 3$ . In the surface-initiated case, the bead adjacent directly to the surface is not movable. The numbers of monomers and initiators have been fixed at  $M_0 = 12500$  and  $I_0 = 400$ , respectively; this corresponds to a lattice occupancy of 10.64%. We perform a preliminary long equilibration run consisting of  $\approx 10^9$  attempted Monte Carlo steps (MCS, defined as MC steps per simulation bead) to obtain a randomly-distributed configuration. The equilibrated configuration serves as input to the MC simulations.

We initialize the simulations by a short equilibration period of  $10^6$  MCS. This is equivalent to every bead in the simulation box undergoing 75 attempted moves. Once the second pre-equilibration finishes the reactive MC algorithm commences. The reactive MC scheme continues until either 80% of the monomer is exhausted (i.e., polymerized) or a predetermined maximum number of MCS elapses. The latter premature end of the simulations before reaching high

conversions was necessary because in the high surface density and poor solvent regimes probed, the polymerization rate is very slow and the simulation would not reach 80% conversion in a reasonable time.

The MC algorithm implemented here is similar to our previous work<sup>34</sup> except for a few changes that we describe next. Previously, the probability of reaction versus motion was set a priori to  $P_r = 0.5$ . In the current work, we investigate the effect of this parameter on the results of the simulation and determine that, for the study of different levels of confinement and poor solvent conditions, a more appropriate value of  $P_r$  is 0.01 (see **Appendix C**). Reducing the reaction rate (propagation only in the present work since we prohibit termination and chain transfer) further assures controlled polymerization growth, which is consistent with the approach of Liu and coworkers. Reducing  $P_r$  also shifts the system behavior from a diffusion-limited reaction to a kinetically limited one, in turn, mitigating the effects of gradients in the free monomer volume fraction and allowing the polymer chains to approach their equilibrium conformations. Although it would be desirable to slow the reaction rate enough to achieve full kinetic control, balancing this need with feasible simulation times was required. The second difference between the current simulations and our previous work is that the probability to add a monomer ( $P_a$ ) is no longer proportional ( $P_a = P_{a,0}[M/M_0]$ , where  $P_{a,0}$  is a constant and  $M$  is the instantaneous

number of free monomers) to the number of free monomers left in the simulation box. This proportionality was redundant because the probability that an active chain and a free monomer approach to within the reactive distance is already proportional to the instantaneous monomer concentration. We therefore modify our approach in the current work and set  $P_a = P_{a,o}$  throughout the simulation run. Both these changes affect the observed results in an absolute fashion but all the observed trends and conclusions of our previous work<sup>34</sup> remain unchanged in this revision of the algorithm.

During a typical polymerization run, we monitor the monomer conversion ( $x_m$ ), polydispersity index (PDI), radius of gyration ( $|R_g^2|^{1/2}$ ), volume fraction profiles ( $\varphi_i(z)$ ) and the number of nearest neighbor site per active chain-end occupied by monomers ( $\theta_m$ ), polymers ( $\theta_p$ ) and chain-ends ( $\theta_e$ ). We evaluate the PDI,  $R_g$ , and  $\varphi_i(z)$  at steps of 1% monomer conversion. We average these quantities for at least three independent runs in order to gain statistical certainty. The number of the nearest neighbors to the active chain-ends are computed every 10000 MCSs and plotted as a function of monomer conversion. These data are fitted with a third degree polynomial in order to discern the trends between the different runs.

## 4.4. Results and Discussion

### 4.4.1. Solvent quality

Computer simulations of polymerization reactions were performed in good and poor solvents for bulk-initiated systems. The working hypothesis was that with decreasing the solvent quality, the coil becomes more compact thus making the interior of the coil inaccessible to monomers and hiding the growing chain inside the collapsed coil. As a result, relative to polymerization under good solvent conditions, the rate of polymerization under poor solvent conditions will be slower and the PDI will increase. **Figure 4.1** depicts the evolution of the  $|R_g^2|^{1/2}$  (a) and PDI (b) as a function of monomer conversion for polymerizations performed in good (blue squares) and poor (red circles) solvent conditions. Compared to polymers grown in good solvents, under poor solvent conditions the resulting macromolecules possess smaller dimensions for identical average molecular weights (conversions). Moreover, the PDI of polymers grown under poor solvent conditions increases at higher conversions relative to the good solvent case.

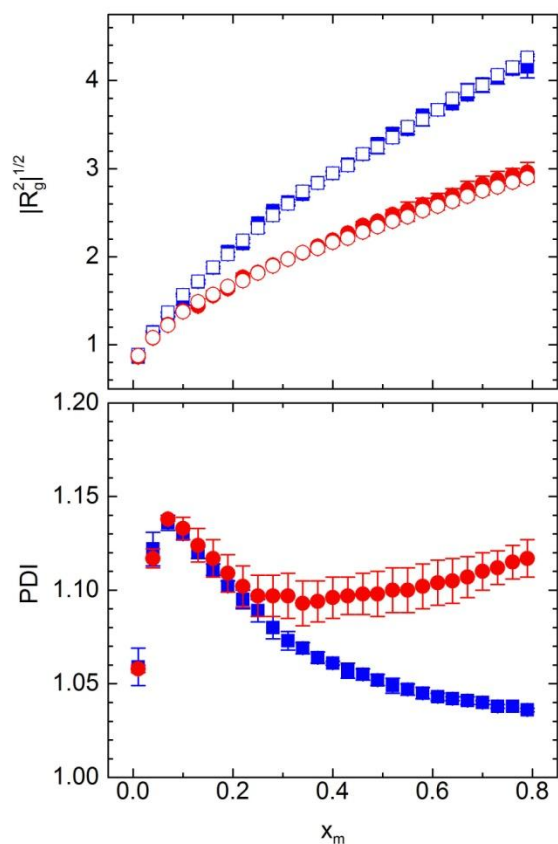


**Figure 4.1.** a) Radius of gyration and b) polydispersity index of bulk polymers in good (blue squares,  $\epsilon = 4 \times 10^{-7} k_B T$ ) and poor (red circles,  $\epsilon = 4 \times 10^{-1} k_B T$ ) solvent conditions as a function of monomer conversion.

While these observations confirm that chain collapse under poor solvent conditions and the resulting confinement of the propagating centers lead to broader MWDs, in order to gain insight into the reasons for this broadening we have to monitor the environment around the propagating chain-ends. Specifically, every 10000 MCSs we determine the number of nearest neighbor site per active chain-end occupied by monomers ( $\theta_m$ ), polymer beads belonging

to the observed chain-end ( $\theta_{p,s}$ ) or to other chains ( $\theta_{p,o}$ ), and the remaining empty sites ( $\theta_e$ ). We least-square fit these data to facilitate the identification of differences between good and poor solvent conditions (**Figure 4.2**). In contrast to polymerization under good solvent conditions, in poor solvents there is a lower likelihood that an active chain-end will encounter a monomer and undergo reaction as reflected by the data for  $\theta_m$ . Concurrently,  $\theta_{p,s}$  and  $\theta_{p,o}$  increase in going from good to poor solvent conditions. The increase in  $\theta_{p,s}$  indicates that the chains are collapsing and that chain-ends are more likely to neighbor other beads in the same chain. The increase in  $\theta_{p,o}$  suggests that the chains tend to aggregate in poor solvent conditions thus further shielding the active chain-ends and hindering the polymerization reaction. Both of these effects can disrupt monomer delivery to the chain-ends, which can explain the decreased rate of polymerization (not shown) and the increase in PDI. One explanation for the increase in PDI that we cannot currently verify is that each chain might collapse with its chain-end located farther or closer to the interphase between the collapsed globule and the solution. The dynamics of a collapsed chain are slow enough that the chain will not change its configuration significantly throughout the polymerization. This would result in uneven growth of chains depending on the specific collapse configuration.

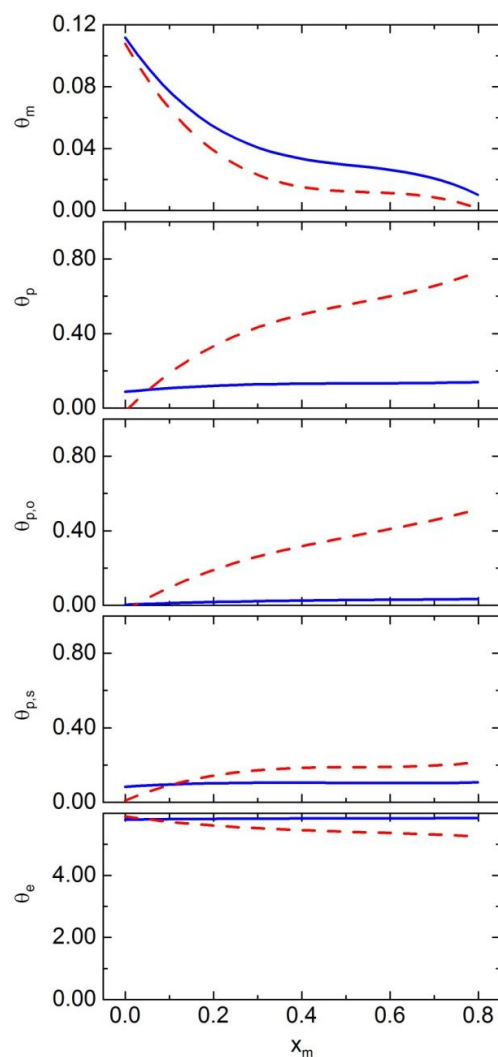


**Figure 4.2.** Average number of nearest neighbor sites per active end occupied by free monomers ( $\theta_m$ ), polymers ( $\theta_p$ ), polymers belonging to a different chain ( $\theta_{p,o}$ ), polymer belonging to the observed chain ( $\theta_{p,s}$ ) and the remaining empty sites ( $\theta_e$ ) for bulk polymerization under good (solid,  $\varepsilon = 4 \times 10^{-7} k_B T$ ) and poor (dashed,  $\varepsilon = 4 \times 10^{-1} k_B T$ ) solvent conditions.

While the aforementioned observations are specific to our model reaction, they provide insight into the factors influencing a real system. Take for example, ATRP reactions, in which a terminal halogen atom can transfer reversibly to a neighboring metal/organic ligand complex protecting and de-protecting the

chains.<sup>45</sup> In this case, not only will the collapse of the chain obstruct the monomer from reaching the reaction centers but it will also hinder the metal/organic ligand complex and the catalyst crucial for the reaction. One can therefore envision situations in which collapsed polymers do not alternate efficiently between the active (living) and inactive (dormant) forms resulting in deterioration of reaction control. Many other factors may come into play under poor solvent conditions (*i.e.*, altered halogen transfer between the metal/ligand complex and the growing chain) and in this sense, our simulations are a simplified scenario providing insight into the factors affecting polymerization control in poor solvents.

#### 4.4.2. *Surface Density*

Computer simulations of polymerizations were performed with bulk and surface-bound initiators under good and poor solvent conditions. Our benchmark system corresponds to a lattice defined by  $L_x = L_y = L_z = 100$  with the initial number of monomers equal to 12500 and number of initiators equal to 400. In the surface-initiated polymerization, this corresponds to  $\sigma = 0.16$ . We also explore how varying  $\sigma$  affects the polymerization reaction. While a logical way to change  $\sigma$  would seem to be to add more initiators to the surface, this approach would alter the ratio between numbers of monomers and initiators,

which would consequently influence the kinetics and PDI of the reaction. In order to achieve different values of  $\sigma$  without changing the numbers of monomers and initiators one should thus modify the dimensions of the lattice to vary the area per initiator molecule while keeping the total volume of the lattice approximately constant. Given that  $L_z$  varies for simulations at different  $\sigma$ , all runs are inspected to insure that the perpendicular component of the radius of gyration ( $|R_{g,\perp}^2|^{1/2}$ ) does not approach  $L_z$ .

**Figure 4.3** shows the parallel ( $|R_{g,\parallel}^2|^{1/2}$ ) and perpendicular ( $|R_{g,\perp}^2|^{1/2}$ ) components of the radius of gyration as a function of the monomer conversion for bulk- (dashed line) and surface-initiated (symbols) systems under good (left column) and poor (right column) solvent conditions at three different  $\sigma$  equal to 0.08 (top), 0.16 (middle), and 0.44 (bottom). We must note that the averages computed here are not ensemble averages for configurations of a single chain but the averages of the instantaneous configurations of a population of chains with varying degrees of polymerization ( $N$ ). Bulk polymers exhibit equal dimensions in every direction because of orientational averaging over many configurations and are therefore represented by a single line. The average size of the bulk-initiated polymers increases with increasing conversion; the increase is

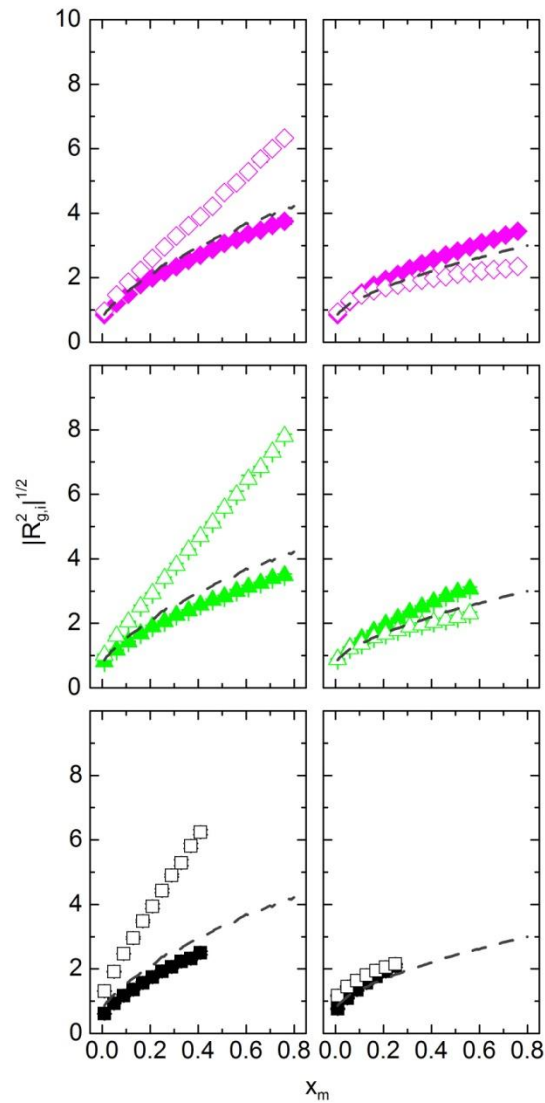


**Figure 4.3.** Parallel ( $R_{g,\parallel}$ , closed symbols) and perpendicular ( $R_{g,\perp}$ , open symbols) components of the average radius of gyration of grafted chains as a function of monomer conversion for good (left column,  $\epsilon = 4 \times 10^{-7} k_B T$ ) and poor (right column,  $\epsilon = 4 \times 10^{-1} k_B T$ ) solvent conditions at three different grafting densities ( $\sigma$ ): 0.08 (top row, magenta), 0.16 (middle row, green) and 0.44 (bottom row, black). The dashed lines represent corresponding data for chains polymerized in bulk.

slower in poor solvents relative to good solvents, as noted previously. Surface-initiated polymers in good solvents exhibit larger dimensions in the direction perpendicular to the substrate than parallel to it; this effect becomes more pronounced with increases in  $\sigma$ . This shape asymmetry is due to repulsive excluded volume interactions between neighboring chains, which force the polymers to extend away from the tethering surface. Most of the shape asymmetry manifests itself as an increase in  $|R_{g,\perp}^2|^{1/2}$  while  $|R_{g,\parallel}^2|^{1/2}$  undergoes only a small decrease from its bulk value. Under poor solvent conditions and at low  $\sigma$ ,  $|R_{g,\perp}^2|^{1/2}$  becomes smaller than  $|R_{g,\parallel}^2|^{1/2}$ . With increasing  $\sigma$  the difference between  $|R_{g,\perp}^2|^{1/2}$  and  $|R_{g,\parallel}^2|^{1/2}$  vanishes and eventually  $|R_{g,\perp}^2|^{1/2} > |R_{g,\parallel}^2|^{1/2}$ . These observations reveal that under poor solvent conditions the chains try to minimize their contact with the solvent. At low grafting densities, they achieve this by collapsing onto the substrate and stretching towards their neighbors. At higher grafting densities, the horizontal confinement increases and the only direction the chains can extend to is that perpendicular to the substrate.

In an ideal system, one would want all initiator molecules to activate simultaneously so that the propagation reaction commences instantaneously for all growing polymers. In reality, not all initiators are activated at the same time (or activated at all).<sup>19</sup> There are multiple reasons for this behavior. Some of them

are associated with the chemical nature of the initiator and the environmental trigger that activates it (typical examples include azo-based initiators for free radical polymerizations<sup>46-48</sup>) or with steric hindrance of the initiator molecules in confined systems. Since the properties, particularly the PDI, of the polymeric tethers depend crucially on the initiator efficacy, it is important to monitor the fraction of active initiators that participate in the reaction. Although such a task is challenging to carry out experimentally, computer simulations can handle monitoring this parameter very easily. In **Figure 4.4**, we plot the fraction of initiators that undergo polymerization as a function of monomer conversion ( $x_m$ ). For nearly all values of  $\sigma$ , complete (*i.e.*, 100%) initiation efficiency is achieved by  $x_m = 0.20$ . The sole exceptions are systems with very high grafting density where the initiator efficiency plateaus earlier,  $\sigma \geq 0.44$  in good solvents and  $\sigma \geq 0.25$  in poor solvents. In poor solvent conditions and at the highest  $\sigma$ , the initiator efficiency reaches a plateau value of 0.8, which might have implications for polymerization of real systems if large gradients in monomer concentration develop (*i.e.*, methacrylates in water/alcohol mixtures).<sup>19,35</sup>

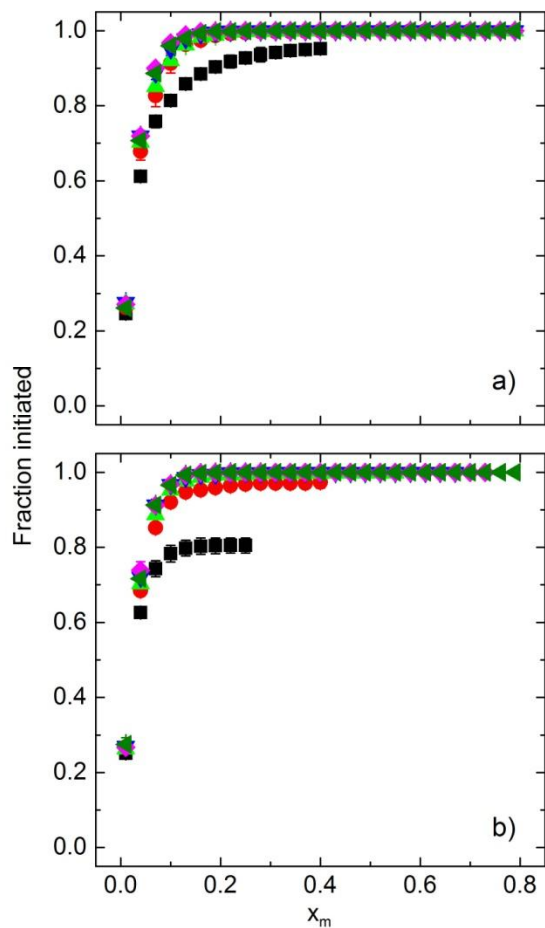


**Figure 4.4.** Initiator efficiency as a function of monomer conversion for a) good ( $\epsilon = 4 \times 10^{-7} k_B T$ ) and b) poor ( $\epsilon = 4 \times 10^{-1} k_B T$ ) solvent conditions at various grafting densities ( $\sigma$ ): 0.06 ( $\blacktriangleleft$ ), 0.08 ( $\blacklozenge$ ), 0.11 ( $\blacktriangledown$ ), 0.16 ( $\blacktriangleup$ ), 0.25 ( $\bullet$ ), and 0.44 ( $\blacksquare$ ).

One of the main benefits of computer simulations applied to polymerization is that one can determine the MWD of the grown polymers *in situ*. Although SEC experiments are in principle capable of providing similar information, the amount of material cleaved off from the substrate is often below the sensitivity limit of most SEC detectors. Furthermore, even if SEC traces show a polymer

peak, they might miss (or skew) low and high molecular weight tails, leading to underestimation of the broadness of the distribution. Computer simulations overcome this limitation by calculating the MWD from the size ( $N$ ) of each chain. The data in **Figure 4.5** represent MWDs as a function of  $x_m$  and  $\sigma$  for good (left column) and poor (right column) solvent conditions. The values in the ordinate represent conversions and the black lines represent slices of the MWDs at the labeled conversions. While relatively narrow peaks represent the MWDs at low  $\sigma$ , at high  $\sigma$  a high molecular weight tail develops. Going from  $\sigma = 0.08$  (top) to  $\sigma = 0.44$  (bottom) the MWD broadens significantly. Although at low  $\sigma$  the peak moves steadily to larger molecular weight areas, at high  $\sigma$  most of the chains remain short. Polymerizations under poor solvents exacerbate these effects possibly due to chain collapse and obstruction of the access of monomers to chain-ends.

To quantify the broadness of the MWDs at different  $\sigma$  and different solvent conditions we monitor the PDI of the surface-initiated chains as function of  $x_m$  and plot the results in **Figure 4.6**. We compute the PDI, defined as the ratio of the mass-average molar mass (second moment) to the number-average molar mass (first moment) of the distribution, by taking into account the length of all chains including those of initiators that have not yet polymerized ( $N = 2$ ). In good solvents (**Figure 4.6a**) and at low  $\sigma$  the reaction remains controlled; very

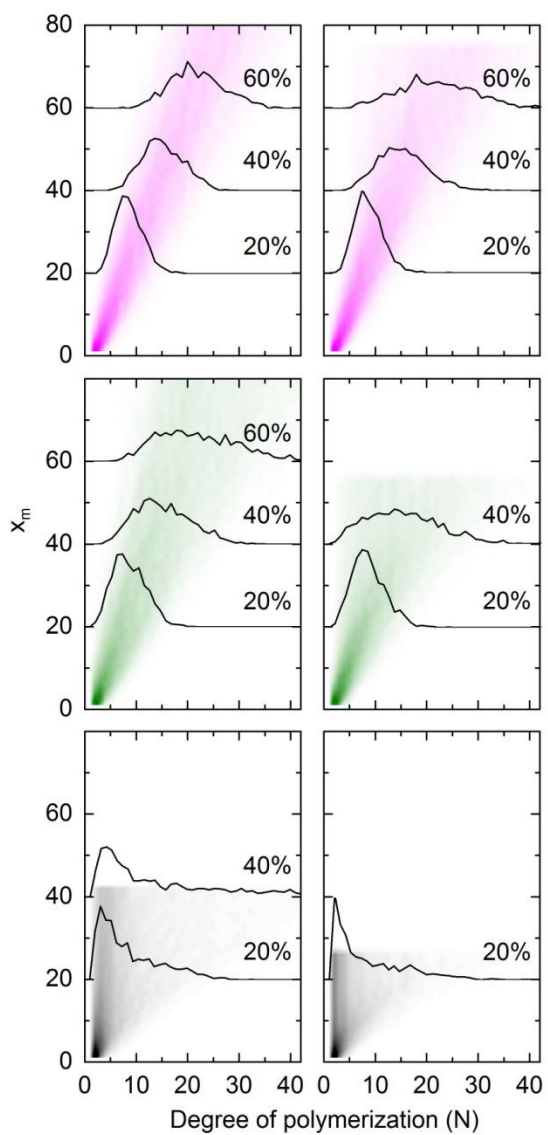


**Figure 4.5.** Chain length distributions for surface initiated polymerizations as a function of monomer conversion ( $x_m$ , ordinate) for good (left column,  $\epsilon = 4 \times 10^{-7} k_B T$ ) and poor (right column,  $\epsilon = 4 \times 10^{-1} k_B T$ ) solvent conditions at three grafting densities ( $\sigma$ ): 0.08 (top, magenta), 0.16 (middle, green) and 0.44 (bottom, black). The dark areas represent high frequency of a specific chain length and light colors low frequency. The lines represent slices of these distributions and their ordinate value represent the frequency at a given chain length.

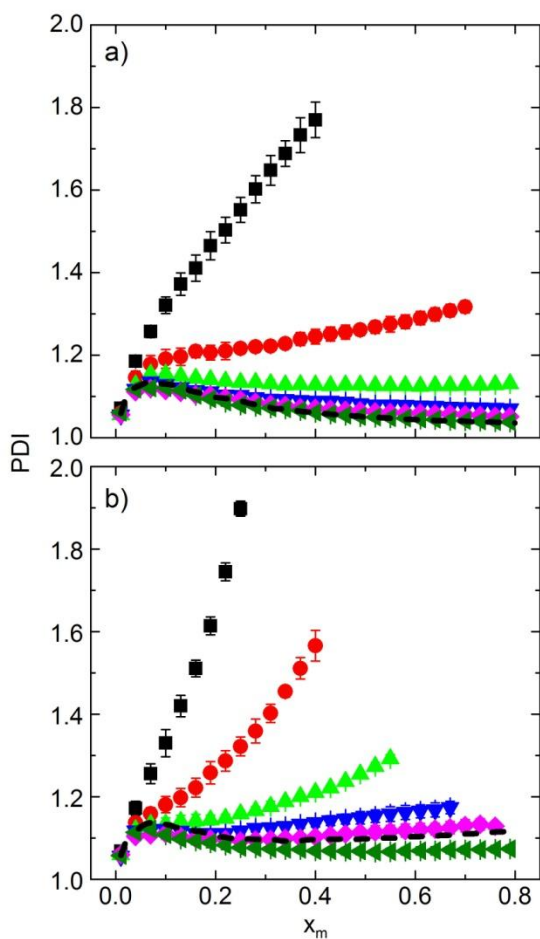


**Figure 4.6.** Polydispersity index (PDI) of grafted chains as a function of monomer conversion for good (a,  $\epsilon = 4 \times 10^{-7} k_B T$ ) and poor (b,  $\epsilon = 4 \times 10^{-1} k_B T$ ) solvent conditions at various grafting densities ( $\sigma$ ): 0.06 ( $\blacktriangleleft$ ), 0.08 ( $\blacklozenge$ ), 0.11 ( $\blacktriangledown$ ), 0.16 ( $\blacktriangle$ ), 0.25 ( $\bullet$ ), and 0.44 ( $\blacksquare$ ). The dotted black lines represent the PDI values for chains polymerized in bulk.

low PDI values are attainable at all monomer conversions. Furthermore, the PDIs for low  $\sigma$  are identical to those obtained for bulk polymerizations (dashed line).

This indicates polymerizations from surfaces populated sparsely with initiators may achieve similar control as the bulk-initiated CRP (we caution that some

differences between the two polymerization geometries may still exist in real systems even at low  $\sigma$  because effects not considered in this model, such as mobility of the metal/organic ligand complex in the activation reaction, etc). Increasing  $\sigma$  leads to higher PDI values indicating that polymers grown from dense initiator assemblies have broader MWDs. Given that chain termination is neglected, the monomer concentration is unchanged and all the relevant kinetic parameters of the model are constant we attribute this gradual increase in PDI to the increase in initiator density on the surface and therefore to chain crowding. This observation is consistent with previous experimental studies<sup>15,16,18,19</sup> and the work in Liu et al.,<sup>32</sup> which report higher PDIs for surface grown polymers relative to polymers grown in solution.

Computer simulations performed under poor solvent conditions yield similar trends as those observed in good solvents. However, we observe pronounced increases in the PDI with increasing monomer conversion, especially at high  $\sigma$  (**Figure 4.6b**). At  $\sigma = 0.08$  we detect an increase of  $\approx 5\%$  in the PDI at the maximum conversion achieved ( $x_m = 0.8$ ) in going from good to poor solvent condition; this value increases to 26% ( $x_m = 0.27$ ) at  $\sigma = 0.44$ . Overall, there are synergistic effects when both high  $\sigma$  and poor solvent conditions are present that result in very poor control of polymerization reactions. In addition, for the bulk-initiated systems, the increase in PDI when

going from good to poor solvent conditions is  $\approx 7.8\%$ , which is larger than the value at  $\sigma = 0.08$ . Polymers grown at  $\sigma = 0.08$  and under poor solvent conditions represent the only case, in which we observe a lower PDI for grafted chains relative to those in the bulk. A possible explanation for this behavior is that although bulk chains can readily form aggregates through intermolecular interactions, tethered chains cannot diffuse to one another because of their attachment to the surface. The latter prevents chain aggregation and therefore reduces the chain-end confinement on the surface when compared to the bulk.

In order to explain the increases in PDIs as a function of  $\sigma$  we recur to the average occupation of the nearest neighbor sites of the active chain-ends. In **Figure 4.7** we plot  $\theta_m$ ,  $\theta_p$  and the fraction of surface sites near the chain-ends ( $\theta_w$ ) as a function of  $x_m$  for polymerizations performed under good (left column) and poor (right column) solvent conditions at three  $\sigma$  values: 0.08 (top), 0.16 (middle), and 0.44 (bottom). We observe that with increasing monomer conversion  $\theta_m$  decreases due to monomer consumption,  $\theta_p$  increases due to the higher molar mass of polymers and  $\theta_w$  decreases due to the chain-ends moving farther away from the surface. At the lowest  $\sigma$ , the initial value of  $\theta_m$  ( $x_m = 0$ ) is about half that of the bulk-initiated case and it decreases further at higher values of  $\sigma$ . We attribute this behavior to the presence of the substrate and to the increased crowding of the initiators at higher  $\sigma$ . As the polymerization

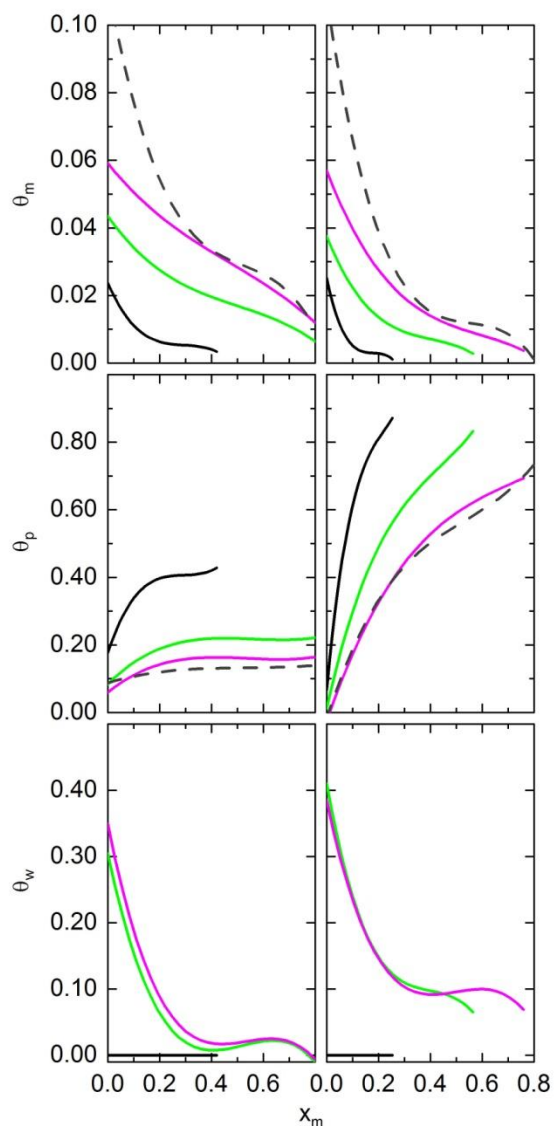


**Figure 4.7.** Average number of nearest neighbor sites per active end occupied by monomers ( $\theta_m$ , top row), polymers ( $\theta_p$ , middle row), wall ( $\theta_w$ , bottom row) as a function of monomer conversion for good (left column,  $\epsilon = 4 \times 10^{-7} k_B T$ ) and poor (right column,  $\epsilon = 4 \times 10^{-1} k_B T$ ) solvent conditions. The solid lines represent values corresponding to various grafting densities: 0.08 (magenta), 0.16 (green), and 0.44 (black). The dark grey dashed lines represent the corresponding values for chains polymerized in bulk.

progresses and the chain-ends migrate away from the substrate (at about  $x_m = 0.31$ ),  $\theta_m$  for the low  $\sigma$  case and the bulk-initiated case become equal indicating similar environments of the active chain-ends in these systems. Further,  $\theta_p$  increases with increasing  $\sigma$  indicating that the polymers are occupying the space near the active chain-ends and blocking their access to free monomer. Under poor solvent conditions (right column), this effect is more pronounced suggesting that chain collapse leads to additional masking of the active chain-ends by the polymer and additional disruption of the chain-ends access to monomer. Finally,  $\theta_w$  decreases as a function of  $x_m$  except for the largest  $\sigma$  in which its value is zero for all  $x_m$ . When  $\sigma = 0.44$  the initiators almost fully cover the surface and within the BFM it is impossible for macromolecules growing under such conditions to access the sites adjacent to the wall.

In order to comprehend the increases in PDI as  $\sigma$  increases we construct volume fraction profiles of the polymers ( $\varphi_p(z)$ , left column), free monomers ( $\varphi_m(z)$ , center column) and chain-ends ( $\varphi_e(z)$ , right column) as a function of distance from the substrate ( $z$ , abscissa) and  $x_m$  (ordinate) for good (**Figure 4.8**) and poor (**Figure 4.9**) solvents. As previously, the data in the top, middle, and bottom rows correspond to  $\sigma$  equal to 0.08, 0.16, and 0.44, respectively. The colored areas correspond to high concentrations while the white color denotes zero concentration. The black lines represent sample slices of the  $\varphi_i(z)$  at a

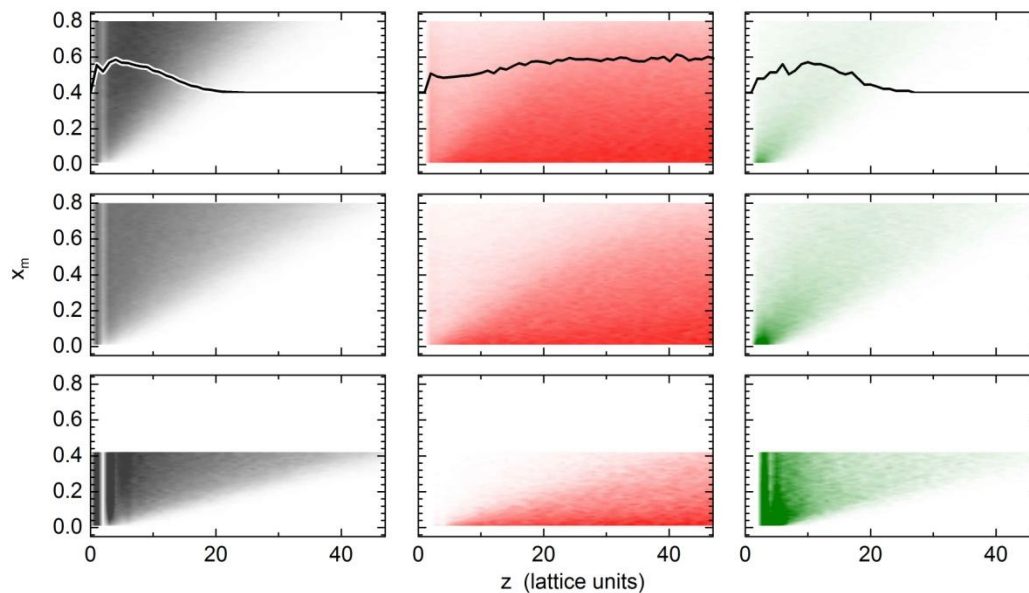


**Figure 4.8.** Volume fraction of grafted chains (left column, black), monomers (middle column, red), and chain-ends (right column, green) expressed as a function of the distance from the wall (abscissa,  $z$ ) vs. monomer conversion (ordinate,  $x_m$ ) under good ( $\epsilon = 4 \times 10^{-7} k_B T$ ) solvent conditions at three grafting densities: 0.08 (top row), 0.16 (middle row), and 0.44 (bottom row).

specific  $x_m$ . In general,  $\phi_p(z)$  and  $\phi_e(z)$  extend away from the surface with increasing  $x_m$ , as expected. In addition,  $\phi_m(z)$  develops a depletion layer near the substrate as  $x_m$  increases indicating that within the polymer brush the concentration of monomer decreases appreciably. As  $\sigma$  increases, the monomer depletion continues to develop and reaches a point where the populations of chain-ends and monomers no longer overlap. In more detail, **Figure 4.10** shows  $\phi_p(z)$ ,  $\phi_m(z)$  and  $\phi_e(z)$  on the same scale at three different  $\sigma$ ,  $x_m = 0.2$  and at good (left column) and poor (right column) solvent conditions. At  $\sigma = 0.08$  (top)  $\phi_m(z)$

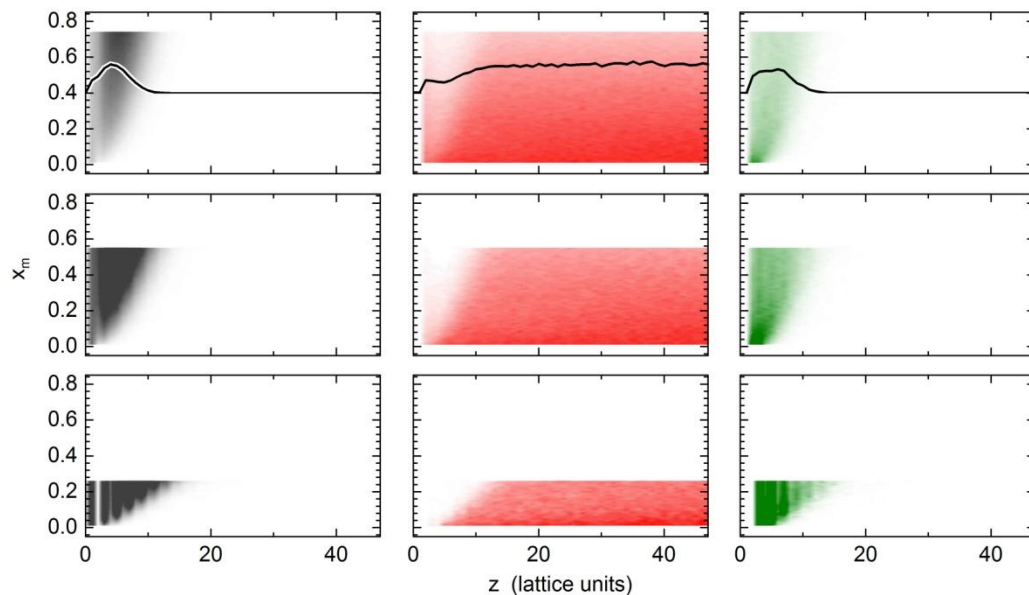


**Figure 4.9.** Volume fraction of grafted chains (left column, black), monomers (middle column, red), and chain-ends (right column, green) expressed as a function of the monomer conversion ( $x_m$ ) vs. the distance from the wall ( $z$ ) under poor ( $\epsilon = 4 \times 10^{-1} k_B T$ ) solvent conditions at three grafting densities: 0.08 (top row), 0.16 (middle row), and 0.44 (bottom row).

remains almost constant even very close to the surface; there is appreciable overlap between the free monomer and chain-end populations. At  $\sigma = 0.16$  (middle)  $\phi_m(z)$  undergoes a steeper decrease near the substrate and in poor solvents it is very close to zero. Finally, at  $\sigma = 0.44$  (bottom)  $\phi_m(z)$  reaches zero farther away from the substrate under both good and poor solvent conditions. The populations of chain-ends and free monomers have minimal overlap leading to uneven growth in the high  $\sigma$  case. We therefore conclude that at higher  $\sigma$  any differences in the chain-lengths of the polymers lead to preferential growth of

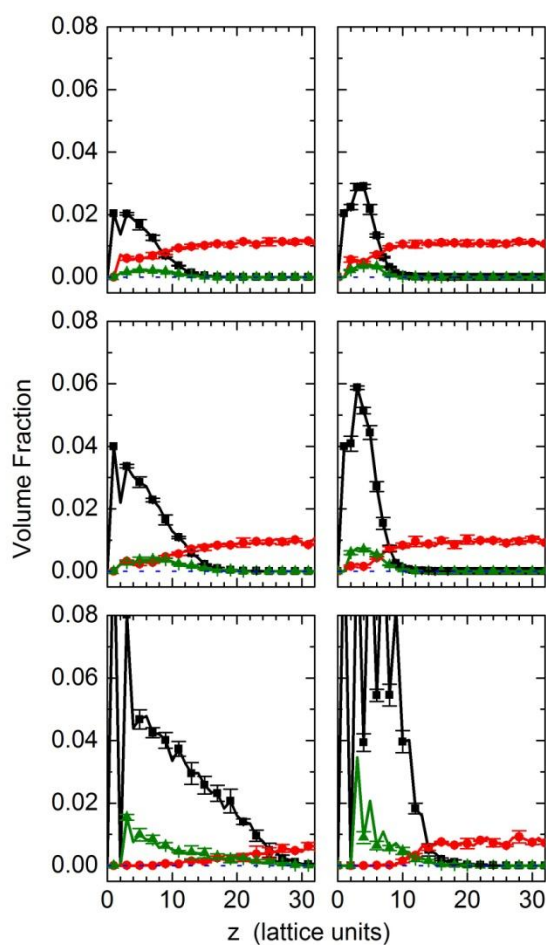


**Figure 4.10.** Volume fraction profiles of grafted chains (■), monomers (●), and chain-ends (▲) for good (left column,  $\epsilon = 4 \times 10^{-7} k_B T$ ) and poor (right column,  $\epsilon = 4 \times 10^{-1} k_B T$ ) solvent conditions at three grafting densities: 0.08 (top row), 0.16 (middle row), and 0.44 (bottom row).

the longer chains versus the shorter ones, a situation that is detrimental to the controlled growth of macromolecules from surfaces.

As alluded to above, properties such as the brush height and the volume fraction profile of the polymers and chain-ends depend on the broadness of the MWDs. A brief exploration of these differences can be seen in **Figure 4.11**, which

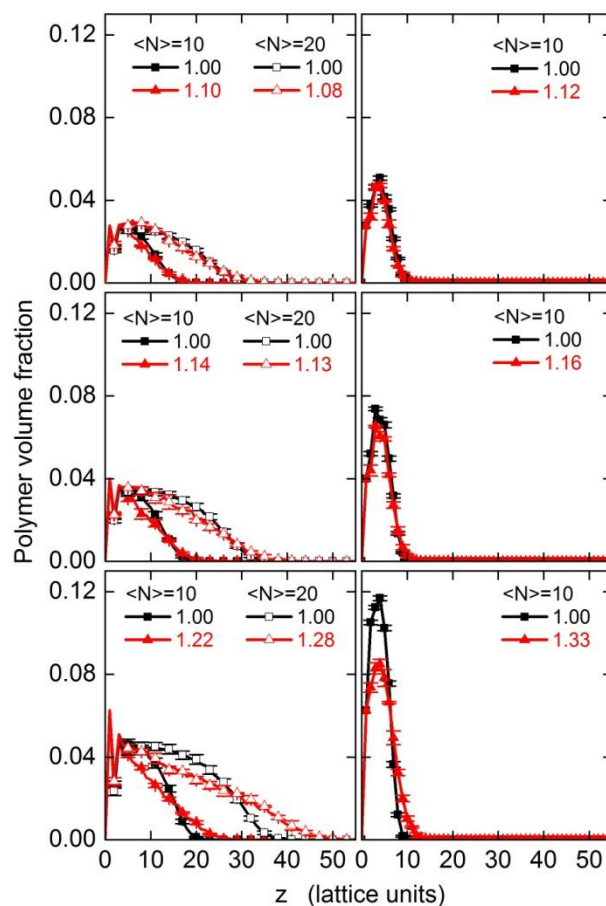


**Figure 4.11.** Volume fraction profiles for monodisperse (squares) and polydisperse (triangles, PDI listed in the legend) for good (left column,  $\epsilon = 4 \times 10^{-7} k_B T$ ) and poor (right column,  $\epsilon = 4 \times 10^{-1} k_B T$ ) solvents at three grafting densities: 0.11 (top row), 0.16 (middle row) and 0.25 (bottom row). Profiles were obtained at  $x_m$  values of 0.26 and 0.58 for  $N$  equal to 10.1 and 20.1 respectively.

shows  $\varphi_p(z)$  for grafted layers created by our reactive simulation (up-triangles) and those with PDI = 1 (squares). Samples with  $N = 10.0$  (10.1 for polydisperse system) correspond to  $x_m = 0.26$  and for  $N = 20.0$  (20.1 for polydisperse system) correspond to  $x_m = 0.58$ . As  $\sigma$  increases from 0.11 (top) to 0.25 (bottom) the PDI

of the synthesized layers grows from 1.10 to 1.22, respectively, at  $N = 10$ . Although at  $\sigma = 0.11$  the monodisperse and polydisperse concentration profiles are nearly identical, there are substantial differences at  $\sigma = 0.25$ . Relative to the monodisperse layers, the polydisperse ones exhibit lower  $\varphi_p(z)$  close to the substrate but extend farther away from it indicating larger thicknesses. In general, this effect is more notable as the PDI increases and it can be observed for the chains in poor solvents as well.

de Vos and Leermakers recently published a detailed account of the effect of chain length polydispersity on characteristics of end-tethered polymers.<sup>29</sup> They used a numerical self-consistent field model to calculate concentration profiles of brushes that had bimodal and continuous distributions (the latter was assumed to follow the Schulz–Zimm distribution). The authors reported that for both distributions studied, increases in PDI of the brushes in good solvents result in changes in the shape of the concentration profiles from parabolic to linear to concave. They also noted that the average height of the brush increased with increasing PDI; for instance, an increase of PDI from 1.0 to 1.1 resulted in a 12% increase in brush height. de Vos and Leermakers noted that in polydisperse brushes chain-ends segregate depending on the molecular weight of the chain as opposed to the monodisperse case, in which the locations of the chain-ends fluctuate strongly through the entire thickness of the grafted layer. Our

**Table 4.2.** Degrees of polymerization ( $N$ ) and polydispersity indices (PDI) compared to those obtained by fitting the Schulz-Zimm distribution to the simulation data at several  $\sigma$  and both solvent conditions.

Solvent conditions	$\sigma$	Direct calculation		Fit to Schulz-Zimm distribution		
		$\langle N \rangle$	PDI	$\langle N \rangle$	PDI	$R^2$
good <sup>a)</sup>	0.08	14.5	1.07	15.1	1.11	0.96
good <sup>a)</sup>	0.16	14.5	1.13	15.2	1.13	0.91
good <sup>a)</sup>	0.44	14.5	1.76	10.0	1.76	0.87
poor <sup>b)</sup>	0.08	10.4	1.10	10.8	1.09	0.94
poor <sup>b)</sup>	0.16	10.4	1.16	11.2	1.16	0.91
poor <sup>b)</sup>	0.44	10.4	2.00	3.56	1.62	0.90

a)  $\varepsilon = 4 \times 10^{-7} k_B T$ ,  $x_m = 0.40$

b)  $\varepsilon = 4 \times 10^{-1} k_B T$ ,  $x_m = 0.27$

simulations allow us to generate populations of chains grown directly from the surface and determine if the Schulz-Zimm distribution describes correctly these populations. **Table 4.2** shows the least-squared fitted parameters of the Schulz-Zimm distribution to data for several of our grafted polymer populations. Although the Schulz-Zimm distribution describes the populations at  $\sigma = 0.08$  and  $\sigma = 0.16$  well, at  $\sigma = 0.44$  the quality of the fit deteriorates. Moreover, the values obtained for the PDI and  $N$  in the high  $\sigma$  fits deviate from the true values for these populations. We posit that the Schulz-Zimm distribution fails to describe the chain-length distribution at high  $\sigma$  because the chains are no longer growing with equal probability, *i.e.*, small chains have a lower probability of growth than larger ones. We can also verify independently the conclusions reached by de Vos and Leermakers without assuming any a priori form of the distribution of chain lengths. First, regardless of solvent quality, increasing  $\sigma$

leads to higher PDI and higher brush heights. Second, polydisperse brushes in good solvents are more extended than are those in poor solvents, the latter exhibit larger increases in PDI relative to systems under good solvent conditions. Third, for a given combination of solvent quality,  $\sigma$ , and  $N$ , a crossover point exists where all volume fraction profiles intersect regardless of the PDI. This observation was also made by de Vos and Leermakers but not discussed in their paper. We will provide a detailed discussion of this effect in a subsequent publication.<sup>49</sup>

#### **4.5. Conclusions**

We employed Monte Carlo simulations to investigate the effect that grafting density and solvent quality on surface-initiated living polymerizations. Our computer simulations neglected terminations and chain-transfer while incorporating an idealized mechanism for activation and deactivation of the growing chains. We have shown that even under such “true living” conditions “grafting from” polymerization from planar impenetrable substrates results in broadened of molecular weight distributions relative to bulk-initiated polymerizations and that this broadening increases as the grafting density of initiators increases. We attribute this broadening at high grafting densities to the uneven access to free monomers for short and long chains occasioned by the

depletion of free monomer close to the substrate. In addition, the PDI of both bulk- and surface-initiated polymers produced by CRP increased with decreasing solvent quality. This behavior has been attributed to the collapsed conformation of the coil and possible chain aggregates that confine the growing chain-end and limit the access of free monomers to the growing end. The combination of poor solvent conditions and high grafting densities further exacerbates the broadening of the molecular weight distribution. For instance, relative to good solvent conditions, low grafting density systems ( $\sigma = 0.08$ ) underwent an increase in PDI of 5% under poor solvent conditions. This number increased to 26% at the highest grafting density ( $\sigma = 0.44$ ) studied. We also showed that, although the Schulz–Zimm distribution describes correctly the chain-length probability density of surface-initiated polymers at small and moderate grafting densities, at high grafting densities ( $\sigma = 0.44$ ) the description is no longer valid. We attribute the latter behavior to the difference in the probability of short (low) and long (high) chains to grow which is a direct result of the separation of the monomer and chain-end populations under these conditions.

Although the effect of initiator density and solvent quality on surface-initiated CRP is clear, additional work is needed to understand the process of living polymerization from surfaces in detail and perhaps a in a more realistic manner. One important aspect we have ignored in this work is that solvent

quality will depend on the monomer concentration. The interaction energies used in this study could in principle be a function of the distance away from the substrate and depend on the local monomer concentration. This adjustment would resemble experimental conditions more closely. Experimentally, one works with large excess of monomer and stops the reaction in its early stages in order to keep the PDI relatively low. Computer simulations describing such situations should be developed; this would effectively mean switching from the NVT simulation system to one that considers a constant chemical potential of free monomers in the bulk. A more thorough study is necessary to explore the validity of the Schulz–Zimm distribution for layers polymerized to higher average degree of polymerization and to check for a cross-over degree of polymerization at which the Schulz–Zimm distribution ceases to be valid. The effect of the substrate curvature on the molecular weight (MW) and PDI should also be extended beyond flat surfaces and compared to similar systems polymerized in bulk. In particular, it would be interesting to explore whether strong confinement of chains polymerized from surfaces with negative curvature (*i.e.*, concave surfaces) leads to increases in PDI and decreases in MW. Living polymerization from surfaces with positive curvature (*i.e.*, convex) should also be considered. Here the effect expected is the opposite to polymerization in concave spaces. Specifically, with increasing the positive curvature, the polymers

grown from surface should start to resemble their counterparts polymerized in solution. While the effect of confinement is, in general, relatively trivial to imagine, it is difficult to provide numerical data about the combined effect of curvature, initiator density, and solvent quality. This is where computer simulations will come very handy.

#### 4.6. References

1. Barb y, R.; Lavanant, L.; Paripovic, D.; Sch wer, N.; Sugnaux, C.; Tugulu, S.; Klok, H. Polymer Brushes Via Surface-Initiated Controlled Radical Polymerization: Synthesis, Characterization, Properties, and Applications. *Chem. Rev.* **2009**, *109*, 5437-5527.
2. Chen, T.; Chang, D. P.; Zauscher, S. Fabrication of Patterned Polymer Brushes on Chemically Active Surfaces by in Situ Hydrogen-Bond-Mediated Attachment of an Initiator. *Small* **2010**, *6*, 1504-1508.
3. Gautrot, J. E.; Trappmann, B.; Oceguela-Yanez, F.; Connelly, J.; He, X.; Watt, F. M.; Huck, W. T. S. Exploiting the Superior Protein Resistance of Polymer Brushes to Control Single Cell Adhesion and Polarisation at the Micron Scale. *Biomaterials* **2010**, *31*, 5030-5041.
4. Lavanant, L.; Pullin, B.; Hubbell, J. A.; Klok, H. A Facile Strategy for the Modification of Polyethylene Substrates with Non-Fouling, Bioactive Poly(Poly(Ethylene Glycol) Methacrylate) Brushes. *Macromol. Biosci.* **2010**, *10*, 101-108.
5. Moglianetti, M.; Webster, J. R. P.; Edmondson, S.; Armes, S. P.; Titmuss, S. Neutron Reflectivity Study of the Structure of pH-Responsive Polymer Brushes Grown from a Macroinitiator at the Sapphire-Water Interface. *Langmuir* **2010**, *26*, 12684-12689.

6. Ohno, K.; Kayama, Y.; Ladmiral, V.; Fukuda, T.; Tsujii, Y. A Versatile Method of Initiator Fixation for Surface-Initiated Living Radical Polymerization on Polymeric Substrates. *Macromolecules* **2010**, *43*, 5569-5574.
7. Riachi, C.; Schuwer, N.; Klok, H. Degradable Polymer Brushes Prepared Via Surface-Initiated Controlled Radical Polymerization. *Macromolecules* **2009**, *42*, 8076-8081.
8. Takahashi, H.; Nakayama, M.; Yamato, M.; Okano, T. Controlled Chain Length and Graft Density of Thermoresponsive Polymer Brushes for Optimizing Cell Sheet Harvest. *Biomacromolecules* **2010**, *11*, 1991-1999.
9. Ye, Q.; Wang, X.; Li, S.; Zhou, F. Surface-Initiated Ring-Opening Metathesis Polymerization of Pentadecafluorooctyl-5-Norbornene-2-Carboxylate from Variable Substrates Modified with Sticky Biomimic Initiator. *Macromolecules* **2010**, *43*, 5554-5560.
10. Tsujii, Y.; Ohno, K.; Yamamoto, S.; Goto, A. Structure and Properties of High-Density Polymer Brushes Prepared by Surface-Initiated Living Radical Polymerization. *Adv. Polym. Sci.* **2006**, *197*, 1-45.
11. Goto, A.; Fukuda, T. Kinetics of Living Radical Polymerization. *Prog. Polym. Sci.* **2004**, *29*, 329-385.
12. Braunecker, W. A.; Matyjaszewski, K. Controlled/living Radical Polymerization: Features, Developments, and Perspectives. *Prog. Polym. Sci.* **2007**, *32*, 93-146.
13. Matyjaszewski, K.; Miller, P. J.; Shukla, N.; Immaraporn, B.; Gelman, A.; Luokala, B. B.; Siclovan, T. M.; Kickelbick, G.; Vallant, T.; Hoffmann, H.; Pakula, T. Polymers at Interfaces: Using Atom Transfer Radical Polymerization in the Controlled Growth of Homopolymers and Block Copolymers from Silicon Surfaces in the Absence of Untethered Sacrificial Initiator. *Macromolecules* **1999**, *32*, 8716-8724.
14. Matyjaszewski, K.; Dong, H.; Jakubowski, W.; Pietrasik, J.; Kusumo, A. Grafting from Surfaces for "Everyone": ARGET ATRP in the Presence of Air. *Langmuir* **2007**, *23*, 4528-4531.

15. Gorman, C. B.; Petrie, R. J.; Genzer, J. Effect of Substrate Geometry on Polymer Molecular Weight and Polydispersity during Surface-Initiated Polymerization. *Macromolecules* **2008**, *41*, 4856-4865.
16. Pasetto, P.; Blas, H.; Audouin, F.; Boissière, C.; Sanchez, C.; Save, M.; Charleux, B. Mechanistic Insight into Surface-Initiated Polymerization of Methyl Methacrylate and Styrene Via ATRP from Ordered Mesoporous Silica Particles. *Macromolecules* **2009**, *42*, 5983-5995.
17. Kruk, M.; Dufour, B.; Celer, E. B.; Kowalewski, T.; Jaroniec, M.; Matyjaszewski, K. Grafting Monodisperse Polymer Chains from Concave Surfaces of Ordered Mesoporous Silicas. *Macromolecules* **2008**, *41*, 8584-8591.
18. Koylu, D.; Carter, K. R. Stimuli-Responsive Surfaces Utilizing Cleavable Polymer Brush Layers. *Macromolecules* **2009**, *42*, 8655-8660.
19. Jones, D. M.; Brown, A. A.; Huck, W. T. S. Surface-Initiated Polymerizations in Aqueous Media: Effect of Initiator Density. *Langmuir* **2002**, *18*, 1265-1269.
20. Milner, S. T. Compressing Polymer «Brushes»: A Quantitative Comparison of Theory and Experiment. *Europhys. Lett.* **1988**, *7*, 695-699.
21. Milner, S. T.; Witten, T. A.; Cates, M. E. Effects of Polydispersity in the End-Grafted Polymer Brush. *Macromolecules* **1989**, *22*, 853-861.
22. Chakrabarti, A.; Toral, R. Density Profile of Terminally Anchored Polymer Chains: A Monte Carlo Study. *Macromolecules* **1990**, *23*, 2016-2021.
23. Klushin, L. I.; Skvortsov, A. M. Chain Behavior in a Polydisperse Brush: Depression of Critical Fluctuations. *Macromolecules* **1992**, *25*, 3443-3448.
24. Lai, P.; Zhulina, E. B. Structure of a Bidisperse Polymer Brush: Monte Carlo Simulation and Self-Consistent Field Results. *Macromolecules* **1992**, *25*, 5201-5207.
25. Dhoot, S.; Watanabe, H.; Tirrell, M. Measurement of Forces in Interactions between Bimodal Layers of Diblock Copolymer Adsorbed on Mica. *Colloids Surf., A* **1994**, *86*, 47-60.

26. Laub, C. F.; Koberstein, J. T. Effect of Brush Polydispersity on the Interphase between End-Grafted Brushes and Polymeric Matrixes. *Macromolecules* **1994**, *27*, 5016-5023.
27. Kritikos, G.; Terzis, A. F. Structure of Bimodal and Polydisperse Polymer Brushes in a Good Solvent Studied by Numerical Mean Field Theory. *Polymer* **2005**, *46*, 8355-8365.
28. Kritikos, G.; Terzis, A. F. Theoretical Study of Polymer Brushes by a New Numerical Mean Field Theory. *Polymer* **2007**, *48*, 638-651.
29. de Vos, W.; Leermakers, F. Modeling the Structure of a Polydisperse Polymer Brush. *Polymer* **2009**, *50*, 305-316.
30. de Vos, W. M.; Leermakers, F. A. M.; de Keizer, A.; Kleijn, J. M.; Cohen Stuart, M. A. Interaction of Particles with a Polydisperse Brush: A Self-Consistent-Field Analysis. *Macromolecules* **2009**, *42*, 5881-5891.
31. Wittmer, J. P.; Cates, M. E.; Johner, A.; Turner, M. S. Diffusive Growth of a Polymer Layer by in Situ Polymerization. *Europhys. Lett.* **1996**, *33*, 397-402.
32. Milchev, A.; Wittmer, J. P.; Landau, D. P. Formation and Equilibrium Properties of Living Polymer Brushes. *J. Chem. Phys.* **2000**, *112*, 1606-1615.
33. Liu, H.; Li, M.; Lu, Z.; Zhang, Z.; Sun, C. Influence of Surface-Initiated Polymerization Rate and Initiator Density on the Properties of Polymer Brushes. *Macromolecules* **2009**, *42*, 2863-2872.
34. Genzer, J. In Silico Polymerization: Computer Simulation of Controlled Radical Polymerization in Bulk and on Flat Surfaces. *Macromolecules* **2006**, *39*, 7157-7169.
35. Jones, D. M.; Huck, W. T. S. Controlled Surface-Initiated Polymerizations in Aqueous Media. *Adv. Mater.* **2001**, *13*, 1256-1259.
36. Schild, H. G.; Muthukumar, M.; Tirrell, D. A. Cononsolvency in Mixed Aqueous-Solutions of Poly(n-Isopropylacrylamide). *Macromolecules* **1991**, *24*, 948-952.

37. Jones, D. M.; Smith, J. R.; Huck, W. T. S.; Alexander, C. Variable Adhesion of Micropatterned Thermoresponsive Polymer Brushes: AFM Investigations of Poly(*N*-Isopropylacrylamide) Brushes Prepared by Surface-Initiated Polymerizations. *Adv. Mater.* **2002**, *14*, 1130-1134.
38. Farhan, T.; Huck, W. T. S. Synthesis of Patterned Polymer Brushes from Flexible Polymeric Films. *Eur. Polym. J.* **2004**, *40*, 1599-1604.
39. Liu, G.; Zhang, G. Reentrant Behavior of Poly(*N*-Isopropylacrylamide) Brushes in Water-Methanol Mixtures Investigated with a Quartz Crystal Microbalance. *Langmuir* **2005**, *21*, 2086-2090.
40. Jhon, Y. K.; Bhat, R. R.; Jeong, C.; Rojas, O. J.; Szleifer, I.; Genzer, J. Salt-Induced Depression of Lower Critical Solution Temperature in a Surface-Grafted Neutral Thermoresponsive Polymer. *Macromol. Rapid Commun.* **2006**, *27*, 697-701.
41. Carmesin, I.; Kremer, K. The Bond Fluctuation Method: A New Effective Algorithm for the Dynamics of Polymers in all Spatial Dimensions. *Macromolecules* **1988**, *21*, 2819-2823.
42. Deutsch, H. P.; Binder, K. Interdiffusion and Self-Diffusion in Polymer Mixtures: A Monte Carlo Study. *J. Chem. Phys.* **1991**, *94*, 2294-2304.
43. Wittkop, M.; Kreitmeier, S.; Göritz, D. The Collapse Transition of a Single Polymer Chain in Two and Three Dimensions: A Monte Carlo Study. *J. Chem. Phys.* **1996**, *104*, 3373-3385.
44. Semler, J. J.; Genzer, J. Design of Random Copolymers with Statistically Controlled Monomer Sequence Distributions Via Monte Carlo Simulations. *J. Chem. Phys.* **2006**, *125*, 014902.
45. Matyjaszewski, K.; Xia, J. H. Atom Transfer Radical Polymerization. *Chem. Rev.* **2001**, *101*, 2921-2990.
46. Prucker, O.; Rühle, J. Mechanism of Radical Chain Polymerizations Initiated by Azo Compounds Covalently Bound to the Surface of Spherical Particles. *Macromolecules* **1998**, *31*, 602-613.

47. Prucker, O.; Rhe, J. Synthesis of Poly(Styrene) Monolayers Attached to High Surface Area Silica Gels through Self-Assembled Monolayers of Azo Initiators. *Macromolecules* **1998**, *31*, 592-601.
48. Prucker, O.; Rhe, J. Polymer Layers through Self-Assembled Monolayers of Initiators. *Langmuir* **1998**, *14*, 6893-6898.

## CHAPTER 5

### COMPUTER SIMULATION OF SIMULTANEOUS BULK- AND SURFACE-INITIATED CONTROLLED RADICAL POLYMERIZATION

#### 5.1. Introduction

In **Chapter 4**, we discussed the reasons for the differences in the broadness of the molecular weight distribution (MWD) between polymers initiated on the surface and those grown in bulk. In this Chapter, we investigate the case of simultaneous polymerization of surface- and bulk-initiated polymers and their competition for the available free monomers in bulk solution. Our principal objective is to understand the effect this competition has on the molecular weights and MWDs of both populations of polymers. To achieve this goal we explore a parameter space that includes the initiator grafting density ( $\sigma$ ), fraction of polymers on the surface ( $\eta$ ), and the initial number of free monomers in the simulation box ( $M_0$ ).

The motivation for our study originates from experiments with polymer brushes on planar impenetrable surfaces.<sup>1,2</sup> In order to provide information

about the grafting density and molecular weight of the surface-grown polymers, one typically conducts simultaneous polymerization initiated both on the surface and in the bulk. The molecular weight ( $\langle N \rangle_B$ ) and the polydispersity index (PDI) of the bulk-initiated polymers are determined by means of size exclusion chromatography. By assuming that both bulk- and surface-initiated polymers grow with similar rates, one can write  $\langle N \rangle_S \approx \langle N \rangle_B$  and can then convert conveniently the dry thickness ( $h$ ) of the surface polymers into the grafting density of the chains ( $\sigma$ ) on the surface:

$$\sigma = \frac{h\rho N_a}{\langle N \rangle_S}, \quad (5.1)$$

where  $\rho$  is the density of the polymer and  $N_a$  is Avogadro's number. The objective of this work is to determine the validity of the  $\langle N \rangle_S \approx \langle N \rangle_B$  assumption. Moreover, we plan to compare the molecular weight distributions of the two classes of macromolecules.

The synthesis of surface-grafted polymers is often accomplished by controlled radical polymerization (CRP) methods.<sup>1,3-13</sup> Within this class of reactions, atom transfer radical polymerization (ATRP) is probably the most widely used.<sup>2,14</sup> The widespread use of CRP schemes is due to their compatibility with an extensive library of monomers, the living character of the reaction (allowing the creation of block copolymers), insensitivity to impurities

(compared to free radical or ionic polymerization techniques), the ability to control the average molecular weight (and thickness in the case of surface initiation), and the ability to obtain polymers with low PDI. In the context of CRP, the presence of free initiators in solution can have an effect on the intrinsic growth kinetics of the surface polymers. Surface reactions, especially those from planar substrates, produce very small amounts of the deactivating species (i.e.  $\text{CuX}_2$  in ATRP where  $\text{X} = \text{Cl}$  or  $\text{Br}$ ) leading to loss of control due to excessive terminations at the early stages of the polymerization. Sacrificial (free) initiators added to the bulk solution increase the concentration of the deactivating species thus restoring control to the reaction.<sup>2,8,15</sup> A second way in which free initiators may affect the growth of surface bound initiators is by competing with the surface-bound polymers for the available monomers. Therefore, the possibility that surface and bulk grown polymers differ in their polymerization rates may lead to different molecular weights as well as PDIs of these two populations of polymers. Such a difference precludes the application of Equation 5.1 for the characterization of the grafted polymer layers because the assumption that  $\langle N \rangle_S \approx \langle N \rangle_B$  is no longer valid. This study focuses on investigating the competition between polymers grown in bulk and those initiated simultaneously from flat surfaces and the associated effects on the molecular weight distributions of both classes of macromolecules (i.e., bulk- and surface-initiated).

We neglect any effects that the presence of bulk initiators may have on the activation/deactivation and on the buildup of deactivating species since we incorporate these processes in our simulations implicitly. This is to say that the polymerizations herein studied remain controlled in terms of their kinetics and the value of  $\eta$  has no effect on the intrinsic kinetics of the polymerization process. In addition, we assume that bulk and surface polymers have equal probabilities of undergoing activation and deactivation reactions.

## 5.2. Simulation Model and Algorithm

We investigate the effects of  $M_0$ ,  $\eta$ , and  $\sigma$  on the simultaneous polymerization of bulk and surface-bound polymers. The initial number of total initiators (combined bulk and surface) remains constant ( $I_0 = 400$ ). By setting  $\eta$ , we therefore fix the number of both bulk and surface polymers. It is our objective to investigate the independent effects of  $\sigma$  and  $\eta$  on the MWDs of both populations of polymers. In order to vary  $\sigma$  and  $\eta$  independently we alter the dimensions of the lattice in the lateral ( $L_X = L_Y$ ) and vertical ( $L_Z$ ) dimensions independently while keeping the volume of the lattice at  $\approx 5 \times 10^5$  lattice units. In order to vary  $\sigma$ , the procedure for resizing the lattice described in **Chapter 4** has been employed.<sup>16</sup> Additional variations in the lattice sizes were needed when keeping  $\sigma$  constant while varying  $\eta$ . We resize the lateral dimensions of the

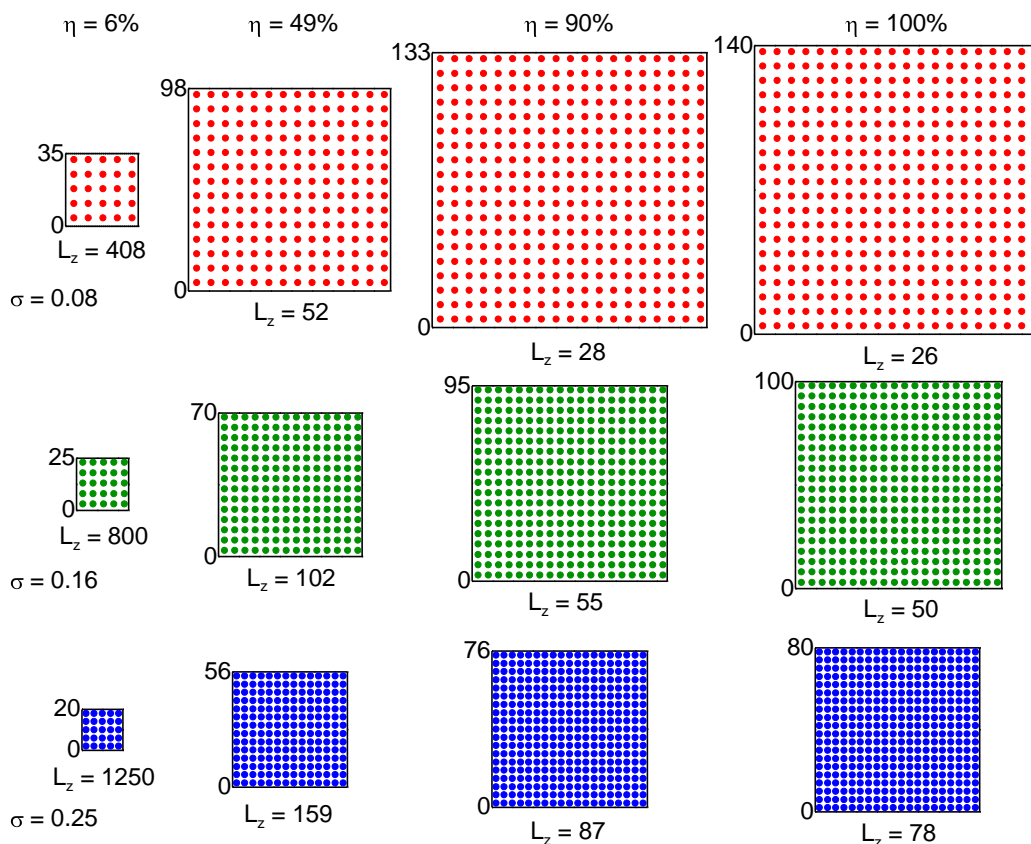


**Figure 5.1.** Top view of the lattices used in this study for various  $\sigma$  and  $\eta$ . The dots indicate the positions of the grafting points on the surface.

lattice as the number of polymers on the surface varies to maintain a constant  $\sigma$ . We also vary  $M_0$  in order to explore the effects of free monomer density on polymerization. Altering the latter parameter would reveal any possible effects associated with diffusion limitation during the course of the polymerization reaction. **Figure 5.1** depicts pictorially the surfaces (i.e., the x-y plane at  $L_z = 0$ ) of various lattices corresponding to various  $\sigma$  and  $\eta$  investigated and the positions of the initiator sites on the surfaces. Some of the lattices investigated have large

**Table 5.1.** Parameters adjusted in order to change  $M_0$  correctly.

<b>Mo</b>	<b>Beads</b>	<b>Pr</b>	<b>Moves</b>	<b>LT</b>	<b>NRLT</b>
6250	7050	0.0187	52	535	19
12500	13300	0.0100	99	1000	10
25000	25800	0.0052	192	1930	5

aspect ratios, which might confine the polymers and affect the polymerizations. To verify that the large lattice aspect ratio does not affect the properties of the growing polymers we compare the PDIs of bulk polymers ( $\eta = 0\%$ ) grown in lattices with low and high aspect ratios as a function of conversion and number average molecular weight and determined that they were equivalent.

The implementation of our simulation protocols with varying values of  $M_0$  requires adjustments to the parameters affecting the reaction kinetics (**Table 5.1**). The parameters requiring adjustment are the probability of reaction versus motion ( $P_r$ ) and the lifetime of active polymers (LT). If we increase the initial number of free monomers in the simulation while keeping  $P_r$  constant, there will be, on average, a lower fraction of total beads attempting to move between attempted reaction steps. This is equivalent to a change in the relative rates of reaction and motion, an undesirable consequence of a simple increase in  $M_0$ . We therefore adjust  $P_r$  depending on the value of  $M_0$  in order to keep the relative rates of reactions and motions constant. For instance, if  $M_0$  equals 12500 and  $P_r = 0.01$  there will be on average 99 attempted motions for every attempted reaction, which corresponds to 0.74% of the beads attempting a

move. In contrast, for  $P_r = 0.01$  and  $M_o = 25000$  0.38% of the beads would undergo motion. To take this into account, we use the  $M_o = 12500$  simulations as a benchmark and adjust  $P_r$  for the  $M_o$  equal 6250 and 25000 systems in order to maintain the fraction of beads attempting a move between attempted reactions equal to 0.74% (cf. **Table 5.1**). The value of  $LT$  also affects the kinetics of the simulated reaction. If  $P_r$  adjustments are needed to account for the varying number of beads, then  $LT$  corrections are necessary to account for the changes in  $P_r$ . As  $P_r$  is varied, the average number of reactions occurring within a living polymer cycle varies proportionally. For instance, if  $P_r$  equals 0.01 or 0.10 and  $LT = 1000$  there will be on average 10 or 100 attempted reactions, respectively, every living cycle. Kinetic theories of CRP reactions have shown that the number of propagations per living cycle is an important parameter in the CRP scheme and that it can have significant effects on the molecular weight distribution of the resulting polymers.<sup>17</sup> Adjustments in  $P_r$  and  $LT$  are therefore needed to compare systems with different  $M_o$ .

The initial configurations for the simulations consist of an equidistant array of initiators on the flat surface (cf. **Figure 5.1**). The bulk initiators and free monomers are distributed regularly throughout the lattice. Each initiator corresponds to two joined beads of which one is an initiating site that can undergo initiation if approached by a monomer. We pre-equilibrate the

configurations thus constructed for at least  $1 \times 10^5$  attempted MC moves per bead yielding a random spatial distribution of free initiators and monomers on the lattice. The randomly distributed configurations serve as an input to the reactive simulations. To mimic “living” polymerization conditions we disable completely terminations and chain transfer reactions in the simulations. We note, however, that subroutines for termination and chain transfer reactions have been implemented in our code and exploration of their effects on the behavior of our system is possible (work currently in progress). We obtain averages of the number average molecular weights and the PDIs by repeating each simulation 5 times and sampling the system at regular values of the free monomer conversion ( $x_m$ ). Prior to the initialization of the reactive MC algorithm, we perform a final short equilibration consisting of  $1 \times 10^6$  attempted MC moves. The reactive MC scheme then begins and continues until either 80% of the free monomer is exhausted (*i.e.*, polymerized) or a predetermined maximum number of MCS elapses. In a few instances, the distance between the substrate and the opposing impenetrable wall ( $L_z$ ) for some of the lattices in Table 1 is very small. To prevent interaction of the tethered polymers with the opposite wall, it is necessary to truncate some of the datasets as shown in **Table 5.2**.

**Table 5.2.** Datasets truncated to avoid interaction with opposing substrate.  $\text{Max}(x_m)$  denotes value of  $x_m$  at which truncation occurred. Datasets not displayed were not truncated.

$\sigma$	$\eta$ (%)	$M_o \times 10^{-3}$	$\text{Max}(x_m)$
0.08	90	6.25	0.60
		12.5	0.40
		25.0	0.25
	100	6.25	0.60
		12.5	0.40
		25.0	0.25
0.16	90	25.0	0.60
	100	12.5	0.70
		25.0	0.50
0.25	90	25.0	0.70
	100	25.0	0.55

### 5.3. Results and Discussion

To elucidate the effects of simultaneous polymerizations of surface and bulk polymers as a function of  $\eta$  and  $\sigma$ , we monitor the average molar weight as a function of  $x_m$  at  $M_o = 25000$  for bulk and surface polymers independently (**Figure 5.2**). The average molecular weight of bulk-grown polymers increases linearly at  $\eta = 6\%$ , as one would expect from polymerizations, in which only bulk or surface polymers are grown ( $\eta = 0\%$  or  $100\%$ , black dashed lines). As  $\eta$  increases from  $6\%$  to  $90\%$ ,  $\langle N \rangle_B$  becomes larger than expected at a particular value of  $x_m$ . The deviation for  $\sigma = 0.08$  is very small indicating that polymers growing sparsely from surfaces grow at a similar pace to their bulk counterparts.

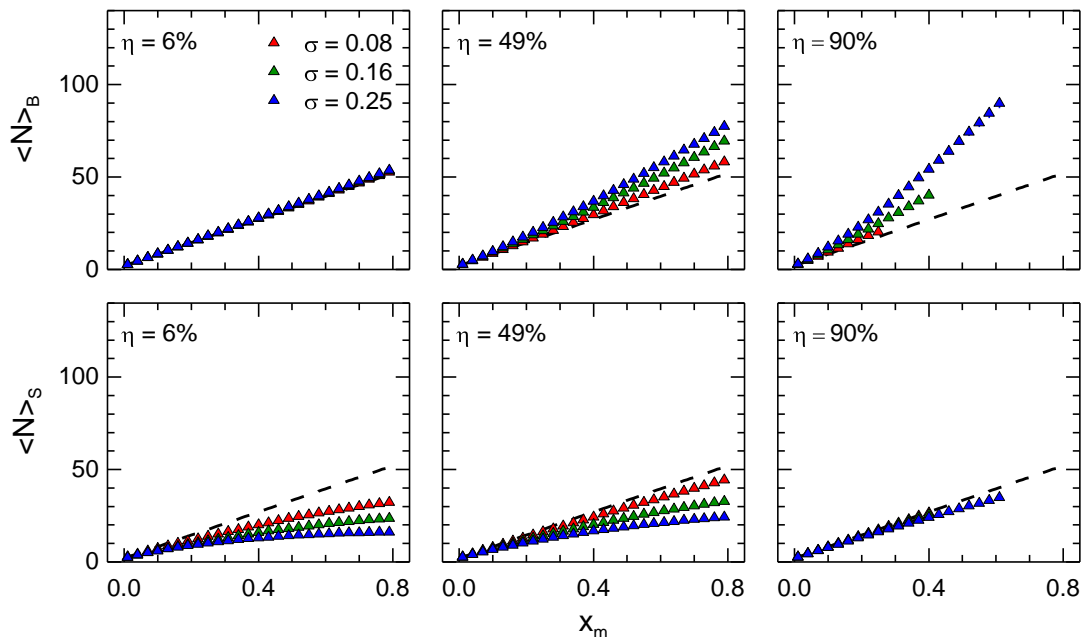


**Figure 5.2.** Average molecular weight for bulk (top row) and surface (bottom row) polymers as a function of monomer conversion with initial number of monomers ( $M_0$ ) of 25000; percentages of surface polymers ( $\eta$ ): 6% (left column), 49% (middle column) and 90% (right column); grafting densities of initiators ( $\sigma$ ): 0.08 (red), 0.16 (green) and 0.25 (blue). The black dashed lines represent the  $\eta = 100\%$  and  $M_0 = 25000$  conditions. The  $\eta = 90\%$  data is truncated because the brush starts interacting with the opposite impenetrable surface.

The deviation from the  $\eta = 0\%$  line increases when  $\sigma$  increases from 0.08 to 0.25, indicating that the surface-bound initiators affect the properties of the bulk-grown polymers under these conditions. Namely, increasing the density of surface-bound initiators increases the molecular weight of the bulk-grown polymers. The surface polymers exhibit the opposite trend. Here we observe that the data lie below the black line indicating shorter polymers than when only surface polymers are grown ( $\eta = 100\%$ ). For the surface-grown polymers, the deviation between the  $\eta = 90\%$  and  $\eta = 100\%$  cases is very small, but as  $\eta$

decreases from 90% to 6%, the deviation becomes larger indicating that at low  $\eta$  the polymers initiating from the surface grow at a slower pace than the bulk-initiated macromolecules. Increasing  $\sigma$  tends to enlarge the deviation from the  $\eta = 100\%$  line suggesting that the larger the  $\sigma$  the slower the pace of surface growth. Furthermore, at  $\eta = 6\%$  and  $\sigma = 0.25$ ,  $\langle N \rangle_s$  reaches a plateau at approximately  $x_m = 0.6$  indicating that depending on  $\sigma$  and  $\eta$  the presence of the bulk polymers might cap the growth of the surface bound layer. This observation is consistent with many experimental studies, in which the thickness of the polymer layer reaches a plateau value at long polymerization times.<sup>18</sup> The presence of this plateau is attributed typically to excessive terminations at the beginning of the reaction thus decreasing the propagating radicals on the surface. This explanation alone, however, cannot hold true in our simulations due to the lack of termination reactions. We thus suggest that in addition to the effect of termination, the plateau in  $\langle N \rangle_s$  can be attributed (in part) to 1) the competition between the bulk- and surface-initiated macroinitiators (i.e., growing chains) for free monomers and 2) the slower polymerization rate from the surface-initiated sites that in turn depends on the degree of confinement of the surface-grown macromolecule. Comparisons of  $\langle N \rangle_B$  and  $\langle N \rangle_s$  reveal one of the most important findings of this study. Specifically, at a particular monomer conversion  $\langle N \rangle_B - \langle N \rangle_s = \delta > 0$ . The magnitude of  $\delta$  depends on the combination

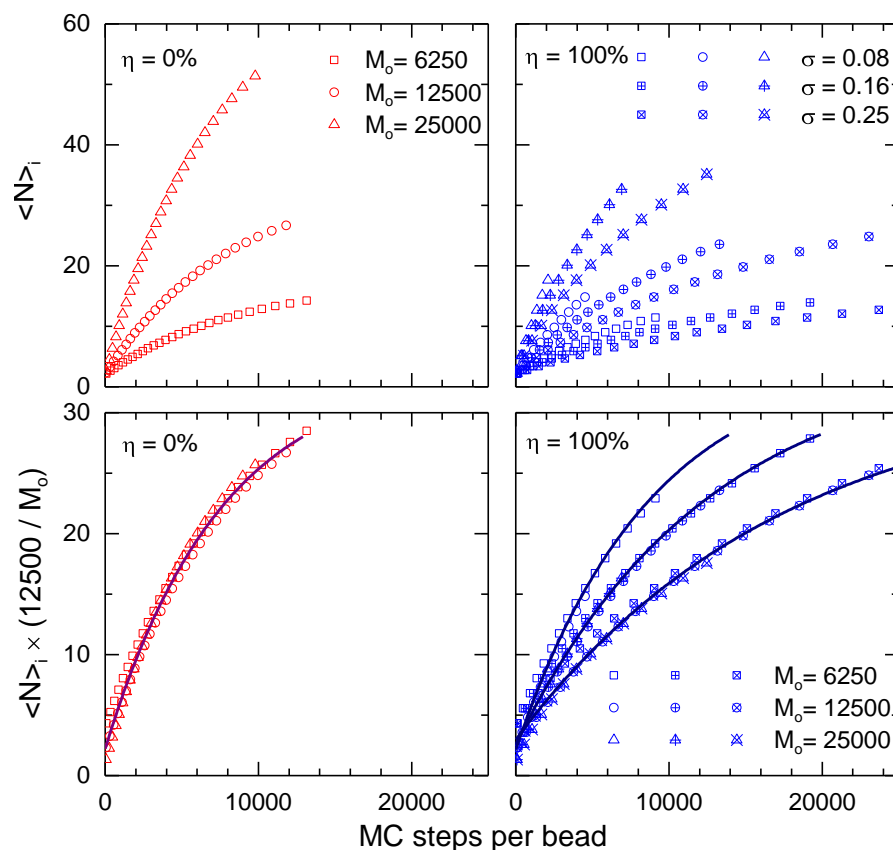


**Figure 5.3.** Number average molecular weight (top row) and the same quantity scaled (bottom row) for bulk (left column, red,  $\eta = 0\%$ ) and surface (right column, blue,  $\eta = 100\%$ ) polymers as a function of Monte Carlo steps per bead for initial number of monomers ( $M_0$ ): 6250 (squares), 12500 (circles), and 25000 (triangles); grafting density of initiators ( $\sigma$ ): 0.08 (hollow), 0.16 (cross), and 0.25 (ex). The purple and dark blue lines are guides to the eye for the bulk- and surface-initiated data, respectively.

of  $\sigma$  and  $\eta$ . Generally,  $\delta$  decrease with decreasing  $\sigma$  and increasing  $\eta$ . These observations, on which we will elaborate more in the following sections, suggest that the common practice of associating the properties of surface-grown polymers with those polymerized in the bulk is of limited validity.

In order to understand the growth rate of both sets of polymers we plot  $\langle N \rangle_B$  (left) and  $\langle N \rangle_S$  (right) as a function of MC step per simulation bead (**Figure 5.3**) for  $\eta = 0\%$  (left column) and  $100\%$  (right column). The top row shows the raw data. As expected, increases in  $M_0$  lead to larger rates of polymerization (initial slopes of the plots) and polymer molecular weights. The rate of polymerization of surface-grown polymers also depends on  $\sigma$ ; it decreases with increasing  $\sigma$ . Furthermore, the rate of polymerization for surface-initiated polymers at low  $\sigma$  is similar to that of the bulk-initiated chains. This reinforces the claim that, at  $\sigma$ ,  $x_m$  and  $\langle N \rangle_S$ , the low chain crowding on the surfaces results in similar growth for bulk and surface polymers. Classic polymerization kinetics suggests that the rate of polymerization is proportional to the free monomer concentration. To verify this we use the  $M_0 = 12500$  case as a benchmark and scale the data by multiplying times  $12500/M_0$  (bottom row, **Figure 5.3**). All bulk data and surface data for a given value of  $\sigma$  overlap visually confirming the rate dependence on  $M_0$ . **Figure 5.4** shows the scaled data for various combinations of  $\eta$ ,  $\sigma$ , and  $M_0$ . For all cases displayed, the initial rate of polymerization of bulk and surface polymers matches relatively well the  $\eta = 0\%$  (purple line) and  $\eta = 100\%$  (dark blue line) cases, respectively. Identical trends to those observed in **Figure 5.2** are identified in **Figure 5.4**. A few trends can be identified. First, while increasing  $\eta$  leads to larger deviations among the various

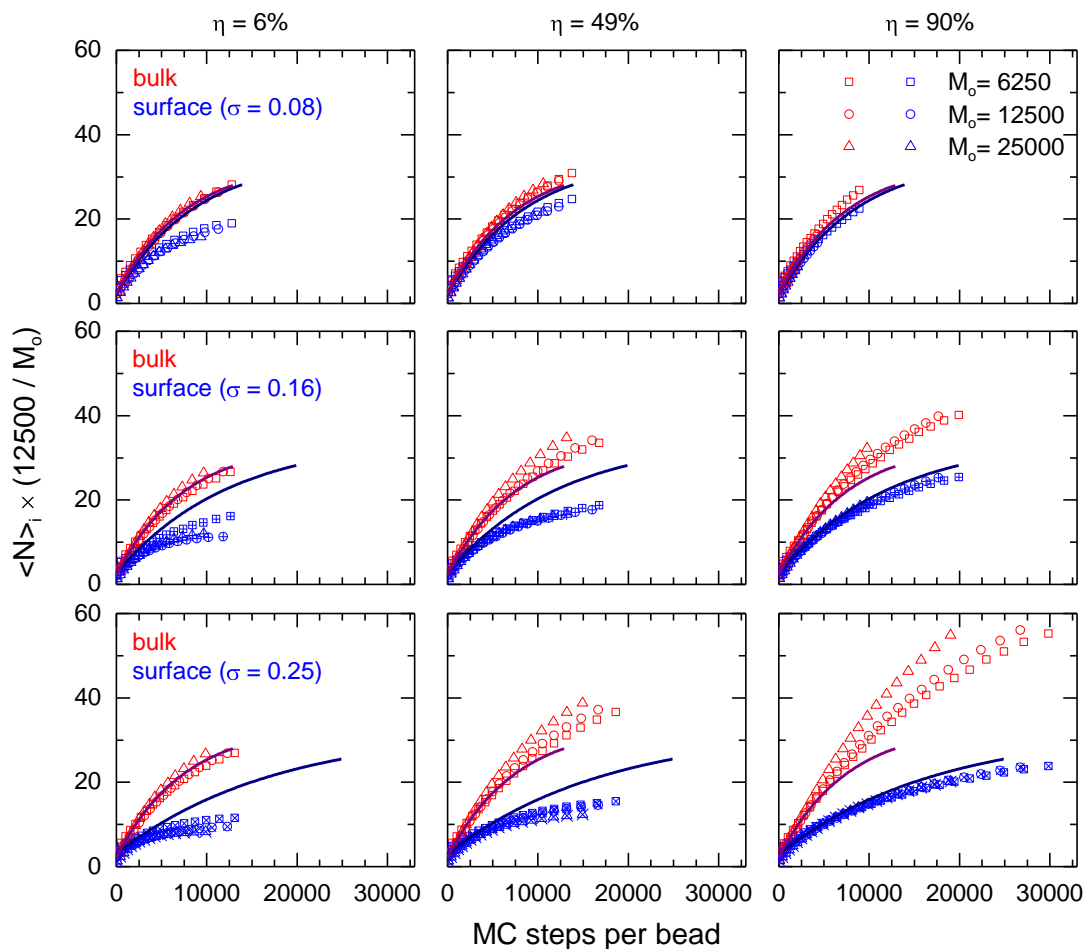


**Figure 5.4.** Scaled number average molecular weight as a function of Monte Carlo step per bead for bulk (red) and surface (blue) polymers with fraction of surface polymers ( $\eta$ , left to right columns): 6%, 49%, and 90%; initiator grafting densities ( $\sigma$ , top to bottom rows): 0.08, 0.16, and 0.25; initial number of monomers ( $M_0$ ): 6250 (squares), 12500 (circles), and 25000 (triangles). The solid lines correspond to  $\eta = 0\%$  (purple) and  $\eta = 100\%$  (dark blue).

$M_0$  cases for bulk polymers but improves the data collapse for surface-initiated polymers. Second, with increasing  $\eta$ ,  $\langle N \rangle_B$  increases above the case corresponding to bulk-only polymerization. Concurrently, there is a corresponding decrease in  $\langle N \rangle_S$  with increasing  $\eta$ ; the molecular weights of surface-grown polymers are generally lower than during surface-only initiated

polymerizations. The aforementioned effects increase with increasing  $\sigma$ . The initial rates of polymerization obtained by fitting a first-order exponential to the data ( $x_m < 0.2$ ) and evaluating the derivative at  $x_m = 0$  are plotted in **Figure 5.5**. We observe a dependence of the initial rate of polymerization on  $M_o$  indicating that the majority (but not all) of the rate variation is accounted for by scaling the data by  $M_o$ . Two additional and somewhat related factors that may be affecting the rate of polymerization include i) diffusion limitation and ii) the percentage of accepted attempted moves. First, diffusion limitation can arise if the monomer concentration decreases close to the surface or in proximity to the polymer chain-ends. This effect results in faster polymerization rates as  $M_o$  increases. Second, the move acceptance rate can affect the initial polymerization rates by perturbing the time unit in the simulation. As we increase  $M_o$ , for example, we increase the lattice occupancy and therefore the probability of an attempted move to an already occupied lattice site. This would lead to a higher fraction of attempted moves being rejected (due to excluded volume) resulting in slower simulation dynamics. In this case, we expect the polymerization rates for  $M_o = 25000$  to be slower. Barring other factors, it appears that diffusion limitation may play a role in our simulations, although this effect is small compared to that of  $M_o$ . **Figure 5.5** also depicts the dependence of the initial polymerization rate on  $\sigma$  for bulk and surface polymers. In most cases the rate of

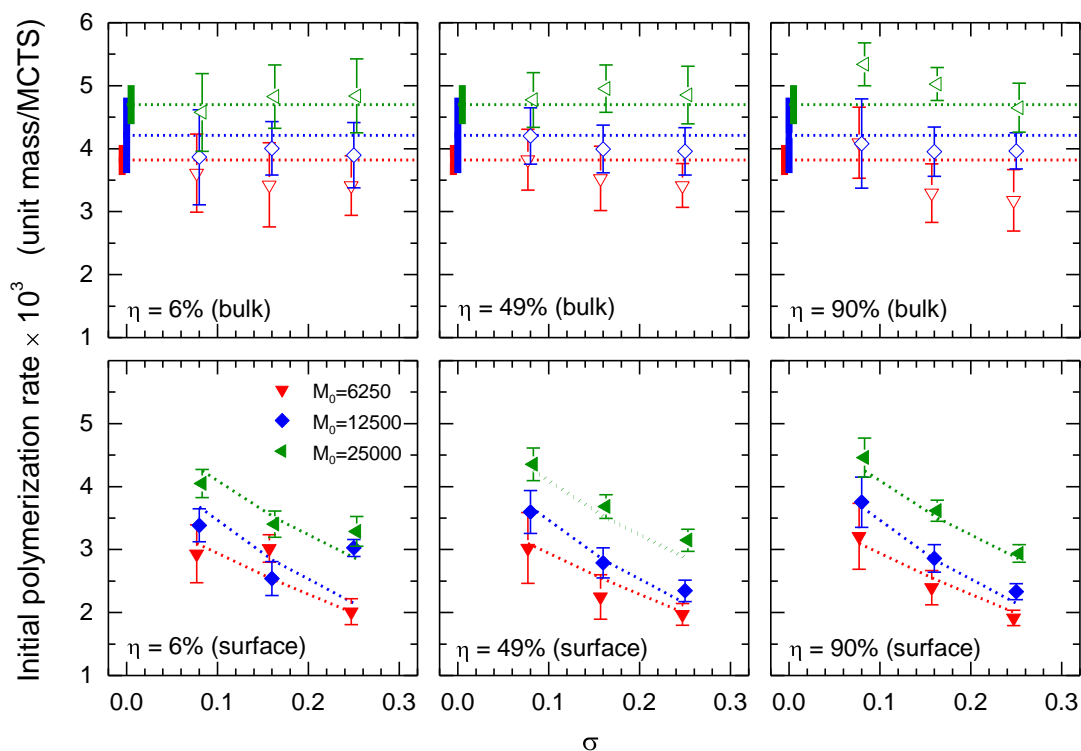


**Figure 5.5.** Initial polymerization rate as a function of  $\sigma$  for bulk (open symbols, top row) and surface (close symbols, bottom row) for  $\eta$  equal to 6% (left column), 49% (middle column), and 90% (right column) and  $M_0$  equal to 6250 (red down triangle), 12500 (blue diamond), and 25000 (green left triangle). For clarity, the data for  $M_0 = 6250$  and  $M_0 = 25000$  have been shifted horizontally by a small arbitrary increment to the left and right, respectively. The dotted lines in the top and bottom rows represent  $\eta = 0\%$  (bulk-only polymerization and 100% (surface-only polymerization), respectively. The solid vertical lines in the top row at  $\sigma = 0$  denote the range of the  $\eta = 0\%$  data.

bulk polymerization is independent of  $\sigma$  (the sole exception being the  $\eta = 90\%$  and  $M_0 = 25000$  case). The bulk polymers, at least at the beginning of the reaction, are unaffected by the presence of the surface growing polymers or by their grafting density. The surface polymers, however, do exhibit a polymerization rate dependence on the value of  $\sigma$  as would be expected from the

findings in **Chapter 5.4**. As  $\sigma$  increases, the rate of polymerization decreases consistently, a likely consequence of chain crowding at the surface.

To better discern the relation between the molecular weights of surface and bulk grown polymers at a particular instant in the polymerization, in **Figure 5.6** (top row) we plot the number average molar mass of the surface grown polymers ( $\langle N \rangle_S$ ) as a function of the number average molar mass of the bulk polymers ( $\langle N \rangle_B$ ). The black dashed line corresponds to  $\langle N \rangle_B = \langle N \rangle_S$ . For all combinations of  $\sigma$ ,  $\eta$ , and  $M_0$ , the data lies below the diagonal indicating that  $\langle N \rangle_S$  is smaller than  $\langle N \rangle_B$  at all conversions. Thus, an important characteristic of these systems is the competition for free monomers between the bulk and surface polymers and the higher growth rate of the bulk polymers relative to the surface ones. This is a clear indication that confining the initiators on the flat surface reduces their rate of polymerization. As the density and confinement of the initiators on the surface increases, the difference between the growth rates of the surface and bulk polymers widens yielding shorter surface-bound chains.

Inspecting the top row of **Figure 5.6** we observe that the data lies closer to the diagonal on going from  $\eta = 6\%$  to  $\eta = 90\%$  (from left to right). This is counterintuitive since we invoke confinement and crowding as the reasons for the difference between  $\langle N \rangle_S$  and  $\langle N \rangle_B$ . As explained before, the confinement on the surface for all values of  $\eta$  is identical as long as  $\sigma$  remains constant. One

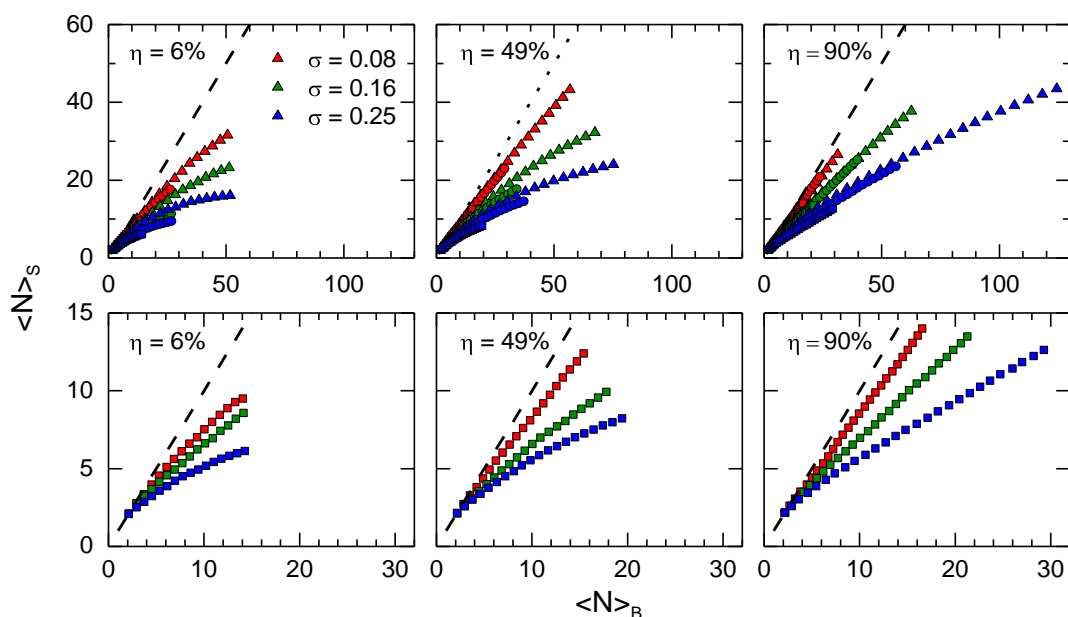


**Figure 5.6.** Number average molecular weight of surface polymers as a function of number average molecular weight of bulk polymers for the three values of  $M_0$  (top row) and for  $M_0 = 6250$  (bottom row). Percentage of surface polymers ( $\eta$ ): 6% (left column), 49% (middle column), and 90% (right column); initial number of free monomers ( $M_0$ ): 6250 (squares), 12500 (circles), and 25000 (triangles); grafting density of initiators ( $\sigma$ ): 0.08 (red), 0.16 (green), and 0.25 (blue). The dashed line represents  $\langle N \rangle_s = \langle N \rangle_B$ .

would expect that an increase in  $\eta$  would have no effect in the deviation of the data from the diagonal. We explain this by the presence (or lack thereof) of the fast growing polymers in the bulk. At  $\eta = 6\%$  most of the polymers in the simulation are fast-growing bulk polymers. The large amount of these fast growing polymers, relative to the polymers attached to the surface, lead to a larger difference between the molecular weights in the bulk and surface. At high  $\eta$ , the slow-growing surface polymers outnumber the bulk polymers. Although the bulk polymers possess a faster growing rate per chain, as a group they add less monomer than the surface-based chains. This results in the observed shift of

the trends towards the diagonal and the better match between  $\langle N \rangle_S$  and  $\langle N \rangle_B$  at the large values of  $\eta$ .

An important trend to note from **Figure 5.6** is the behavior of the final values of the average molecular weights ( $\langle N \rangle_S(x_m=0.80)$  and  $\langle N \rangle_B(x_m=0.80)$ ) as a function of  $\sigma$  and  $\eta$  for the  $M_o = 6250$  case (bottom row). At  $\eta = 6\%$ ,  $\langle N \rangle_B(0.80)$  is almost constant with increasing  $\sigma$ . However, as  $\sigma$  increases,  $\langle N \rangle_S(0.80)$  decreases from  $\approx 10$  to  $\approx 7$ . At  $\eta = 90\%$  both  $\langle N \rangle_S(0.80)$  and  $\langle N \rangle_B(0.80)$  depend on  $\sigma$ .  $\langle N \rangle_S(0.80)$  decreases from  $\approx 14$  to  $\approx 13$  and  $\langle N \rangle_B(0.80)$  increases from  $\approx 17$  to  $\approx 30$ . The latter observation is intriguing because one would not expect  $\sigma$ , which is a property of the surface, to have such a large effect on the final average molecular weight of the bulk polymers. To explain this we have to take into consideration the effect of crowding/confinement on the rate of surface polymerization, the relative rates of surface and bulk growth, and the ratio of bulk polymers to free monomers. The slight variation in  $\langle N \rangle_B$  with  $\sigma$  is explained by noting that the surface in this system constitutes a small perturbation and therefore cannot inflict a large effect on the bulk polymers. The differences in  $\langle N \rangle_S(0.80)$  are due to the crowding and slowing down of the surface-initiated reaction at higher  $\sigma$  (cf. **Chapter 4**). In the  $\eta = 90\%$  case, the decrease in  $\langle N \rangle_S(0.80)$  is still explained by the effects of surface confinement. The large increase in  $\langle N \rangle_B(0.80)$ , however, is interesting and somewhat more complex to

explain. In this system, the surface plays a very significant role because this is where most of the polymers are located. As  $\sigma$  increases, the rate of polymerization of surface-initiated polymers slows down and because surface-initiated polymers are the majority component, the overall rate of polymerization decreases as well. In contrast to  $\eta = 6\%$ , the bulk polymers only compete with the slow-growing surface-based polymers. The same trends are expected for higher values of  $M_0$  although they cannot be observed here due to the aforementioned truncation of the datasets at  $\eta = 90\%$  (cf. **Table 5.2**).

As mentioned above, we aim to explore the consequences of these findings on the common practice of assuming similar properties between simultaneously grown bulk and surface polymers and using this assumption to estimate  $\sigma$ . The typical approach involves measuring the dry thickness of the polymer layer by means of optical ellipsometry or neutron/x-ray reflectometry. Equation 5.1 requires the knowledge of  $\langle N \rangle_s$ , which is commonly assumed to be equal to  $\langle N \rangle_b$ , as measured by SEC. As can be seen in **Figure 5.6** the only situation in which this assumption is nearly valid is for small values of  $\sigma$  on flat substrates. At high  $\sigma$ , the differences between  $\langle N \rangle_b$  and  $\langle N \rangle_s$  are likely to be larger than the error of the SEC measurement resulting in inaccurate estimates for  $\sigma$ . These results highlight the need for continued development of direct measurement

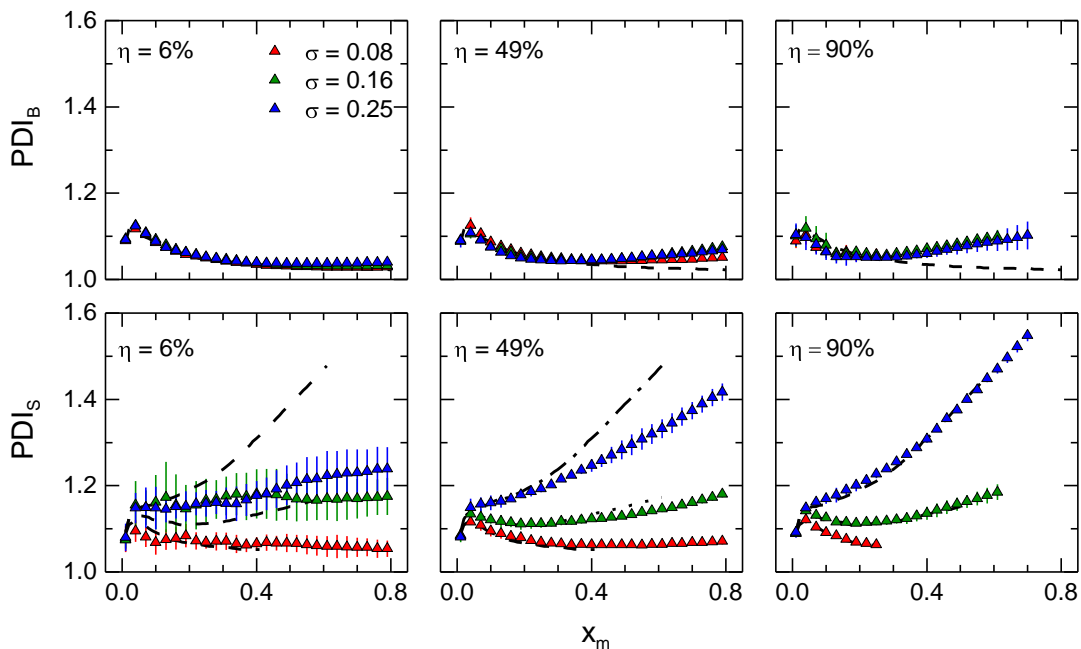


**Figure 5.7.** Polydispersity index for bulk (top row) and surface (bottom row) polymers as a function of monomer conversion with initial number of monomers ( $M_o$ ) of 25000; percentages of surface polymers ( $\eta$ ): 6% (left column), 49% (middle column) and 90% (right column); grafting densities of initiators ( $\sigma$ ): 0.08 (red), 0.16 (green) and 0.25 (blue). The black dashed lines represent the  $\eta = 0\%$  (top row) and  $\eta = 100\%$  (bottom row),  $M_o = 25000$  and  $\sigma = 0.08, 0.16$  and  $0.25$  conditions.

experimental techniques of either  $\langle N \rangle_S$  or  $\sigma$  (one potential approach is described in **Chapter 6** - Outlook and future research).

The simultaneous polymerization of bulk and surface-anchored initiators also influences the broadness of the molecular weight distributions of both populations of polymers. We monitor the PDI of bulk (top) and surface (bottom) polymers as a function of  $x_m$ ,  $\eta$  and  $\sigma$  for  $M_o = 25000$  in **Figure 5.7**. At low  $\eta$ , the  $PDI_B$  resembles very closely the situation corresponding to  $\eta = 0\%$  case for all values of  $\sigma$ . As  $\eta$  increases, the PDI deviates above the  $\eta = 0\%$  line at

approximately  $x_m = 0.3$ . This is an additional indication that when the surface polymers constitute the majority component in the simulation they can affect the properties of the bulk polymers. As with  $\langle N \rangle$ , we observe the opposite trend for the surface polymers. At  $\eta = 90\%$ , the PDIs of the surface-grown polymers are nearly identical with those corresponding to the polymerization of only surface-based polymers (i.e.,  $\eta = 100\%$ ). With decreasing  $\eta$ , the PDI<sub>S</sub> lines for  $\sigma$  equal to 0.16 and 0.25 are below the  $\eta = 100\%$  like. This is difficult to see in the  $\eta = 6\%$  case because the error in the PDI of such a small number of polymers is significant. At a particular conversion, the presence of bulk polymers imparts a lower PDI to the surface-grown polymers. Although this observation is intriguing, it is misleading, as we will explain below.

The data in **Figure 5.8** show the evolution of the PDI of the bulk and surface polymers as a function of monomer conversion for  $\eta = 49\%$  and  $M_0$  equal to 6250, 12500, and 25000. When plotted against monomer conversion one can see how the results of a hypothetical SEC experiment would depict the broadness of the distributions at any time during the polymerization reaction. At  $\sigma = 0.08$ , the assumption that the PDI obtained for the bulk polymers is similar to that of those initiated from the surface is a reasonable one. However, as  $\sigma$  increases to 0.25, this assumption ceases to be valid and PDI<sub>B</sub> underestimates PDI<sub>S</sub> for all values of  $M_0$ . At  $x_m = 0.8$  and  $M_0 = 25000$  the difference in the PDI of the surfaces

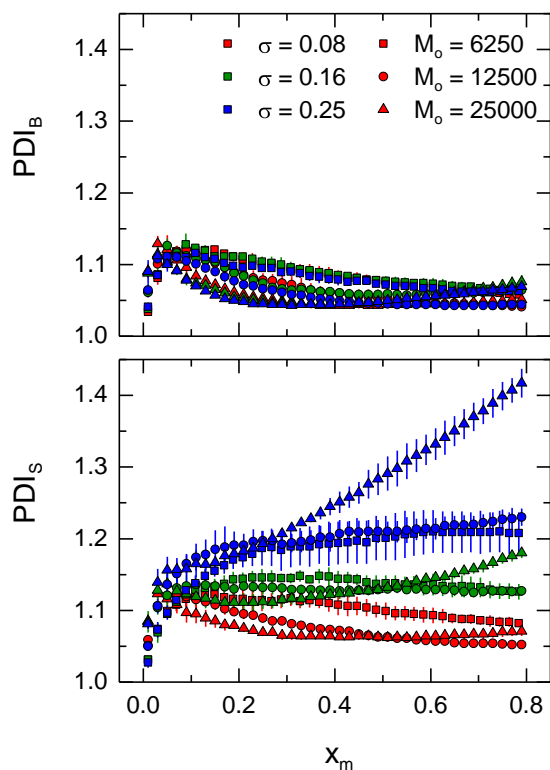


**Figure 5.8.** The PDIs of bulk (top) and surface (bottom) polymers as a function of the monomer conversion for  $\eta = 49\%$ . Initiator grafting densities ( $\sigma$ ): 0.08 (red), 0.16 (green) and 0.25 (blue); initial number of free monomers ( $M_o$ ): 6250 (squares), 12500 (circles) and 25000 (triangles).

from that of the bulk is approximately 0.3. A change of this magnitude in the PDI will most certainly alter the properties of the surface-grown polymer layers<sup>19</sup> (thickness, density, etc.) and therefore their performance in practical applications<sup>20</sup> (i.e. anti-fouling coatings). These observations suggest that in order to assume that the simultaneously grown bulk and surface polymers possess similar properties it is necessary to know the value of  $\sigma$  precisely. As

described above, estimation of  $\sigma$  requires that the properties between bulk and surface polymers be similar, resulting in a circular problem.

Our main motivation to explore polymerizations with different values of  $M_0$  is the possibility that  $\langle N \rangle_s$  has an effect on the growth rate and PDI of polymers grown from flat surfaces. For instance, at the beginning of the polymerization when  $\langle N \rangle_s$  is low, the surface-based polymers grow with little or no crowding. With increasing polymerization time, the molecular weight increases and neighboring chains will approach one another. At some point, excluded volume interactions will cause chain stretching away from the surface. In addition, chain crowding among neighbors may hinder the delivery of monomers to the chains with conformations in which the chain ends reside inside the polymer layer. Whereas plotting the PDIs as a function of conversions elucidates the differences between bulk and surface polymers at a particular instant during the polymerization, they mask the dependence that the PDI may have on the average molecular weights. A plot of the PDI as a function of the average molecular weight of the polymers can show this type of dependency effectively (**Figure 5.9**). When plotted against  $\langle N \rangle_B$  and  $\langle N \rangle_s$ , the  $PDI_B$  and  $PDI_s$  are independent of  $M_0$  because for a given value of  $\langle N \rangle_B$  or  $\langle N \rangle_s$  we consider the same number of beads in the bulk- or surface-based polymer, respectively, regardless of the solution conditions. The bulk polymers also prove to be

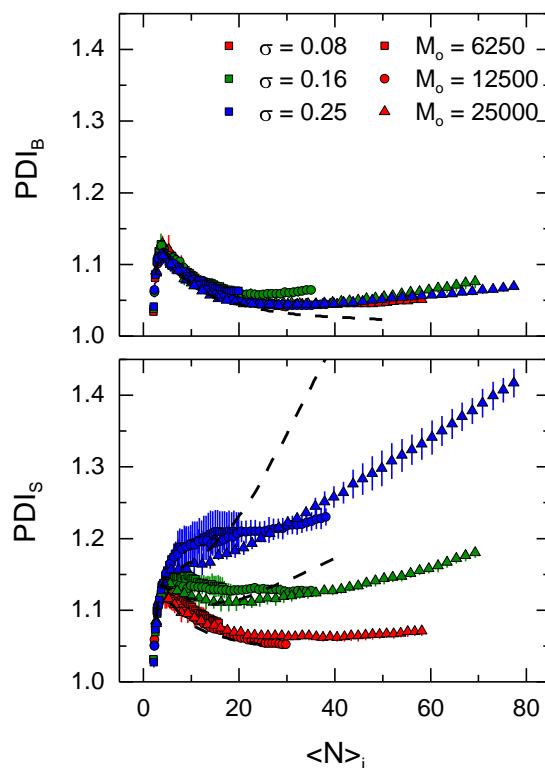


**Figure 5.9.** The PDIs of bulk (top) and surface (bottom) polymers as a function of the average molar mass of bulk and surface polymers, respectively, for  $\eta = 49\%$ . Initiator grafting densities ( $\sigma$ ): 0.08 (red), 0.16 (green) and 0.25 (blue); initial number of free monomers ( $M_o$ ): 6250 (squares), 12500 (circles) and 25000 (triangles). The black dashed lines represent the  $\eta = 0\%$  (top) and  $\eta = 100\%$  (bottom),  $M_o = 25000$  and  $\sigma = 0.08, 0.16$  and  $0.25$  conditions.

insensitive to  $\sigma$ , indicating that no matter what the characteristic of the surface are, the bulk polymers that grow to a particular molecular weight possess similar PDIs. The surface-grown polymers, however, do exhibit a dependence on  $\sigma$  as should be expected from the study described in **Chapter 4**. As  $\sigma$  increases, the PDI<sub>s</sub> increases due to chain crowding resulting in the uneven delivery of monomers to the short and long chains. The insensitivity of the PDI to the value

of  $M_0$  explains our observation that the addition of bulk polymers ( $\eta = 6$  and 49 percent) seems to have a controlling effect on  $PDI_S$  in **Figure 5.7**. The correct explanation for the perceived decrease in  $PDI_S$  is that the presence of bulk polymers results in a lower  $\langle N \rangle_S$  at a particular  $x_m$  and therefore a lower level of confinement.

In this work, we have established that  $\eta$  and  $\sigma$  have a strong effect on the MWDs of bulk- and surface-grown polymers and that knowing these parameters is essential for the validation of the  $\langle N \rangle_B \approx \langle N \rangle_S$  assumption. We now draw parallels between the range of  $\sigma$  and  $\eta$  studied here and those found in the experimental literature. Experiments where the initiation of surface polymerization occurs from a planar substrate operate often at very low values of  $\eta$  (or  $\eta = 0\%$ , i.e. no sacrificial initiator) due primarily to the low surface area of the planar sample. Thus, the determination of  $\sigma$  encounters problems outlined in this Chapter. For example, Husseman et al.<sup>15</sup>, and Koylu and Carter<sup>21</sup> performed their experiments at  $\eta \ll 0.0001\%$  and  $0.01\%$ , respectively. The values of  $\sigma$  calculated by the authors in these studies ranged from 0.5 to 1.4 chains/nm<sup>2</sup>. Koylu and Carter concluded that the assumption of equal bulk and surface average molecular weights is not universally valid based on their SEC measurements of the grafted and solution chains. Koylu and Carter reported a lower molecular weight of polymers grown in solution relative to those

polymerized from the substrate, which is opposite to the trend described here. Based on their computed values of  $\sigma$  ( $\approx 1.0$  chain/nm<sup>2</sup>), the estimated value of  $\eta$  cited above, and the data in **Figure 5.4** we would expect the average molecular weight on the surface to be substantially smaller than that in the bulk. Husseman and coworkers did not measure the molecular weight of the brushes grown from planar substrates. Instead, their results showed similar molecular weights and PDIs between polymer cleaved from silica gel particles and those free in solution. Here the positive curvature of the substrate may have contributed to a relatively low PDI of the surface-initiated polymers. A comparison to polymers grown from the substrate is thus not appropriate unless one works with very low values of  $\sigma$ . Jeyaprakash et al. compared ATRP polymerizations with added deactivators ( $\eta = 100\%$ ) and with sacrificial initiators ( $\eta$  unknown) and showed that polymerizations in the presence of deactivators produce thicker grafted layers than those carried out in the presence of free initiators. The explanation Jeyaprakash and coworkers put forth is consistent with our observations, i.e.,  $\eta$  affects the rate of polymerization of the surface-initiated polymers and can therefore lead likely to polymers with  $\langle N \rangle_S \neq \langle N \rangle_B$ .

Silica based mesoporous materials can also serve as supports for surface initiated CRP studies. In this case, it is possible to cleave sufficient amount of material for SEC analysis. However, the negative curvature of the initiator-

covered surfaces and the diffusion of monomer to the pores may accentuate the effects observed in this study. Kruk et al.<sup>6</sup> performed such polymerizations at  $\eta = 0\%$  and noted that the polymerization was controlled and the PDI remained as small as in solution based ATRP ( $< 1.1$ ). Pasetto<sup>22</sup> and coworkers, however, performed polymerizations from similar mesoporous materials in the whole range of  $\eta$  and noted higher PDIs and lower molecular weights for the surface bound polymers. Similar conclusions have been reached in the study of Gorman and coworkers.<sup>23</sup> This inconsistency of observations for both planar substrates and mesoporous materials highlights the need for continued research in the area and for a systematic investigation of the effects of  $\eta$  and  $\sigma$  in the controlled growth of polymer chains. The simulations performed here can serve as a guide to the proper design of such investigation.

#### **5.4. Conclusions**

The computer simulations implemented herein provide insight into the competitive growth of macromolecules initiated simultaneously in the bulk- and on the flat surface. We observe that the common assumption invoked in the literature of equality between the molecular weights of the surface- ( $\langle N \rangle_s$ ) and bulk- ( $\langle N \rangle_B$ ) based polymers is not generally valid. We find that  $\langle N \rangle_B > \langle N \rangle_s$ . Furthermore, the broadness of the molecular weight distribution of surface-

grown polymers is highly dependent on their grafting density ( $\sigma$ ), suggesting that claims, often found in literature, of narrowly distributed surface-grown polymers polymerized by means of living polymerization is not generally true.

We confirm that  $\sigma$  has important effect on the growth rate and polydispersity of surface-grown polymers. Depending on the percentage of polymers on the surface ( $\eta$ ), the properties of the bulk polymers are also affected by  $\sigma$ , which is a surface property. When  $\eta$  is large, the surface represents a strong perturbation to the growth of bulk polymers and as a consequence the molecular weights of the bulk polymers at a monomer conversion of 0.8 increase with increasing  $\sigma$ . This is attributed to the fact that at low  $\eta$  the bulk polymers compete with each other (they are the majority component) while at high  $\eta$  they compete primarily with the slow-growing surface polymers.

By performing simulations at various initial numbers of free monomers ( $M_0$ ) we were able to confirm that the initial rate of polymerization is depends proportionally on  $M_0$ . However, diffusion limitation likely affects the polymerization; this effect becomes less important with increasing  $M_0$ . The initial rates of polymerization also depend on  $\sigma$ . Increasing  $\sigma$  results in decreases in the rate of polymerization, confirming the results presented in **Chapter 4** of this Ph.D Thesis.

## 5.5. References

1. Brinks, M. K.; Studer, A. Polymer Brushes by Nitroxide-Mediated Polymerization. *Macromol. Rapid Commun.* **2009**, *30*, 1043-1057.
2. Barb y, R.; Lavanant, L.; Paripovic, D.; Sch wer, N.; Sugnaux, C.; Tugulu, S.; Klok, H. Polymer Brushes Via Surface-Initiated Controlled Radical Polymerization: Synthesis, Characterization, Properties, and Applications. *Chem. Rev.* **2009**, *109*, 5437-5527.
3. Jones, D. M.; Brown, A. A.; Huck, W. T. S. Surface-Initiated Polymerizations in Aqueous Media: Effect of Initiator Density. *Langmuir* **2002**, *18*, 1265-1269.
4. Jones, D. M.; Smith, J. R.; Huck, W. T. S.; Alexander, C. Variable Adhesion of Micropatterned Thermoresponsive Polymer Brushes: AFM Investigations of Poly (N-Isopropylacrylamide) Brushes Prepared by Surface-Initiated Polymerizations. *Adv. Mater.* **2002**, *14*, 1130-1134.
5. Jones, D. M.; Huck, W. T. S. Controlled Surface-Initiated Polymerizations in Aqueous Media. *Adv. Mater.* **2001**, *13*, 1256-1259.
6. Kruk, M.; Dufour, B.; Celer, E. B.; Kowalewski, T.; Jaroniec, M.; Matyjaszewski, K. Grafting Monodisperse Polymer Chains from Concave Surfaces of Ordered Mesoporous Silicas. *Macromolecules* **2008**, *41*, 8584-8591.
7. Matyjaszewski, K.; Dong, H.; Jakubowski, W.; Pietrasik, J.; Kusumo, A. Grafting from Surfaces for "Everyone": ARGET ATRP in the Presence of Air. *Langmuir* **2007**, *23*, 4528-4531.
8. Pyun, J.; Kowalewski, T.; Matyjaszewski, K. Synthesis of Polymer Brushes using Atom Transfer Radical Polymerization. *Macromol. Rapid Commun.* **2003**, *24*, 1043-1059.
9. Matyjaszewski, K.; Miller, P. J.; Shukla, N.; Immaraporn, B.; Gelman, A.; Luokala, B. B.; Siclovan, T. M.; Kickelbick, G.; Vallant, T.; Hoffmann, H.; Pakula, T. Polymers at Interfaces: Using Atom Transfer Radical Polymerization in the Controlled Growth of Homopolymers and Block Copolymers from Silicon Surfaces in the Absence of Untethered Sacrificial Initiator. *Macromolecules* **1999**, *32*, 8716-8724.

10. Gautrot, J. E.; Trappmann, B.; Ocegüera-Yanez, F.; Connelly, J.; He, X.; Watt, F. M.; Huck, W. T. S. Exploiting the Superior Protein Resistance of Polymer Brushes to Control Single Cell Adhesion and Polarisation at the Micron Scale. *Biomaterials* **2010**, *31*, 5030-5041.
11. Moglianetti, M.; Webster, J. R. P.; Edmondson, S.; Armes, S. P.; Titmuss, S. Neutron Reflectivity Study of the Structure of pH-Responsive Polymer Brushes Grown from a Macroinitiator at the Sapphire-Water Interface. *Langmuir* **2010**, *26*, 12684-12689.
12. Takahashi, H.; Nakayama, M.; Yamato, M.; Okano, T. Controlled Chain Length and Graft Density of Thermoresponsive Polymer Brushes for Optimizing Cell Sheet Harvest. *Biomacromolecules* **2010**, *11*, 1991-1999.
13. Ye, Q.; Wang, X.; Li, S.; Zhou, F. Surface-Initiated Ring-Opening Metathesis Polymerization of Pentadecafluorooctyl-5-Norbornene-2-Carboxylate from Variable Substrates Modified with Sticky Biomimic Initiator. *Macromolecules* **2010**, *43*, 5554-5560.
14. Matyjaszewski, K.; Xia, J. H. Atom Transfer Radical Polymerization. *Chem. Rev.* **2001**, *101*, 2921-2990.
15. Husseman, M.; Malmström, E. E.; McNamara, M.; Mate, M.; Mecerreyes, D.; Benoit, D. G.; Hedrick, J. L.; Mansky, P.; Huang, E.; Russell, T. P.; Hawker, C. J. Controlled Synthesis of Polymer Brushes by "Living" Free Radical Polymerization Techniques. *Macromolecules* **1999**, *32*, 1424-1431.
16. Turgman-Cohen, S.; Genzer, J. Computer Simulation of Controlled Radical Polymerization: Effect of Chain Confinement due to Initiator Grafting Density and Solvent Quality in "Grafting from" Method. *Macromolecules* **2010**, *43*, 9567-9577.
17. Goto, A.; Fukuda, T. Kinetics of Living Radical Polymerization. *Prog. Polym. Sci.* **2004**, *29*, 329-385.
18. Jeyaprakash, J. D.; Samuel, S.; Dhamodharan, R.; Rühle, J. Polymer Brushes Via ATRP: Role of Activator and Deactivator in the Surface-Initiated ATRP of Styrene on Planar Substrates. *Macromolecular Rapid Communications* **2002**, *23*, 277-281.

19. de Vos, W.; Leermakers, F. Modeling the Structure of a Polydisperse Polymer Brush. *Polymer* **2009**, *50*, 305-316.
20. de Vos, W. M.; Leermakers, F. A. M.; de Keizer, A.; Kleijn, J. M.; Cohen Stuart, M. A. Interaction of Particles with a Polydisperse Brush: A Self-Consistent-Field Analysis. *Macromolecules* **2009**, *42*, 5881-5891.
21. Koylu, D.; Carter, K. R. Stimuli-Responsive Surfaces Utilizing Cleavable Polymer Brush Layers. *Macromolecules* **2009**, *42*, 8655-8660.
22. Pasetto, P.; Blas, H.; Audouin, F.; Boissière, C.; Sanchez, C.; Save, M.; Charleux, B. Mechanistic Insight into Surface-Initiated Polymerization of Methyl Methacrylate and Styrene Via ATRP from Ordered Mesoporous Silica Particles. *Macromolecules* **2009**, *42*, 5983-5995.
23. Gorman, C. B.; Petrie, R. J.; Genzer, J. Effect of Substrate Geometry on Polymer Molecular Weight and Polydispersity during Surface-Initiated Polymerization. *Macromolecules* **2008**, *41*, 4856-4865.

## CHAPTER 6

### OUTLOOK AND FUTURE WORK

#### 6.1. Polymerization from various geometries

Modification of convex and concave surfaces (**Figure 6.1**) with polymeric tethers represents an important technological step in a number of applications. Polymer brushes deposited onto convex supports are often used in applications involving fiber modification for specialty filters or steric stabilization of nanoparticles. Polymer grafts on concave surface find potential applications in changing the wettability of nanofluidic conduits and pores. Our research into the “grafting from” synthesis of polymer brushes has thus far focused in polymer growth from planar substrates. These planar substrates could, in fact, represent experimental planar geometries of low curvature supports (i.e. micron sized fibers, particles, pores, wrinkles, etc.). A study that follows naturally from the preceding work (and that we are ready to implement) involves “grafting from” polymerization from substrates of varying convex and concave curvatures. Our algorithm is suitable for simulations in these geometries as long as we

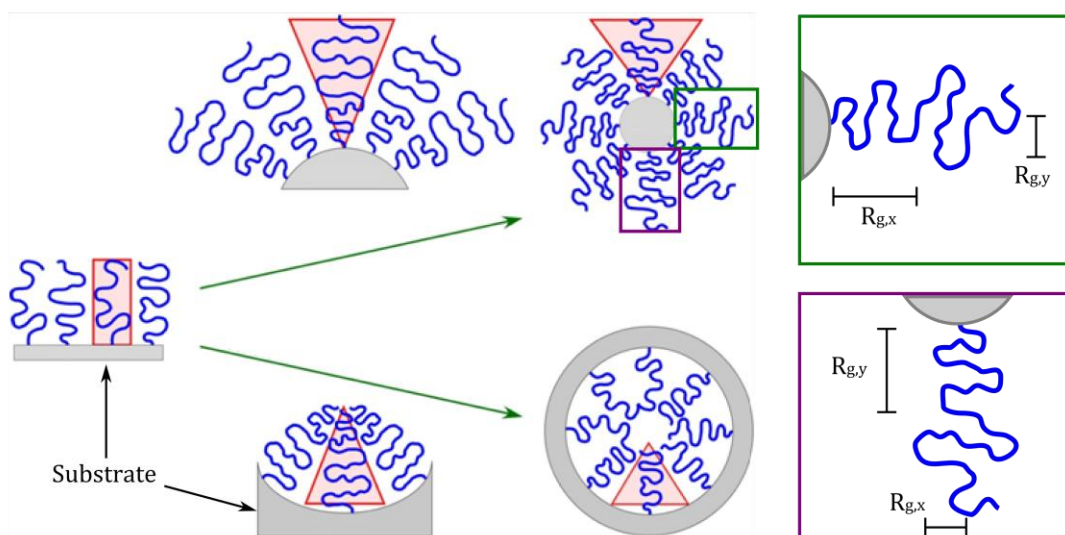


**Figure 6.1.** Schematic of polymers grafted to surfaces of various geometries. The squares represent the difference in shapes of equivalent chains with different orientation. This difference in the dimensions of the chains leads to issues in characterizing these chains solely by measuring the radius of gyration.

implement the proper initial conditions, establish relevant boundary conditions, and employ appropriate methods for analyzing the results.

The parameter space to be explored for such a study is large. It includes the fraction of surface grown polymers (**Chapter 5**), the surface density of initiators (**Chapter 4**), solvent quality (**Chapter 4**), and the curvature of the surface. A possible way to narrow the parameter space is to limit the study to surface-initiated polymerization ( $\eta = 100\%$ ) and to good solvent conditions ( $\epsilon = 4 \times 10^{-7}$ ). With this scope, the relevant parameters for the simulations are the curvature of the surface and the polymer grafting density. To complete such a study, it is important to gain insight into the variation in the confinement of the

polymer chains as a function of the substrate geometry. In **Chapter 4**, we accomplish this by monitoring the parallel and perpendicular components of the radius of gyration for surface and bulk polymers. The surface polymers extend away from the substrate resulting in larger average dimensions in the direction perpendicular to the substrate relative to the dimension in the direction parallel to the substrate. This approach will not suffice for surface-polymers grown from curved substrates like inside and outside cylinders or spheres. In these cases, the orientational averaging over various chain orientations will mask the possible asymmetry of shape exhibited by the coils (cf., **Figure 6.1**, boxes). It is thus necessary to measure the principal components of the radius of gyration tensor. Details on this procedure are outlined in **Appendix E**.

## **6.2. Molecular weight distribution of polymers (Schulz–Zimm)**

As mentioned in **Chapter 4**, de Vos and Leermakers<sup>1</sup> assume, a priori, that the polydispersity of brushes on substrates follows the Schulz–Zimm distribution. Our simulations allow us to obtain the full molecular weight distributions for polymerizations without any a priori assumption about the nature of the molecular weight polydispersity. At the end of **Chapter 3**, we discussed briefly that while the Schulz–Zimm distribution is appropriate for characterizing the molecular weight distributions of polymer brushes grown at

low  $\sigma$ , it fails to describe the distribution of tethered polymers at high  $\sigma$ . We therefore recommend investigating the ability of the Schulz-Zimm equation to describe our simulated molecular weight distributions and determine at which  $\sigma$  this equation ceases to be valid. Furthermore, we hypothesize that for any value of  $\sigma$  (even low values) there will be a crossover average molecular weight of the grafted polymers, at which chain crowding leads to an uneven chain growth, broadening of the molecular weight distribution, and consequently inability of the Schulz-Zimm model to describe the data quantitatively. A model that describes the data can then be formulated or, at the very least, distribution functions can be tested empirically to find one that describes the molecular weight distributions of surface grown polymers for all values of  $\sigma$  and  $N$ . We have already obtained much of the data needed for such a study from the simulations described in **Chapter 4**. To complete this research, however, it is necessary to perform additional repeat runs in order to gain better statistical certainty of the distributions.

### **6.3. Effects of termination and chain transfer**

One factor that we have omitted in **Chapters 4** and **5** of this dissertation are the effects of chain transfer and termination reactions on the molecular weight control and molecular weight distributions of the “grafting from” reactions.

Genzer<sup>2</sup> has already touched upon the effects of termination on surface-initiated polymerization, however, a systematic study of the role of termination and chain transfer is needed for a full range of grafting densities. We have already implemented subroutines aimed at modeling chain transfer reactions both to solvent (generating a new bead in the simulation) and to monomers. Those effects will be reported in follow up publications.

#### **6.4. Experimental studies mimicking the simulations**

The topics investigated in **Chapter 4** and **5** by means of computer simulation are challenging to attack experimentally. For planar substrates, the amount of polymer generated by surface-initiated radical polymerization is very small and difficult to characterize by common experimental techniques (i.e. SEC). We propose two routes for the direct measurement of the grafting density, average molecular weight, and molecular weight dispersity of surface grafted chains synthesized by the “grafting from” method.

##### *6.4.1. Size exclusion chromatography with refractive index detection*

Refractive index (RI) detectors represent some of the most sensitive detection means for SEC measurements. Depending on the properties of the polymer and the mobile phase, the sensitivity of an RI detector can be in the

hundreds of nanograms range.<sup>3,4</sup> In order to employ an RI detector in the SEC characterization of surface-initiated polymers, it is important to select judiciously the polymer/mobile phase pair to maximize the contrast afforded for detection. **Table 6.1** shows the refractive index increment ( $dn/dc$ ) of various common polymer/mobile phase pairs. Conveniently, one of the highest absolute values (positive or negative) of  $dn/dc$  is for the combination of polystyrene (PS) and tetrahydrofuran (THF). The large contrast afforded by the PS/THF pair combined with the extensive literature on PS polymerization by the various CRP schemes makes PS an ideal candidate for the study of the kinetics of surface-initiated polymerizations.

The subsequent experimental work would then involve growing PS brushes by ATRP<sup>5,6</sup> simultaneously for different times and cleave<sup>7,8</sup> the grafted polymers from the surface for characterization. In principle, we can employ this method to monitor with SEC the molecular weight and molecular weight distribution of the surface-grown polymer brushes as a function of polymerization time and other pertinent characteristics of the polymerization reaction. This procedure represents the standard method reported in the literature for direct characterization of the grafted polymers, however, there are some technical issues associated with it. One of the main problems is due to the small amount of cleaved material obtained. This will be especially significant in

**Table 6.1.** Common SEC solvents and their dn/dc when paired with common polymers. Obtained from <http://www.ampolymer.com>.

<b>Solvent</b>	<b>Polymer</b>	<b>dn/dc (ml/g)</b>
Tetrahydrofuran	Polyacrylic acid	0.0738-0.0994
	Epoxy Resin	0.1851-0.1884
	Polyamides	0.106
	Polymethyl methacrylate	0.08-0.0909
	<b>Polystyrene</b>	<b>0.187</b>
Toluene	Polystyrene	0.11
	Polydimethyl siloxane	-0.0913
N,N'-dimethylformamide	Polyamides	0.1747
	Polystyrene	0.159

the early stages of polymerization, when only minute amounts of polymers are present on the surface. Additional problems arise in the detection of the front and back tails of the molecular weight distribution. Because polymers are separated in the SEC process, the tails might fall under the detection limit of the RI detector, effectively leading to underestimation of the breadth of the distribution. Finally, this technique will only work for polymer/mobile phase pairs with high dn/dc values, which limit its applicability to only a few select polymer/solvent systems. Despite these limitations, a systematic study performed with such a methodology can begin elucidating the kinetics of surface-initiated polymerizations.

#### 6.4.2. *Size exclusion chromatography with fluorescence detection*

An alternative approach to RI detection involves coupling of SEC with sensitive fluorescence detectors. Previous research<sup>9,10</sup> has shown that it is possible to combine fluorescent tagging of polymer molecules, fluorescence detection, and SEC to characterize the molecular weights and molecular weight distributions of very small amounts of polymer samples (two orders of magnitude smaller than those achieved with RI detectors). This leads to new possibilities in the study surface-initiated polymerizations. Within the scope of the ATRP scheme, well-established methods for the modification of polymer end-groups with a variety of functional groups are already available.<sup>11-14</sup> One can then follow a similar methodology as that described for the RI detection study with a few variations. Such an approach would increase the detection sensitivity and ameliorate the problem of detection of the low and high molecular weight tails of the distribution. Depending on the methodology, it may be applicable to any polymer that can be synthesized by ATRP and even others given alternative tagging methods. An added advantage of using fluorescent tag modified end-groups in combination with ATRP is that the tagging will only occur on living chains. This means that tagging the polymers and monitoring the total amount of tagged material as a function of polymerization time can provide estimates to the amount of chains that have terminated or transferred during the reaction.

This type of information is impossible to obtain (to the best of our knowledge) with any of the currently available analytical techniques.

## 6.5. References

1. de Vos, W.; Leermakers, F. Modeling the Structure of a Polydisperse Polymer Brush. *Polymer* **2009**, *50*, 305-316.
2. Genzer, J. In Silico Polymerization: Computer Simulation of Controlled Radical Polymerization in Bulk and on Flat Surfaces. *Macromolecules* **2006**, *39*, 7157-7169.
3. Waters Corporation. Application Note: Waters 410 Differential Refractive Index Detector Sensitivity <http://www.waters.com/waters/library.htm?cid=511436&lid=1536419> (accessed 11/14/2010, 2010).
4. Turgman-Cohen, S.; Genzer, J. Unpublished.
5. Matyjaszewski, K.; Miller, P. J.; Shukla, N.; Immaraporn, B.; Gelman, A.; Luokala, B. B.; Siclovan, T. M.; Kickelbick, G.; Vallant, T.; Hoffmann, H.; Pakula, T. Polymers at Interfaces: Using Atom Transfer Radical Polymerization in the Controlled Growth of Homopolymers and Block Copolymers from Silicon Surfaces in the Absence of Untethered Sacrificial Initiator. *Macromolecules* **1999**, *32*, 8716-8724.
6. Min, K.; Gao, H.; Matyjaszewski, K. Use of Ascorbic Acid as Reducing Agent for Synthesis of Well-Defined Polymers by ARGET ATRP. *Macromolecules* **2007**, *40*, 1789-1791.
7. Husseman, M.; Malmström, E. E.; McNamara, M.; Mate, M.; Mecerreyes, D.; Benoit, D. G.; Hedrick, J. L.; Mansky, P.; Huang, E.; Russell, T. P.; Hawker, C. J. Controlled Synthesis of Polymer Brushes by "Living" Free Radical Polymerization Techniques. *Macromolecules* **1999**, *32*, 1424-1431.
8. Koylu, D.; Carter, K. R. Stimuli-Responsive Surfaces Utilizing Cleavable Polymer Brush Layers. *Macromolecules* **2009**, *42*, 8655-8660.

9. Moon, B.; Hoyer, T. R.; Macosko, C. W. Anionic Synthesis and Detection of Fluorescence-Labeled Polymers with a Terminal Anhydride Group. *J. Polym. Sci., Part A: Polym. Chem.* **2000**, *38*, 2177-2185.
10. Schulze, J. S.; Moon, B.; Lodge, T. P.; Macosko, C. W. Measuring Copolymer Formation from End-Functionalized Chains at a PS/PMMA Interface using FRES and SEC. *Macromolecules* **2001**, *34*, 200-205.
11. Coessens, V.; Nakagawa, Y.; Matyjaszewski, K. Synthesis of Azido End-Functionalized Polyacrylates Via Atom Transfer Radical Polymerization. *Polym. Bull.* **1998**, *40*, 135-142.
12. Coessens, V.; Matyjaszewski, K. End Group Transformation of Polymers Prepared by ATRP, Substitution to Azides. *J. Macromol. Sci. Part A Pure Appl. Chem.* **1999**, *36*, 667-680.
13. Coessens, V.; Matyjaszewski, K. End Group Transformation of Polymers Prepared by ATRP, Substitution to Azides. *J. Macromol. Sci. Part A Pure Appl. Chem.* **1999**, *36*, 653-667.
14. Lutz, J.; Börner, H. G.; Weichenhan, K. Combining Atom Transfer Radical Polymerization and Click Chemistry: A Versatile Method for the Preparation of End-Functional Polymers. *Macromol. Rapid Commun.* **2005**, *26*, 514-518.

## **APPENDICES**

## APPENDIX A

### NEXAFS AND ELLIPSOMETRY FOR SPUN-COATED ASPHALTENES

In order to 1) determine the asphaltene refractive index and 2) reconcile the NEXAFS spectra of asphaltenes adsorbed onto mixed SAMs, asphaltenes were spun-cast onto cleaned silicon wafer substrates from toluene solution (concentration 0.5% w/w) at 2000 rpm for 60 seconds. **Figure A.1** shows ellipsometric data for the spun-coated asphaltenes. The data were collected at  $\theta = 72.5^\circ$  (black),  $74.5^\circ$  (red) and  $76.5^\circ$  (green), where  $\theta$  represents the angle between the sample normal and the incoming light beam; the closed symbols represent  $\Psi$  and the open symbols represent  $\Delta$ . The lines were obtained by a 2 layer model (Si/SiO<sub>x</sub>/asphaltene), in which the thickness and refractive index of asphaltenes were fitted simultaneously. The asphaltene layer thickness determined in this way was found to be 3.48 nm, the refractive index was established to be 1.8.

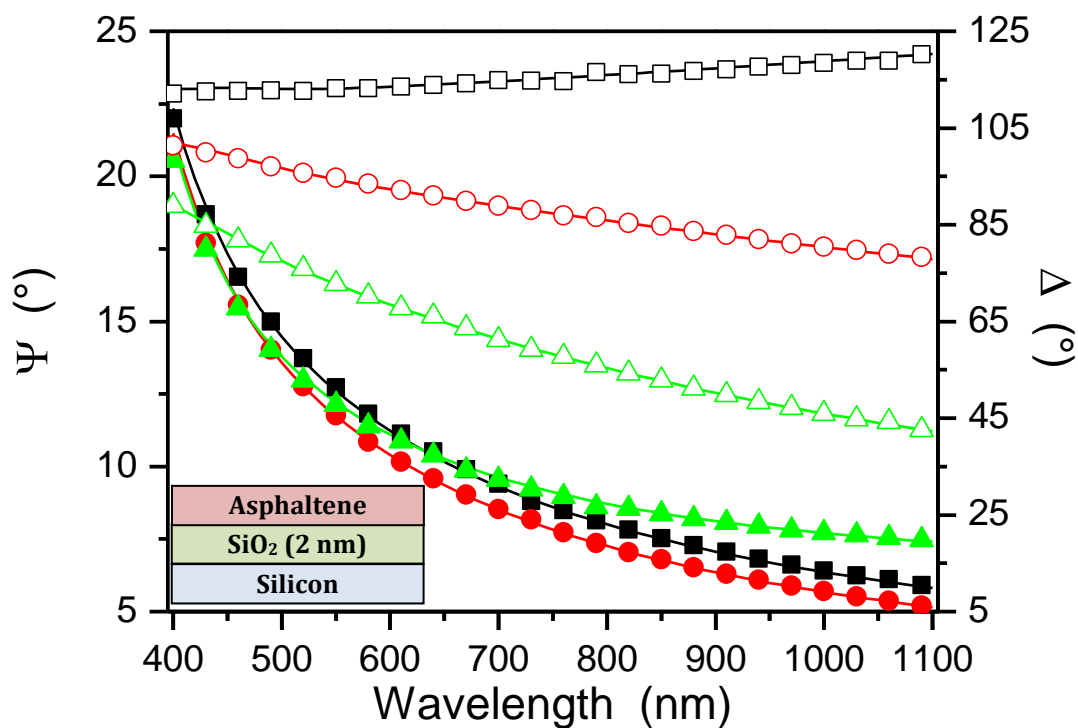


**Figure A.1.** Ellipsometry data for spun-coated asphaltenes. See text for details.

The normalized PEY NEXAFS spectra collected from the spun-coated Hondo asphaltenes at  $\theta = 50^\circ$ , where  $\theta$  is the angle between the surface normal and the electric vector of the x-ray beam, are plotted in **Figure A.2**. The pre-edge and post-edge of the spectra were normalized to zero and one, respectively, using the method described in the paper. The red line in **Figure A.2** represents a Gaussian lines-shape fitted to the  $1s \rightarrow \pi_{C=C}^*$  peak; it is used to determine the area and the position of the peak. The area is determined to be 1.96 in the arbitrary unit scale and the peak position is 285.40 eV.

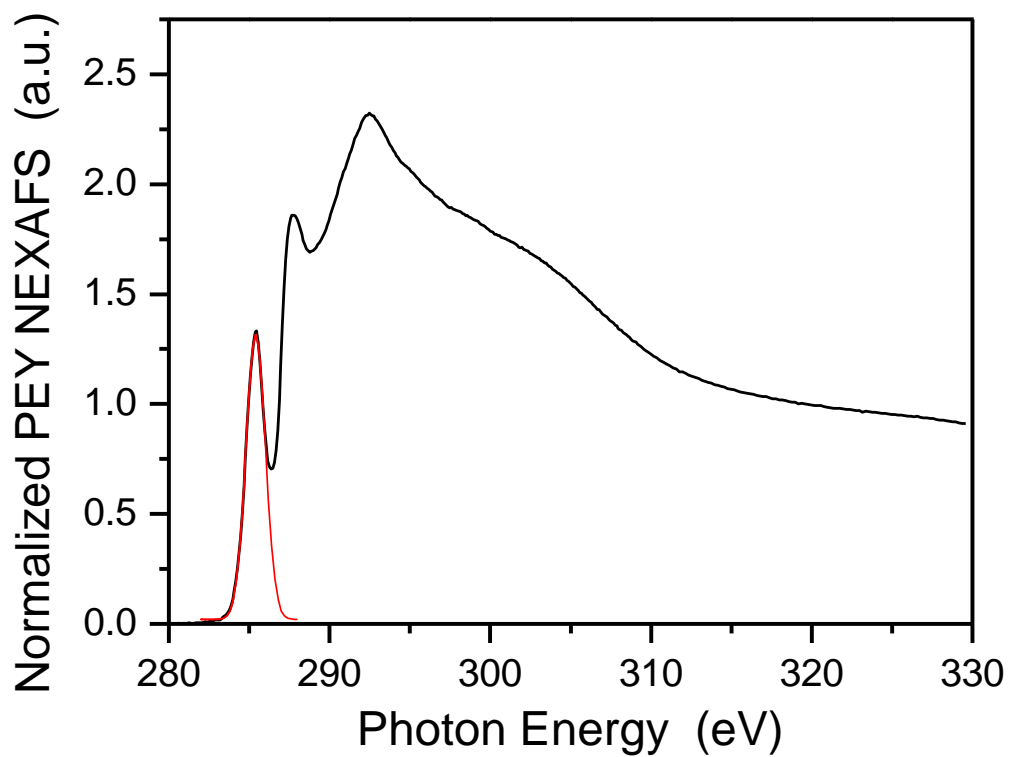


**Figure A.2.** PEY NEXAFS spectra collected from Hondo asphaltenes spin-coated onto a silicon wafer.

## APPENDIX B

### DETERMINING THE ESCAPE DEPTH FOR PEY NEXAFS

The application of SAMs with systematically varying lengths of the alkyl mesogens in the trichlorosilanes enabled us to establish that a correlation exists between the NEXAFS edge jump and the ellipsometric thickness of the SAMs (or equivalently  $N_c$ ). While discussing the dependence of the NEXAFS edge jump on  $N_c$  we briefly pointed out the advantages and disadvantages of both NEXAFS detection methods, the partial electron yield (PEY) and fluorescence yield (FY) modes. A better understanding of the capabilities and shortcomings of each detection mode is acquired when we compare the NEXAFS edge jump to the thickness of the alkyl mesogen of the SAMs (*cf.* **Figure B.1**). The adjusted thickness is obtained by subtracting the thickness of the organosilane head group from the total SAM thickness. This is necessary because the NEXAFS edge jump at the carbon K-edge only probes the carbonaceous material on the surface, whereas ellipsometry measures the total thickness of the SAM, including both the silane head-group and the carbon containing alkyl chain. To accomplish this adjustment we assume that the chains are in an all-trans conformation and

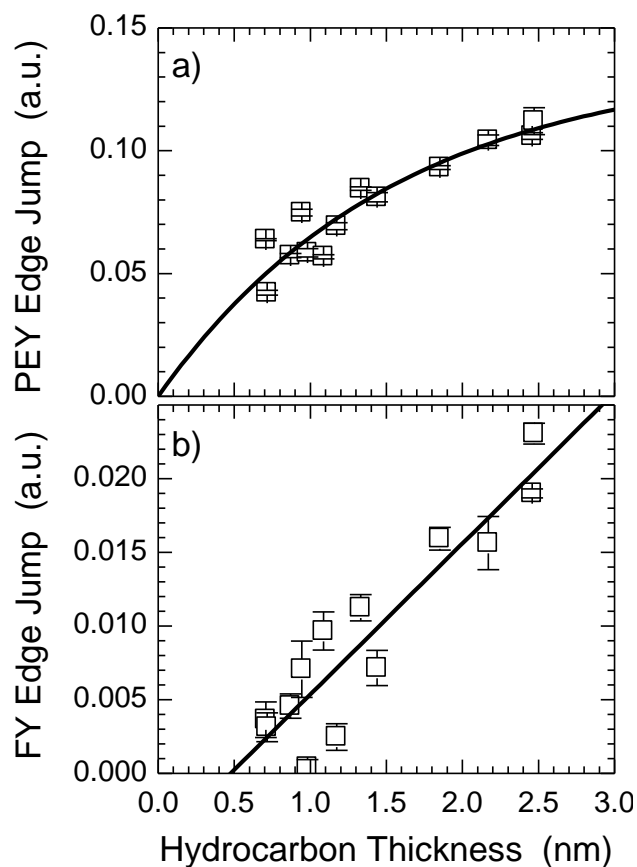


**Figure B.1.** The edge jump of the trichlorosilane SAMs as a function of the adjusted SAM thickness for (a) PEY NEXAFS and (b) FY NEXAFS. The solid line in Figure A.1a represents a best fit to equation A.1, the solid line in Figure A.1b is meant to guide the eye.

subtract a value of  $2.85 \text{ \AA}$  from the total SAM thickness, a number obtained by adding the z-axis projections of a carbon/silicon bond and a silicon/oxygen bond.<sup>1,2</sup> Note that in addition to the carbon present in the SAMs, there is very likely some adventitious carbon contamination present on the sample. Assuming that, to the first approximation, the atomic density of adventitious hydrocarbon is similar to that present in the SAM, the correlation between the NEXAFS edge

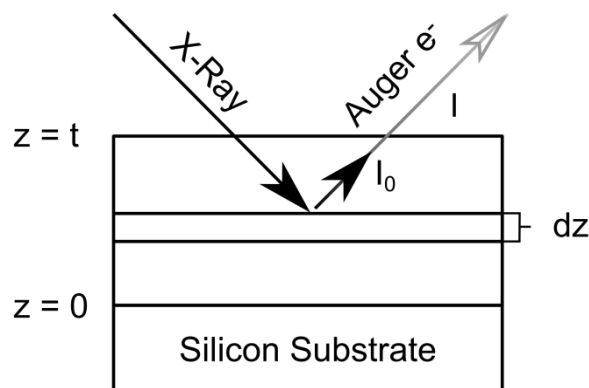


**Figure B.2.** Schematic showing a simple model, from which equation B.1 can be derived.

jump and the hydrocarbon thickness (HT) measured by ellipsometry is not affected by the adventitious carbon because the chemical compositions of the impurities are similar to the SAM and will have comparable dielectric constant (affecting the ellipsometry measurements) and escape depth (affecting the NEXAFS measurements).

**Figure B.1a** displays the PEY edge jump as a function of HT. While the data in **Figure 3.2** showed a nearly linear dependence of the PEY edge jump on  $N_c$ , the same cannot be said about the edge jump dependence on HT. A simple model of the observed Auger electron signal as a function of the thickness of the probed hydrocarbon layer can be constructed, as shown in **Figure B.2**. We assume that the intensity of the Auger electrons originating from an infinitesimally thin slab of the probed material a distance  $z$  from the substrate is  $I_0$ . These electrons

travel through a distance (HT-z) of carbonaceous material before escaping to the vacuum in the NEXAFS chamber and reaching the PEY detector. Given this model, we can write:

$$I = \int_0^{HT} I_0 e^{-(HT-z)/\lambda} dz = I_0 \lambda (1 - e^{-HT/\lambda}), \quad (\text{B.1})$$

where  $\lambda$  is the inelastic mean free path of the Auger electrons, whose intensity in the detector is  $I$ . A best fit to the data using Equation B.1 yields values of  $\lambda = (1.55 \pm 0.32)$  nm and  $I_0 = (0.088 \pm 0.008)$  a.u./nm. We note that the value of  $\lambda$  is close to that recently reported by Sohn et al. ( $\lambda = 1.95$  nm).<sup>3</sup>

In **Figure B.1b**, we plot the FY NEXAFS edge jump as a function of HT. As mentioned in **Chapter 3**, a plot of FY edge jump versus  $N_c$ , extrapolated to  $HT = 0$  yields a negative value of the FY edge jump. A plausible explanation for this is that a minimum amount of carbon has to be probed on the surface in order to be detectable via FY NEXAFS. An equation like B.1 can be written for fluorescent radiation, but the parameter  $\lambda$  is replaced by  $\lambda'$  and increases to hundreds of nanometers. The FY data obtained from SAMs are in the limit of small  $t/\lambda'$  and thus precludes us from fitting and determining  $\lambda'$ . A best linear fit to the FY data suggests that the minimum thickness of carbonaceous material that we are able to detect is  $HT = (0.476 \pm 0.205)$  nm. Additionally, for small  $t/\lambda'$

the slope of the best-fit line becomes  $I_0 = (0.0102 \pm 0.0013)$  a.u./nm. This is a measure of the intensity of fluorescent radiation emitted per nm of material.

This discussion highlights the importance of carrying out NEXAFS measurements in both the PEY and FY detection methods. PEY NEXAFS should be used for probing very thin (1-2 nm thickness) films; the actual thickness depends on the specific material studied. From the data in **Figure B.1** it is apparent that while the PEY signal for films thinner than  $\lambda$  exhibits a reasonably linear dependence on film thickness, upon reaching film thicknesses around 3-4 multiples of  $\lambda$  the signal levels off dramatically because not all Auger electrons can successfully escape from the sample and be detected. In contrast, FY should be used for thicker films, for the case of hydrocarbons studied here; the minimal thickness is  $\approx 0.5$  nm. We expect that this minimal thickness is determined by the sensitivity of the given fluorescence detector and will likely remain the same for most soft materials. Overall, in order to characterize soft material films that span a large range of thickness, a dual detection approach involving both PEY and FY measurements should be invoked when possible.

## **B.1. References**

1. Tompkins, H. G.; McGahan, W. A. In *12.4 Effective Medium Approximations (EMAs); Spectroscopic Ellipsometry and Reflectometry*; John Wiley & Sons, Inc.: New York, 1999; pp 125-126.

2. Alternatively, the thickness adjustment can be accomplished by subtracting 2.34 Å, a mean diameter of the silicon atom, from the total SAM thickness. Using this assumption the value of  $\lambda$  is (1.72±0.37) nm and that of  $I_0$  is (0.008±0.001) a.u./nm.
3. Sohn, K. E.; Dimitriou, M. D.; Genzer, J.; Fischer, D. A.; Hawker, C. J.; Kramer, E. J. Determination of the Electron Escape Depth for NEXAFS Spectroscopy. *Langmuir* **2009**, *25*, 6341--6348.

## APPENDIX C

### MAPPING THE COIL-TO-GLOBULE TRANSITION AND THE EFFECTS OF $P_R$

#### C.1. Mapping the coil-to-globule transition

We perform equilibrations of monodisperse bulk and grafted polymers and compute their properties in order to compare with the reaction-synthesized polymers. A number of chains are placed on the lattice and allowed to equilibrate for  $10^3$  time steps (defined as MCS per bead) at a high temperature. The temperature then decreases slowly at a rate of  $4.0 \times 10^{-7} \epsilon/k_B T$  per time step. The chains are concurrently re-equilibrated every 62500 time steps for  $50 \times 10^6$  MCSs. During the re-equilibration, we compute the values of parameters such as the radius of gyration, its x, y and z components and the volume fraction profiles every  $10^6$  MCSs in order to determine their ensemble averages. **Figure C.1** shows the radius of gyration for both bulk (a) and tethered (b) polymers of various degrees of polymerization (DP) ranging from 10 to 50 as a function of the reduced inverse temperature ( $\beta = \epsilon/k_B T$ ). As  $\beta$  increases the radius of gyration of the chains decreases, passes through a transition point,

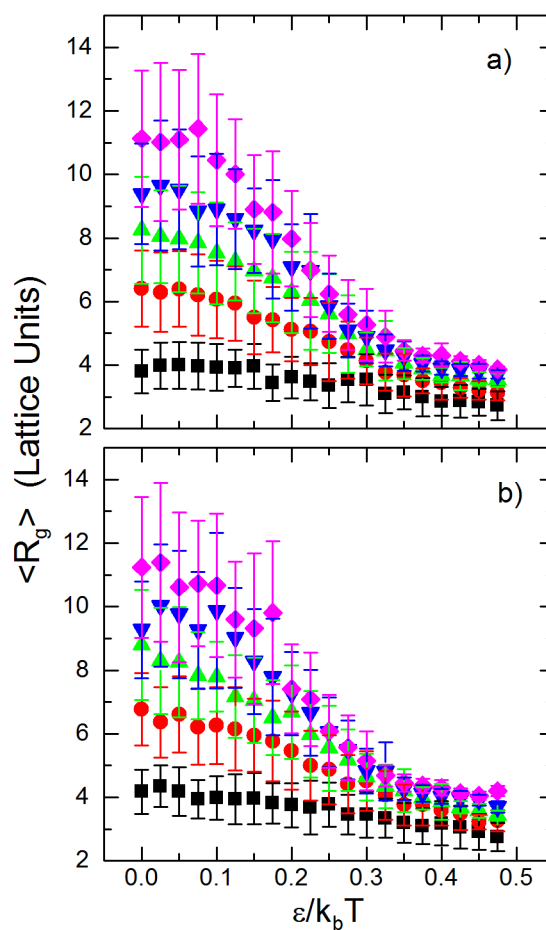


**Figure C.1.** Radius of gyration of a single coil in the bulk (a) and grafted to the surface (b) with degree of polymerization: 10 (■), 20 (●), 30 (▲), 40 (▼), and 50 (◆) as a function of polymer solubility expressed in terms of the reduced inverse temperature.

located at  $\beta \approx 0.225$ , and continues to decrease under poor solvent conditions.

These equilibrations show that one can effectively collapse the chains by tuning

$\beta$  and thus have the capability to simulate polymerizations in various solvent qualities.

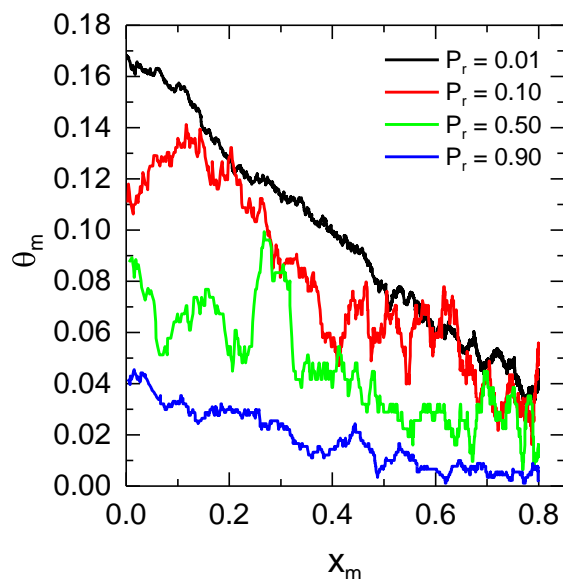


**Figure C.2.** Average number of sites nearest neighbors to the chain-ends occupied by monomer as a function of monomer conversion for bulk-initiated systems in good solvent consisting of  $I_0 = 100$  and  $M_0 = 3125$  at various values of  $P_r$ .

## C.2. Probability of reaction versus motion

As described in the paper we perform a study of the effects of the probability of reaction versus motion ( $P_r$ ) on the results of the simulations. We performed this study at an early stage in our research and the methodology to discern the trends was different from that used in the paper. Instead of fitting a third degree polynomial to the data, we use adjacent averaging to obtain the lines in **Figure C.2**. The system shown here corresponds to bulk polymerization under good solvent conditions with  $I_0 = 100$  and  $M_0 = 3125$ . One important effect of reducing  $P_r$  is that the presence of monomer in the environment of the active

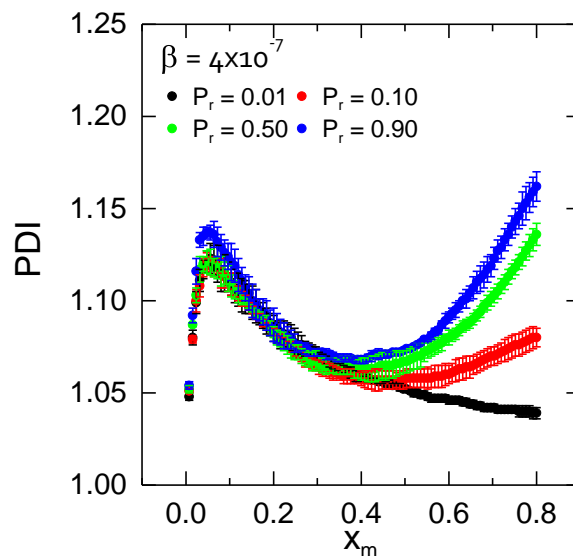


**Figure C.3.** Polydispersity index as a function of monomer conversion for bulk-initiated systems in good solvents consisting of  $I_0 = 100$  and  $M_0 = 3125$  at various values of  $P_r$ .

chain-ends increases substantially because of the reduction in the reaction rate. A direct consequence of this reduction in the polymerization rate is better control of the reaction (**Figure C.3**) which is consistent with reference 32 in **Chapter 4**. The PDI for  $P_r = 0.01$  remains low throughout the polymerization reaction while that at  $P_r = 0.90$  exhibits an upturn at  $x_m = 0.5$ . These data suggests that it is desirable to decrease  $P_r$  to a very low value to achieve true kinetic limitation of the reaction. Unfortunately, as  $P_r$  decreases the simulation time increases and at some point the simulation becomes unfeasible because it only reaches very low  $x_m$ .

## APPENDIX D

### SIMULATION MODEL

We now move to the second topic of this dissertation, namely the computer simulation of surface-initiated controlled radical polymerization reactions. The simulation algorithm used in **Chapters 4** and **5** has been previously described.<sup>1</sup> Here we recount the main features of the algorithm and tabulate the values of the input parameters used in this dissertation.

A flowchart of the simulation process is shown in **Figure D.1**. Polymers in the simulation can be either living or dead. Dead polymers are the ones that underwent a termination reaction and can therefore only move. Living polymers can move and undergo activation, deactivation, propagation, and termination reactions. Of the living polymers, only those that are active can undergo propagation and termination. At the beginning of the simulation, a number of polymers (initiators) are picked at random to represent the active polymers. The number of active polymers depends on the fraction of living polymers (FLP) and the total number of polymers ( $I_0$ ). The active polymers will remain so for a specified number of MC steps (the active chain lifetime, LT). The procedure to

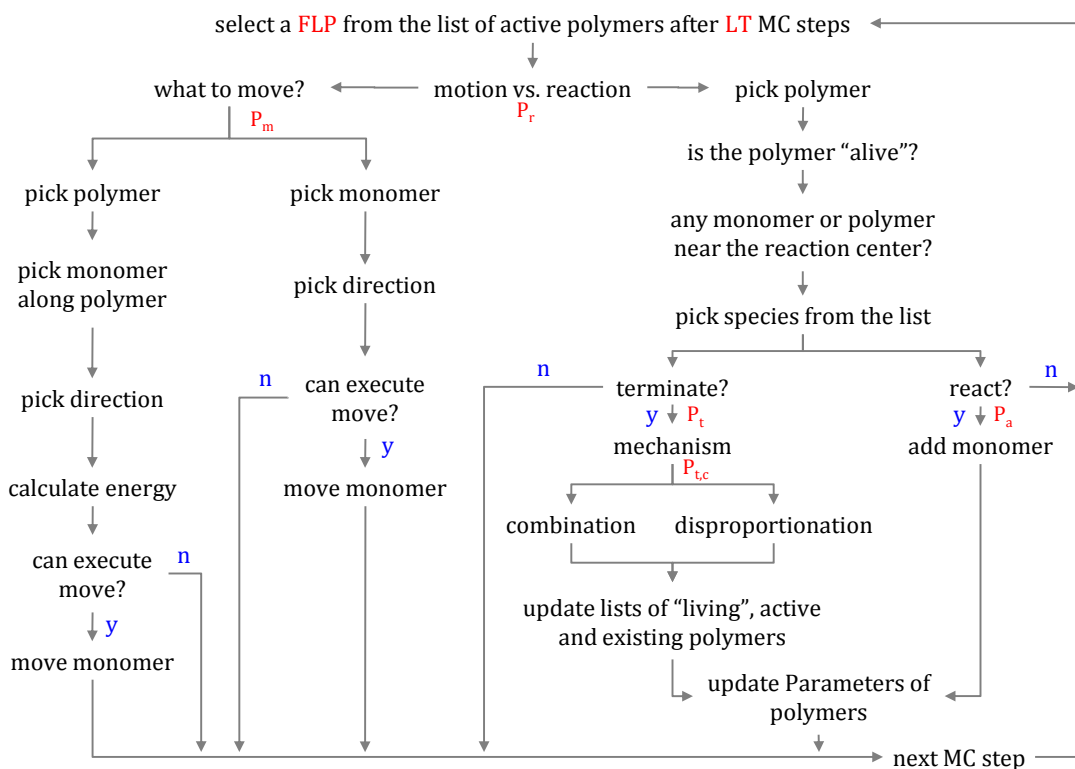


**Figure D.1.** Flow chart of the simulation algorithm.

choose the active polymers occurs at the beginning of the simulation and is repeated every LT steps. The activation and deactivation reactions implemented in this simulation are simple on/off processes. We do not include the molecular level details such as halogen/transfer or persistent radical generation in real controlled radical polymerization processes.

Each MC cycle begins by choosing either motion or reaction depending on the comparison of a random number to the probability of reaction ( $P_r$ ). When motion is selected, either a polymer or a monomer can be moved. The

probability of moving a monomer ( $P_m$ ) depends on the instantaneous number of free monomers available:

$$P_m = \frac{M}{M_o + 2I_o}, \quad (\text{D.1})$$

where  $M_o$  is the initial number of free monomers and  $I_o$  is the initial number of initiators. The factor of two in the denominator arises because the initiators correspond to two joined simulation beads. The probability of moving a polymer is then  $P_p = 1 - P_m$ . Once a choice of moving species has been made, a monomer or polymer from the list of existing species is chosen at random and if a polymer is chosen, a random bead along the polymer chain is chosen for the move. A direction of the move is picked at random and the a one lattice unit move is attempted in the chosen direction. In the case of free monomers, the move is accepted if there are no other beads occupying its new position. In the case of polymer beads the move only if it meets two additional criteria. First, we verify that the move does not violate the previously mentioned set of bond lengths allowed by the BFM. Second, in the case where a potential is used to simulate various solvent conditions (c.f. **Chapter 4**), the energy difference between the configurations before and after the move are compared. If the change in energy ( $\Delta E$ ) is favorable ( $\Delta E < 0$ ), the move is accepted, otherwise the move is accepted according to the Boltzmann probability  $e^{-\Delta E/k_B T}$ .

**Table D.1.** List of input parameters needed for the simulation algorithm and their default values.

Parameter	Symbol	Default value
Initial number of free monomers	$M_o$	12500
Initial number of initiators	$I_o$	400
Percentage of initiators on the surface	$\eta$	100%
Fraction of living polymers	FLP	0.08
Lifetime of living polymers	LT	1000 MC steps
Probability of reaction (vs. motion)	$P_r$	0.01
Probability of addition	$P_a$	1
Probability of termination	$P_t$	0
Probability of combination (vs. disproportionation)	$P_{t,c}$	0.5
Horizontal lattice dimensions	$L_x$ and $L_y$	100
Vertical lattice dimension	$L_z$	100
Reduced temperature ( <b>Chapter 4</b> )	$\beta$	$4 \times 10^{-7}$

If reaction is chosen, a polymer is selected at random from the list of existing polymers. If the polymer is living and active, a list of potential reactive partners nearest neighbors to the chain end is compiled. A species from this list is selected and the reaction occurs with a predetermined probability. If the species selected is a free monomer, a propagation reaction occurs with probability  $P_a$ , whereas if the selected species is another living and active chain, termination occurs with probability  $P_t$ . Termination may occur by combination with probability  $P_{t,c}$ , otherwise occurring by disproportionation.

The input parameters and their corresponding default values are summarized in **Table D.1**. Unless otherwise specified, the parameters listed here

are set to their default values. Some of the parameters are relevant to only one of the forthcoming Chapters (i.e.  $\beta$  and  $\eta$ ).

## **D.1. References**

1. Genzer, J. In Silico Polymerization: Computer Simulation of Controlled Radical Polymerization in Bulk and on Flat Surfaces. *Macromolecules* **2006**, 39, 7157-7169.

## APPENDIX E

### FINDING THE INSTANTANEOUS SHAPE OF A POLYMER COIL

The shape of an unperturbed polymer coil (number of monomers  $N$ )<sup>1,2</sup> is measured by finding the radius-of-gyration tensor of a body consisting of  $N$  atoms<sup>2</sup>:

$$S = \frac{1}{N} \begin{vmatrix} S_{xx} & S_{xy} & S_{xz} \\ S_{yx} & S_{yy} & S_{yz} \\ S_{zx} & S_{zy} & S_{zz} \end{vmatrix}, \quad (\text{E.1})$$

The diagonal elements of the matrix in Equation E.1 are defined by:

$$S_{xx} = \sum_{k=1}^N x_k^2, \quad (\text{E.2.a})$$

$$S_{yy} = \sum_{k=1}^N y_k^2, \quad (\text{E.2.b})$$

$$S_{zz} = \sum_{k=1}^N z_k^2, \quad (\text{E.2.c})$$

And the off-diagonal elements of the matrix in Equation E.1 are defined by:

$$S_{xy} = S_{yx} = \sum_{k=1}^N x_k y_k, \quad (\text{E.3.a})$$

$$S_{xz} = S_{zx} = \sum_{k=1}^N x_k z_k , \quad (\text{E.3.b})$$

$$S_{yz} = S_{zy} = \sum_{k=1}^N y_k z_k , \quad (\text{E.3.c})$$

The origin of the coordinate system is chosen so that it coincides with the center of mass of the particle system. Because of the symmetry of the gyration tensor, one can use Equations. E.2 and E.3 to rewrite Equation E.1 as:

$$S = \frac{1}{N} \sum_{k=1}^N \begin{vmatrix} x_k^2 & x_k y_k & x_k z_k \\ x_k y_k & y_k^2 & y_k z_k \\ x_k z_k & y_k z_k & z_k^2 \end{vmatrix} , \quad (\text{E.4})$$

Diagonalizing Equation E.4 yields:

$$S_{\text{DIAG}} = \frac{1}{N} \sum_{k=1}^N \begin{vmatrix} S_1 & 0 & 0 \\ 0 & S_2 & 0 \\ 0 & 0 & S_3 \end{vmatrix} , \quad (\text{E.5})$$

Where  $S_1$ ,  $S_2$ , and  $S_3$  are the *principal moments* in the principal axes coordinate system ordered such that  $S_3 \geq S_2 \geq S_1$ .

Finding the *principal moments* is equivalent to determining the eigenvalues of the matrix given by Equation (E.1). With the values of  $S_1$ ,  $S_2$ , and  $S_3$  in hand, one can determine the aspect ratios  $S_1/S_3$  and  $S_2/S_3$ . In addition, we define the squared radius of gyration ( $s$ ), asphericity ( $b$ ) and acylindricity ( $c$ ) by Equations. (E.6.a) to (E.6.c):

$$s^2 = S_1^2 + S_2^2 + S_3^2 .. \quad (\text{E.6.a})$$

$$b = S_3^2 - \frac{1}{2}(S_2^2 + S_1^2) , \quad (\text{E.6.b})$$

$$c = S_2^2 - S_1^2 , \quad (\text{E.6.c})$$

which can, in turn, be used to calculate the *relative shape anisotropy* (accentricity),  $\kappa^2$ :<sup>1-3</sup>

$$\kappa^2 = \frac{b^2 + (3/4)c^2}{s^4} , \quad (\text{E.7})$$

For a linear array of atoms  $\kappa^2=1$ , while a molecule with tetrahedral or higher symmetry has  $\kappa^2=0$ .

Our system comprises a number of macromolecules (Q) each having a specific number of monomers. In order to get an average value of  $S_1/S_3$ ,  $S_2/S_3$ , and  $\kappa^2$ , we obtain them by averaging over all chains present in the system:

$$\langle S_1/S_3 \rangle = \frac{1}{Q} \sum_{k=1}^Q (S_1/S_3)_k , \quad (\text{E.8})$$

$$\langle S_2/S_3 \rangle = \frac{1}{Q} \sum_{k=1}^Q (S_2/S_3)_k , \quad (\text{E.9})$$

$$\langle \kappa^2 \rangle = \frac{1}{Q} \sum_{k=1}^Q (\kappa_k^2) \quad (\text{E.10})$$

## E.1. References

1. Theodorou, D. N.; Suter, U. W. Shape of Unperturbed Linear Polymers: Polypropylene. *Macromolecules* **1985**, *18*, 1206-1214.

2. Mattice, W. L.; Suter, U. In *Conformational theory of large molecules : the rotational isomeric state model in macromolecular systems*; John Wiley & Sons: New York, 1994; , pp 449.
3. Lee, H.; Baker, J. R.; Larson, R. G. Molecular Dynamics Studies of the Size, Shape, and Internal Structure of 0% and 90% Acetylated Fifth-Generation Polyamidoamine Dendrimers in Water and Methanol *J. Phys. Chem. B* **2006**, *110*, 4014-4019.